Startability Analysis of Supersonic Air Intakes with Overboard Spillage

Niloofar Moradian

Doctor of Philosophy

Department of Mechanical Engineering

McGill University

Montreal,Quebec

2014-08-15

A Thesis Submitted to McGill University
in Partial Fulfilment of the Requirements of the Degree of
Doctor of Philosophy

DEDICATION

I would like to dedicate my thesis to my beloved parents, and dear sister for all their faith, support and love.

ACKNOWLEDGEMENTS

I would like to thank my supervisor, Professor Evgeny Timofeev, for his constant encouragement, support, patience, and guidance during my PhD. He is a true mentor and has always been generous with his time for me. Without his support, the completion of this work would not be possible.

I would like to particularly thank Dr. Rabi Tahir for his assistance and advice. I would like also to thank Prof. Sannu Molder for his kind interest and attention to this work as well as his useful suggestions. My special thanks to the faculty and staff of the McGill Department of Mechanical Engineering who have been always helpful and co-operative. Dr. Rogerio Pimentel very kindly helped me to improve the French version of the abstract. Any errors that remain are my sole responsibility.

I am extremely grateful to my parents for their understanding and endless love. I would be lost without their unconditional support during my graduate studies.

I would like to thank the Faculty of Engineering of McGill University, the National Sciences and Engineering Research Council of Canada (NSERC), and the McGill Engineering Doctoral Award (MEDA) for their collaborative financial support for this project.

ABSTRACT

For efficient operation of an air-breathing hypersonic/supersonic engine its air intake must be started, i.e., supersonic flow must be established throughout the intake. Among various starting techniques, starting with the assistance of overboard spillage has a number of compelling advantages. The present thesis is devoted to the theoretical and numerical analysis of starting characteristics carried out for the Prandtl-Meyer and Busemann intake families with overboard spillage.

While the provision for overboard spillage is an intrinsic part of the design of planar Prandtl-Meyer intakes, a new way to introduce overboard spillage for the axisymmetric Busemann intakes is suggested in the present work, resulting in a family of three-dimensional Busemann intakes. The theoretical startability analysis is based on the application of the classical quasi-steady Kantrowitz theory to the internal compression section of the on-design intakes under consideration. For three-dimensional Busemann intakes with overboard spillage, an original approach to determine the effective internal compression section area ratio by accounting for the magnitude of spillage area is proposed.

For both intakes families, the limiting self-starting area ratios allowing to maximize the overboard spillage effect are obtained. Furthermore, the Kantrowitz (self-starting) lines on the area ratio/free-stream Mach number diagrams are derived for a number of particular designs within each intake family. It is shown that the so-called "strong shock" design leads to the minimum self-starting area ratios (or maximum self-starting contractions), which are close to the theoretically possible minimum.

Thus, it is demonstrated that the strong-shock-based design principle appears to be rather universal and can be applied to achieve the best possible starting characteristics for different intake families.

The methodology of intake starting numerical trials is developed to replicate the underlying assumptions of the theoretical treatments. In particular, the numerical modelling is based on the 2D and 3D Euler adaptive unstructured finite-volume flow solvers. A very good agreement of the numerical starting outcomes with the theoretical predictions is obtained for planar Prandtl-Meyer intakes. For three-dimensional Busemann intakes with overboard spillage, the proposed theory describes very well the qualitative behaviour of the Kantrowitz (self-starting) line with the change of the intake's geometry. The quantitative agreement is found to be less spectacular than in the case of Prandtl-Meyer intakes because the theory is based on purely geometrical considerations of spillage area, without accounting for gasdynamic spillage parameters. The improvement of intake's starting characteristics comes along with a certain degree of non-uniformity of the intake's exit flow, which is analyzed via numerical simulations. A number of findings of the present work are of practical importance for the design of hypersonic air intakes with improved starting characteristics.

ABRÉGÉ

Pour le fonctionnement efficace d'un moteur aérobie hypersonique/supersonique, son entrée d'air doit être démarrée, i.e., l'écoulement supersonique doit être établi tout au long de la prise d'air. Parmi les différentes techniques de démarrage, celle utilisant le *déversement* externe comporte un certain nombre d'avantages incontestables. La présente thèse est consacrée aux analyses théorique et numérique réalisées sur les caractéristiques de démarrage pour les familles d'entrées d'air du typee Prandtl-Meyer et Busemann avec du déversement externe.

Tandis que l'usage du déversement externe est une partie intrinsèque de la conception des entrées d'air bidimensionnelles due type Prandtl-Meyer, une nouvelle façon de présenter le déversement externe pour les entrées d'air axisymétriques du type Busemann est suggérée dans le présent travail. Ceci résulte en une famille d'entrées d'air tridimensionnelles due type Busemann. L'analyse de la capacité de démarrage théorique est basée sur l'application de la théorie classique quasi-stationnaire de Kantrowitz à la région de compression interne des entrées d'air dans sa condition de project. Pour les entrées d'air tridimentionnelles du typee Busemann avec du déversement externe, une nouvelle approche est proposée afin de déterminer le rapport d'aire effectif de la zone de compression interne en tenant compte de l'ampleur de la zone de déversement.

Les rapports d'aire qui limitent l'auto-démarrage et, pourtant permettent la maximisation de l'effet de déversement externe, ont été obtenues pour les deux familles d'entrées d'air. De plus, le tracé des lignes de Kantrowitz (d'auto-démarrage) sur

le diagramme de rapport d'aire versus le nombre de Mach de l'écoulement libre a été produit pour un certain nombre de designs particuliers au sein de chaque famille d'entrée d'air. Il est démontré que la conception du choc fort conduit à des valeurs minimales de rapport d'aire d'auto-démarrage (ou des contractions maximales d'auto-démarrage), qui sont proches de la valeur minimale théoriquement possible. Ainsi, il est démontré que le principe de conception basé sur le choc fort semble être plutôt universel et peut être appliqué pour l'obtention des meilleures caractéristiques possibles de démarrage pour des différentes familles d'entrées d'air.

Une méthodologie pour les simulations numériques du démarrage des entrées d'air a été développée afin-de reproduire les hypothèses sous-jacentes des analyses théoriques. En particulier, la modélisation numérique a été basée sur les solveurs à volumes finis adaptatifs non-structurés d'Euler en 2D et 3D. Une très bonne concordance a été obtenue entre les résultats des simulations numériques et les prédictions théoriques du démarrage pour les entrées d'air bidimensionnelles deu type Prandtl-Meyer. Pour les entrées d'air tridimensionnelles due type Busemann avec le déversement externe, la théorie proposée décrit très bien le comportement qualitatif de la ligne de Kantrowitz (auto-démarrage) avec le changement de la géométrie de l'entrée d'air. La concordance quantitative est jugée moins spectaculaire que dans le cas des entrées d'air du typee Prandtl-Meyer, puisque la théorie est fondée sur des considérations purement géométriques de l'aire de déversement, sans tenir compte des paramètres de déversement provenant de la dynamique des gaz. L'amélioration des caractéristiques de démarrage de l'entrée d'air est accompagnée d'un certain degré de non-uniformité de l'écoulement à sa sortie. Cette non-uniformité est analysée

par des simulations numériques. Plusieurs conclusions du présent travail sont de l'importance pratique lors de la conception des entrées d'air hypersoniques avec des caractéristiques de démarrage accrues.

TABLE OF CONTENTS

LIST OF TABLES

LIST OF FIGURES

CHAPTER 1
Introduction

Hypersonic/supersonic air-breathing engines belong to the high-speed propulsion systems in which, as their name itself suggests, the atmospheric air is used as the fuel's oxidizer, as opposed to rockets which carry the required amount of oxidizer onboard. Aerospace vehicles with such engines can be potentially used for hyper/supersonic cruise in the Earth atmosphere and as recoverable space launchers to low Earth orbits.

In hypersonic/supersonic air-breathing engines, the atmospheric air must be delivered to the engine's combustor at a certain state, and that is accomplished by the air intake. The intake may be viewed as a converging duct decelerating and compressing the incoming supersonic airflow and supplying the compressed air to the engine's combustion chamber.

For efficient engine operation, the air intake must be "started", i.e., all incoming air flow should be captured and the required supersonic flow established throughout the intake. Due to some fundamental reasons related ultimately to the basic conservation laws, the intake starting is not an easy task, and in most practical situations, intakes would not start on their own spontaneously.

The research described in the thesis is, in general terms, devoted to the air intakes of supersonic air-breathing engines and their starting. The present introductory chapter begins with a review of air-breathing engines and, in particular, their

hyper/supersonic varieties (ramjets and scramjets). This is followed by the discussion of different types of scramjet intakes. Then the reader is introduced to the problem of intake starting, its classic theory and various ways which can be used to achieve the started flow in the intake. All these naturally lead to the formulation of research objectives and the outline of the thesis structure.

1.1 Air-breathing engines and their development

In aerospace practice, there are some typical engines used for many years, such as turbojet and turbofan, which can be used in both subsonic and supersonic flow. These engines contain inlet fans, multiple stages of rotating compressor fans, and multiple rotating turbine stages. In turbojet, the oldest general-purpose engine, the air is compressed into a chamber, and heated by the fuel combustion. Then, it expands out through the turbine into the nozzle to accelerate to high speed to provide propulsion, see Fig. 1–1a. Turbojets are very noisy and quite inefficient if flown below about Mach 2 [1]. In a turbofan, the airstream from the ducted fan is divided into two parts, Fig. 1–1b. One part passes through the core to burn fuel and the other one bypasses the engine core and mixes with the faster stream from the core. This arrangement reduces the noise and also, because of a lower net exhaust speed, it is much more efficient than turbojets at subsonic speeds [2–4]. However, these complex systems make the engines heavy. This is one of the problems that motivates the development of hyper/supersonic air-breathing engines in which the incoming air is compressed by its deceleration from high speed of the aircraft to a lower velocity in converging ducts (so called ram effect) instead of using the rotating components subjected to the high-temperature gasses. Also, having complex systems

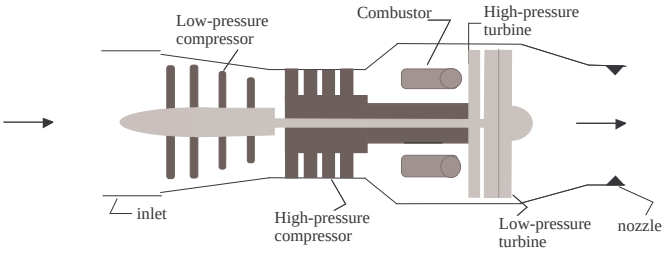

(a) Turbojet

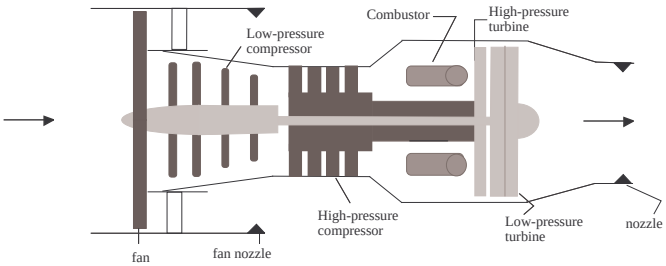

(b)Turbofan

Figure 1–1: Turbojet and turbofan engines' schematics.

in turbojet and turbofan produces the chance of adding more possible failure points to the engine which can be significantly reduced using hyper/supersonic air-breathing engines.

The hyper/supersonic air-breathing engines using the ram effect in converging ducts or intakes generally can be subdivided into ramjets and scramjets. Ramjets utilize an intake to capture the atmospheric air, compress it using converging geometry and shock waves, and decelerate it to subsonic speeds with a terminal normal shock, with subsequent ingestion by a combustor, see Fig. 1–2a. In the combustor, this compressed air is mixed with fuel to burn and, subsequently, the temperature

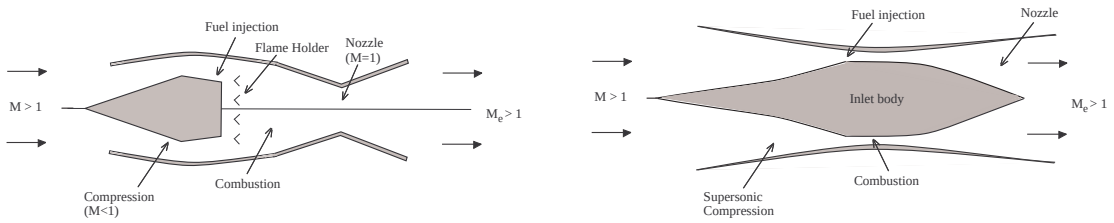

(a) Ramjet [9] (b) Scramjet [10]

Figure 1–2: Schematics of ramjet and scramjet engines.

and pressure inside the engine are raised. In ramjets, the losses as well as the temperature increase because of the strong deceleration of the captured air to subsonic speed, especially, if the Mach number increases to more than 5 [5–8].

Scramjets work similar to ramjets but allow supersonic flow to enter the combustor and involve supersonic combustion of fuel in the air before expansion of the combustion products through a thrust nozzle, see Fig. 1–2b. The flow is slowed to increase the temperature and pressure before combustion. Burning the air-fuel mixture at supersonic speeds and at lower temperatures reduces the losses. Scramjets can be flown up to Mach 15 [11]. In scramjets, high drag is avoided to a significant degree because of the absence of strong shocks. Therefore, scramjets are very promising for efficient super/hypersonic flight. One of the problematic issues of scramjets is the difficulty of mixing and burning the fuel at high airflow velocities in a very short time; therefore, improper geometrical design of the engines may result in a high drag [12].

To give some examples of using air-breathing engines in practice, it is worthwhile to refer to the primary goal of NASA to access space. Over many decades, they tried to improve the hyper/supersonic vehicle design to reach this goal easier. During the

last decade, as the main improvement, they designed air-breathing engines instead of rockets to increase payload capacity or reduce the vehicle size for the same payload. In the 1960s, the comprehensive effort of designing and using air-breathing engines was done at the United Technologies Research Center (UTRC). In the 1970s, in flight tests, ramjet air-breathing engines, such as Advanced Low Volume Ramjet, were examined [13, 14]. The development process was continued, and, finally, it led researchers to test a hydrogen scramjet for the X-30 aircraft in the mid-1980s at Pratt & Whitney under cooperation with the NASP (National Aero Space Plane) project. This engine became the foundation of NASA Hyper-X engines. It is to be mentioned that in a parallel effort, UTRC developed technologies for hydrocarbon-fueled scramjets which were less energetic but more logistically supportable than the hydrogen ones [14]. After less than two decades, in 2001, NASA began testing their first air-breathing engine on the experimental X-43A aircraft which came apart in flight and crashed into the sea a few seconds shortly after its launch [15]. In 2002, the second X-43A vehicle became the fastest free flying air-breathing aircraft in the world at that time. Then, in 2004, during the third aircraft's flight, the scramjet air-breathing engine operated for about 10 seconds, and it reached the speed of Mach 9.68 at about 34,000 meters (112,000 ft) altitude [16, 17]. Most recently, the Boeing X-51A (X-51 WaveRider) aircraft demonstrated the longest scramjet burn duration of 210 seconds at Mach number 5 in May 2013 [18].

1.2 Scramjet intakes

For several decades [12, 19], the scramjet and its intake have already been a major focus in research related to the development of high-speed propulsion systems.

Recently, this research direction has seen a renewed interest and triggered several new projects, such as HyShot [20–22] (the world's first in-flight supersonic combustion) and the subsequent Scramspace [23,24] and HiFIRE [25,26] programs; LAPCAT [27, 28], LEA [29,30] and GRK 1095/2 [31,32] as well as the Hyper-X/X-43 [17,33,34] and X-51 [18,35,36] (the longest scramjet fuel burn) projects.

The efficient operation of all the above-mentioned engines/aircrafts relies heavily on having so-called started air intakes, which means that all incoming flow is captured and inside the intake one has the supersonic flow for which the intake is designed. If these conditions are not met, the intake is considered as unstarted, and in such a case the engine may fail to deliver the required thrust. Therefore, one of the important issues which has to be considered in designing a hyper/supersonic engine is to ensure that the engine's intake can be started. Several intake designs and starting techniques were considered for scramjets. However, there is still no perfect solution available as using some types of intakes make the engines heavy and some others do not provide the required starting characteristics. It is to be mentioned that the reduction of the engine weight is another important issue in designing scramjets. It costs \$3000 to \$5000 per pound to launch payloads into earth orbit and, subsequently, it will cost tens of billions of dollars just to put the Space station into orbit [37]. Therefore, designing a scramjet with the intake which can be reliably and controllably started with less weight is one of the main current goals.

It is therefore clear that the intake is a crucial aspect of an efficient scramjet. The started intake should compress the flow with minimal losses (which means that much of its kinetic energy is to be converted into internal energy) so that to ensure a

high efficiency of the engine's thermodynamic cycle. The intake should maintain high stagnation pressure, and, to the extent possible, uniform velocity and direction of the flow entering the combustor. This study is focused on increasing the startability of scramjet air-breathing engine intakes with an efficient method called the overboard spillage technique which does not add any extra weight to the engines. In the next section, different types of scramjet intakes, and, in particular, those which are used in the present study are considered.

1.3 Different types of scramjet intakes

The intakes used in scramjets may be divided into two categories: two-dimensional (2D) intakes [38–42] and three-dimensional (3D) intakes, which include sidewall compression intakes [43–54] and inward turning intakes, such as the Busemann intakes and the rectangular-to-elliptical shape transition intakes [55, 56].

The interest in engines' intakes was initially focused on 2D intakes, mostly rectangular ones, which generally decelerate the incoming air through a combination of shocks to be adjusted for the combustion system. Some of the most common 2D rectangular intakes are the two-shock and Prandtl-Meyer ramp intakes which designs' details will be explained in the following sections (Section 1.3.1 and Section 1.3.2). These intakes' geometries can be modified to suit various specific design goals.

Two-dimensional intakes have some disadvantages, such as the possibility of unfavorable shock oscillations [57] which may significantly interrupt intake starting and initiate rapid pressure fluctuations as well as their very long ramps to achieve the required compression ratio. Having the compression just in the vertical plane in 2D intakes results in the long length of their ramps. Therefore, designers started

to consider three-dimensional intakes, which also feature the compression in the horizontal plane.

As Heiser and Pratt [19] showed, 3D intakes allow for a more compact, lighter design and better starting characteristics as well as weaker shocks, lower total pressure losses and less significant shock-induced incipient separation. These benefits were demonstrated by Trexler [58], Holland [46, 59], Yuan et al. [60] and Goonko et al. [43, 61] for different types of 3D intakes with sidewall compression.

In recent studies, researchers found that the most efficient intakes are the ones using three-dimensional surfaces obtained through the process of streamline tracing, to compress flow. The streamline tracing technique resulting in a wide variety of surface shapes is used in hyper/supersonic missiles and aircrafts as it can facilitate improved integration of the intake with the aircraft, which is extremely important at hyper/supersonic speeds. In order to design an intake using the streamline tracing technique, firstly, a compressive flowfield is defined; secondly, a curve from which the streamlines originate is established; and then, the streamlines are traced through the flowfield to define the compression surface. The REST-intakes (rectangular-to-elliptical shape transition intakes) [56,62,63] and Busemann intakes [55] are examples of streamline-traced intakes.

Billig and Kothari [64], Tam et al. [65] and Haddad and Moss [66] designed and tested scramjet streamline-traced intakes and showed the intake performance improvement in their tests. Smart's and Trexler's [63] research demonstrated better startability using this type of flow path, and Lu et al. [67] showed that streamline-traced intake's walls can increase the thrust and lift. Bussey and Lewis [68] showed

that even in the case of having viscous and non-uniform flow, 3D intakes based on streamline-tracing have the potential to correct the non-uniformity of the incoming flow and exhibit the performance which is similar to the inviscid case.

Since undesirable viscous phenomena occur in the rectangular-to-elliptical shape transition intake [69], many researchers consider the Busemann intake as the best choice of scramjet engine's intake with high efficiency among various 3D intake designs with streamline-tracing.

A brief overview of the flowfields of the 2D two-shock ramp, 2D Prandtl-Meyer ramp and 3D Busemann intakes, starting characteristics of which will be analyzed in this study, is provided in the following subsections.

1.3.1 Two-shock ramp intake

The two-shock ramp intake represents one of the most simple intake geometries. For many years up to now, in both theoretical and numerical studies as well as in experimental investigations and also in practice, this type of intake was at the center of attention [70–72]. The intake is a rectangular one, including a ramp, a horizontal cowl and side walls, see Fig. 1–3. The ramp deflects the incoming supersonic stream, thus inducing an oblique shock wave. The oblique shock is reflected from the cowl surface. Although, in general, the reflection process can continue inside the intake, it may be designed in such a way that the reflected shock would terminate at the ramp trailing edge (Fig. 1–3b), which is the reason why this type of intake is called a two-shock ramp intake.

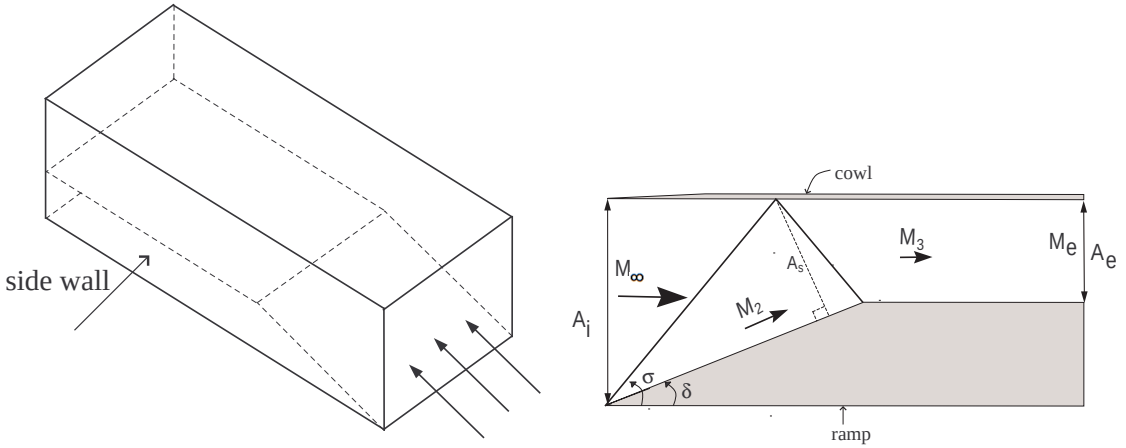

(a) 3D view (b) Cross-sectional side view

Figure 1–3: Schematics of a two-shock ramp intake.

1.3.2 Prandtl-Meyer intake

The Prandtl-Meyer intake is designed on the basis of the Prandtl-Meyer flow [73–75] to improve the efficiency of the ramp intake as compared to the two-shock ramp intake. The only difference between this type of ramp intakes and the two-shock one is related to the ramp geometry, see Fig. 1–4. In the Prandtl-Meyer intake, instead of using a straight wedge for deflecting the incoming air, a concave surface is used to induce an isentropic Prandtl-Meyer compression fan. Thus, the incoming flow passes through the Mach waves of the fan, which are centered at the cowl surface, and then, a reflected shock is produced to restore the original direction of the airstream. Under the appropriate design, the reflected shock may terminate at the ramp trailing edge (Fig. 1–4b) to provide a uniform exit flow. When using the Prandtl-Meyer compression fan to decelerate and compress the flow, the stagnation

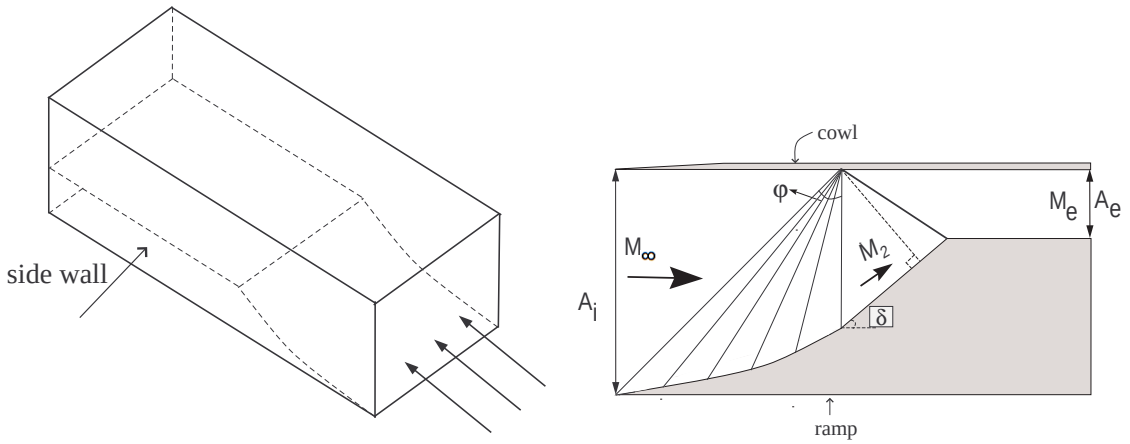

(a) 3D view (b) Cross-sectional side view

Figure 1–4: Schematics of a Prandtl-Meyer intake.

pressure loss is reduced and the efficiency is increased, which makes this intake more practical.

The increase of the intake performance by modifying the two-shock ramp intake to the Prandtl-Meyer intake was shown in [76–78]. Recently, Zhang et al. [78] designed a curved-shock intake with a performance similar to the one of Prandtl-Meyer intakes. They used a curved ramp surface with different angles to produce a curved, variable intensity shock.

1.3.3 Busemann intake

Busemann in 1929 [79] outlined the theoretical aspects of an axial, conically symmetric, supersonic flow (which is known today as Busemann flow) and, subsequently, Taylor and Maccoll [80] published the second order differential equation for this flow. Then, researchers used this flow as the basis for intake design [55,81]. They designed the Busemann intake with its wall contour along a streamline of Busemann

flow. In this intake, isentropic compression in a conical flow deflects the incoming stream towards the axis of symmetry. Then the conical shock returns the flow to its original direction, and the shock is canceled at the end of the intake wall surface to yield an axial, uniform outflow at a lower Mach number [55, 82–85], see Fig. 1–5. In this type of intake, high overall compression and substantial Mach number reduction is attained at high efficiency. To confirm the reduction in total pressure loss and the increase of intake's efficiency in Busemann intakes versus 2D intakes as well as higher pressure recovery in Prandtl-Meyer intakes in comparison with two-shock ramp intakes, for a few cases the pressure recoveries of these intakes are calculated using the analysis explained in the next chapters. For intakes with weak reflected/conical shocks at free-stream Mach number of 3, the total pressure recoveries are 95%, 82% and 67% for Busemann, Prandtl-Meyer and two-shock ramp intakes, respectively, when the compression ratio is about 16. Another analysis for intakes with strong reflected/conical shocks and the compression ratio of 18 at free-stream Mach number of 3 results in the total pressure recoveries of 81%, 69% and 55% for Busemann, Prandtl-Meyer and two-shock ramp intakes, respectively. Clearly, Busemann intakes have the minimum pressure loss among the others.

Molder and Szpiro [55] presented the basics of Busemann intake design and highlighted some idiosyncrasies of Busemann flow as explained above. Molder and Romeskie's [81] experimental results using a full Busemann intake and its modular versions (corresponding to some selected portions of Busemann flow) confirmed the existence of the Busemann flow and better performance of Busemann intakes as compared to 2D intakes and other types of 3D intakes. Molder [86] showed that a

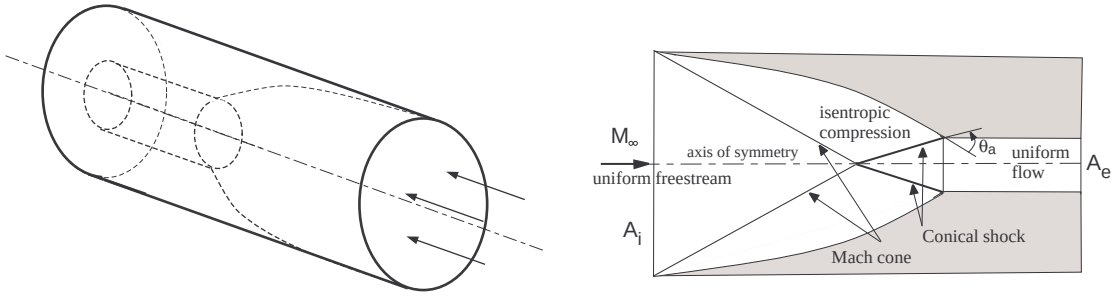

(a) 3D view (b) Cross-sectional side view

Figure 1–5: Schematics of Busemann intake.

Busemann intake can reduce the Mach number from 8.33 to 2.8 with a total pressure recovery of 91%. In 2012, Ogawa's and Boyce's research confirmed the advantage of using Busemann intakes [87] in scramjets. The existence of Busemann flow in a Busemann intake was shown experimentally using flow visualization by Molder [88] who carried out several experiments in the NRC/NAE hypersonic gun-tunnel at a Mach number of 8.33 and in the DRDC trisonic tunnel at a Mach number of 3.

Busemann intakes have some drawbacks as well: 1) long compression surfaces at high Mach numbers lead to high boundary-layer losses [55,89]; 2) high contraction ratios result in starting difficulties under steady free-stream conditions [55]; 3) the intakes are sensitive to off-design conditions at different angles of attack. This study is focused on increasing the intake startability which may help to solve the second difficulty mentioned above.

1.4 Intake starting

The scramjet air intakes are designed to operate in the started mode when they capture all incoming air and a supersonic flow is established throughout the intake at the design free-stream Mach number, see Fig. 1–6a. The process of establishing

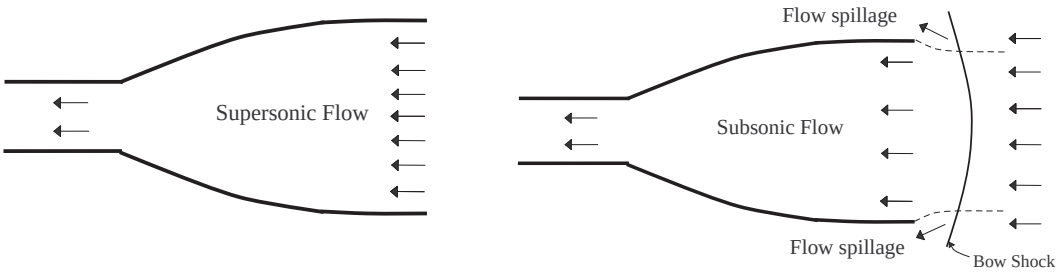

(a) Started intake (b) Unstarted intake

Figure 1–6: Schematics of started and unstarted flowfields.

such started flow is referred to as flow starting or intake starting. Another mode of the flowfield in supersonic air intakes is the unstarted one. In the unstarted mode, as compared with the started mode, less airflow is captured with lower efficiency and pressure recovery [90–94] and higher aerodynamic and thermal loads. In the unstarted condition, the flow inside the intake is subsonic after passing through a bow shock in front of the intake, and some part of the flow is spilled around the intake, see Fig. 1–6b. The unstarted mode may not deliver the required thrust and, thus, it is not suitable for the engine's operation.

Figure 1–7 shows a particular intake used by Saunders et al. [95] at Mach 4. As it is clear from the schlieren photographs, in the started case (Fig. 1–7a) all flow is captured by the intake but in the unstarted one there is some flow spillage, and a bow shock appears in front of the fully enclosed section of the intake. If for some reason, the started flow reverts to the unstarted one, this process is referred to intake unstart. The starting and unstarting processes are important to understand because they may affect the design, operability, and performance of propulsion systems [96–98].

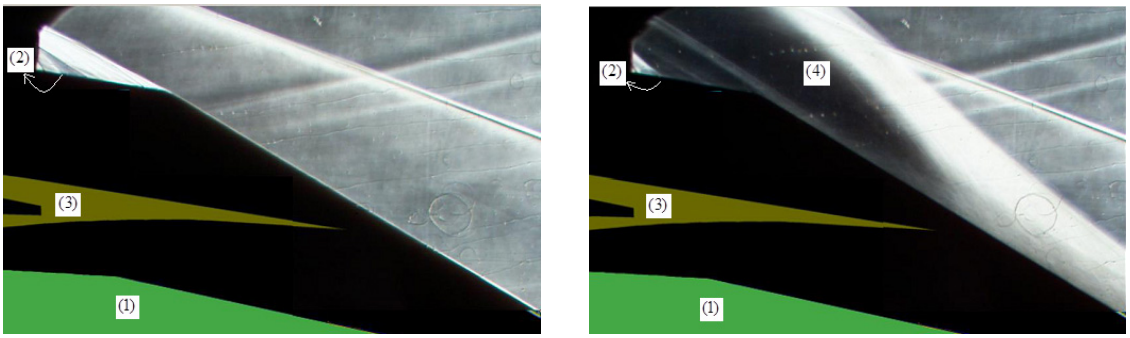

(a) (b)

Figure 1–7: The experimentally visualized flowfields in an intake [95]: a) Started flow; b) Unstarted flow. The flow is from right to left. The numbers on the images represent: (1) ramp; (2) cowl; (3) additional horizontal cowl without any effect on the flow of interest; (4) bow shock.

1.4.1 Started vs. unstarted flow

The earliest recognition of the starting problem can be dated by the 1940s [99–101]. It was found that an intake can be unstarted because the internal contraction is too high, or the back pressure is raised beyond the level that can be sustained by the intake, or a large separated zone is formed (especially at high Mach numbers).

This problem can be controlled and solved by designing the intake with an appropriate contraction ratio (the ratio of the inlet area to the exit area of the intake). There are two critical contraction ratios or critical area ratios (which is the ratio of the exit area to the entry area) for an intake, which need to be considered in order to start the intake and keep it started. The first limit is called the *isentropic* one, and the second limit is known as *Kantrowitz* limit.

The isentropic constraint comes from the well-known fact originating from the basic conservation laws [102] that for an isentropic, quasi-steady, quasi-one-dimensional flow with a given mass flow rate, there is a minimum cross-sectional area through

which the flow can still pass. At the cross-section with this minimum area, the flow becomes sonic, i.e. its Mach number M becomes equal to 1, or, in other words, the flow is choked. The respective minimum cross-sectional area is called the sonic area, A^*.

Therefore, for an intake with the inlet (free-stream) Mach number $M = M_\infty$ and the inlet cross-sectional area A_i, the minimum exit area A_e can be obtained from the area-Mach number relation for an isentropic, quasi-steady, quasi-one-dimensional flow [102]:

$$\left(\frac{A^*}{A_i}\right)_{isentropic} = \left(\frac{A_e}{A_i}\right)_{isentropic} = M\left[\left(\frac{2}{\gamma+1}\right)\left(1+\frac{\gamma-1}{2}M^2\right)\right]^{-\frac{\gamma+1}{2(\gamma-1)}}. \quad (1.1)$$

where A^* is the choked exit area.

In the limiting case of $A_e = A^*$, the flow Mach number decreases along the intake from the free-stream value M_∞ to $M_e = 1$. If the area ratio A_e/A_i is greater than $(A_e/A_i)_{isentropic}$, the exit Mach number is supersonic ($M_e > 1$) and the started supersonic flow can exist in the intake. However, if $(A_e/A_i) < (A_e/A_i)_{isentropic}$, the given mass flow rate is defined by the inlet area A_i and free-stream parameters cannot pass through the exit. The flow reverts to the unstarted mode in which the excessive mass is spilled overboard via the mechanism provided by a curved bow shock arising in the vicinity of the intake's entry. The bow shock stand-off distance is determined by the magnitude of the mass to be spilled.

Therefore, when designing an intake, its area ratio $A_{exit}/A_{inlet} = A_e/A_i$ should be greater than the isentropic area ratio defined above, to have an isentropic operation with supersonic ($M > 1$) or choked ($M = 1$) flow at the throat (exit).

The second limit on the area ratio of the intake, the *Kantrowitz* limit, is determined by assuming a normal shock at the intake entrance so that all incoming mass flow is captured by the intake. Then, the isentropic area ratio for the flow Mach number downstream of the shock represents the second limit of the intake area ratio. The intake area ratio must be equal or greater than the above limiting value for spontaneous intake starting (self-starting). The classical theory (Kantrowitz theory) discussed in the next section gives more details regarding the calculation of the second critical limit of the started intake's area ratio.

1.4.2 The classical theory of quasi-steady intake starting

Kantrowitz and Donaldson [99] and Kantrowitz [100] established the classical theory to predict the flow starting or unstarting in converging ducts. This theory is based on the consideration of the flowfield inside the intake in which a normal shock is located exactly at the entrance to a fully enclosed intake and the incoming flow becomes subsonic downstream of it and passes through the intake and the choked throat (the second, self-starting, limit explained in the previous section). The Mach number of flow downstream of the normal shock is calculated:

$$M_y = \sqrt{\frac{2 + (\gamma - 1)M_x^2}{2\gamma M_x^2 - (\gamma - 1)}}. \tag{1.2}$$

where M_x and M_y are respectively the flow Mach numbers upstream and downstream of the normal shock.

In this theory, it is assumed that the flow downstream of the shock is quasi-one-dimensional, quasi-steady and isentropic. These assumptions and their validity may be the reasons of the differences between the numerical, experimental and theoretical results for startability of an intake as will be discussed in the relevant chapters of the present thesis.

In Fig. 1–8, the essence of this theory is graphically shown in the intake area ratio free-stream Mach number diagram, which is often called the Kantrowitz diagram. It contains three regions delineated by two limiting lines/boundaries. The solid line refers to the isentropic limit. Bellow the isentropic line the intake cannot be started in principle as explained above. The dashed line is the Kantrowitz or self-starting line. This line at different Mach numbers represents the area ratio of the intake with a normal shock exactly at the entrance of the intake and the choked exit. This area ratio can be calculated using Eq. (1.1) where the Mach number is the Mach number of flow downstream of the normal shock M_y which can be calculated using Eq. (1.2). The outcome of this substitution is:

$$\left(\frac{A_e}{A_i}\right)_{Kantrowitz} = \sqrt{\frac{2+(\gamma-1)M^2}{2\gamma M^2-(\gamma-1)}}\left[\frac{(\gamma+1)M^2}{2\gamma M^2-(\gamma-1)}\right]^{-\frac{\gamma+1}{2(\gamma-1)}}. \qquad (1.3)$$

where M is the free-stream Mach number M_∞.

It is shown in [102] that the normal shock is unstable in a converging duct. Thus, if the intake's area ratio is greater than the value represented by the calculated limiting line explained above, the shock enters the intake and it will then continue its downstream motion thill the intake's exit. This is refereed to as shock swallowing and spontaneous intake starting. If the intake's area ratio is lower than the limiting

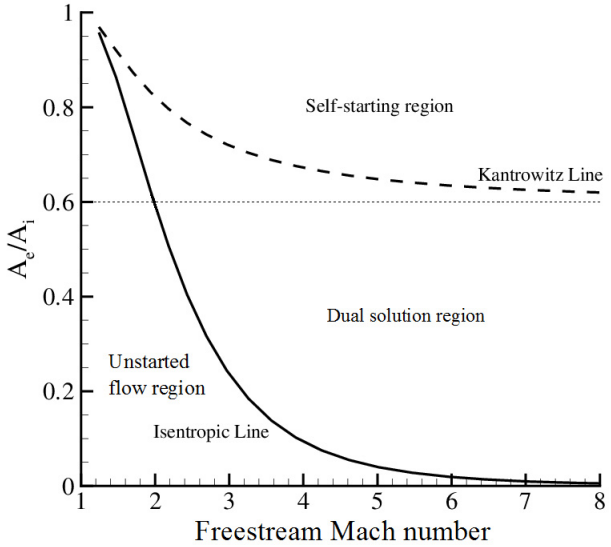

Figure 1–8: The area ratio/free-stream Mach number diagram (the Kantrowitz diagram).

value, the post-shock flow cannot pass through the intake's exit, and the normal shock comes out of the intake and becomes a bow shock providing the necessary amount of spillage.

Between these two boundaries, the isentropic and the Kantrowitz limits, as shown in Fig. 1–8[1] , there is the dual solution region which means that it is possible to have both started and unstarted intake flows for the same free-stream Mach number and the intake's area ratio. However, none of them will change into the other one

[1] The maximum free-stream Mach number of 8 is chosen completely arbitrary in this and subsequent figures. It is possible to choose any desired larger Mach number for such plots.

spontaneously. In the case of initially having an unstarted intake with the area ratio below the isentropic limit at the chosen free-stream Mach number, when the intake area ratio is increased to a value in the dual solution region, the intake remains unstarted and the shock swallowing does not occur. The reason is that the flow sonic area after the shock exceeds the exit area (they become equal only at the Kantrowitz line). On the other hand, in the case of initially having a started intake in the self-starting region, when the intake area ratio is decreased to a value in the dual solution region, the started intake flow does not revert to unstarted one as the exit area is still greater (or equal, on the isentropic line) than the sonic area for the given free-stream Mach number.

A scramjet intake designed to operate at a state in the dual solution region, most likely will not start spontaneously, on its own, because in most practical situations it approaches the desired Mach number from initially low speeds. The intake is initially below the isentropic line and hence, in the unstarted mode. As explained above, the intake would remain unstarted upon crossing the isentrope. This constitutes the well-know intake starting problem. Methods to start intakes in the dual solution region are presented in the next section.

The theory explained above does not take into account viscous effects. Flow viscosity results in boundary layers on the intake's walls with the possibility of their separation. These effects may reduce the effective exit-to-inlet area ratio of the intake thus requiring larger exit areas to start it. Therefore, the "isentropic" and Kantrowitz lines for viscous intake flows would correspond to higher area ratios for a given free-stream Mach number as compared to the inviscid case. In other words,

viscous effects are detrimental to intake's startability. Also, shock wave/boundary layer interactions may result in shock oscillations and produce buzzes, which disturb the flow through the intake and make it very nonuniform.

1.5 Methods of intake starting

The spontaneous intake starting (self-starting) region above the Kantrowitz line is shown on the Kantrowitz diagram (the area ratio/free-stream Mach number diagram) in Fig. 1–8. As explained in the previous sections, in the dual solution region, between the Kantrowitz and isentropic lines, both started and unstarted intake flows are possible and, most importantly, the gradual acceleration from zero velocity always results in unstarted intake flow in this region. Spontaneous starting (shock swallowing) would not occur and, therefore, special techniques should be devised and applied to start intakes in the dual solution region.

In the following subsections, five intake starting techniques are outlined and discussed. The first four techniques are overspeeding, variable geometry, perforated diffuser, and overboard spillage. These basic techniques can be used individually or in various combinations. They all involve quasi-steady starting flows, which are subjected to the constraints of the Kantrowitz theory. Thus, the general idea behind all these methods is to effectively bring the intake to a state at or above the Kantrowitz line where it would start spontaneously and then bring it back to the chosen operational point in the dual solution region. The specific realization of this general approach for each particular technique is discussed in the subsections below. The fifth intake starting approach, which was relatively recently proposed in [103–106],

stands apart. It attempts to use *unsteady* effects, thus circumventing the constraints of the quasi-steady Kantrowitz theory.

1.5.1 Overspeeding

Arguably, the most well-known starting method is the overspeeding technique. The SR-71 "Blackbird" aircraft (1964) is a good example of using this technique as a part of the starting process of the supersonic engine [107]. In this technique, to start an intake, it is accelerated to a Mach number higher than the one given by the Kantrowitz-Donalson limit for the intake's area ratio. As shown in Fig. 1–9a, the intake at the free-stream Mach number M_1 and the area ratio $(A_e/A_i)_1$, is accelerated to reach the state with the free-stream Mach number M_2 and the same area ratio $(A_e/A_i)_1$ above the Kantrowitz limit, and it gets started. Then, it is decelerated to a desired operational Mach number M_3 at the same area ratio $(A_e/A_i)_1$. In fact, its final state is below the Kantrowitz limit and above the isentropic line (in the dual solution region), see Fig. 1–9b.

This starting process can be explained from the gasdynamic point of view as follows. Equation (1.1) gives the sonic area A^* as a function of flow Mach number. When the flow Mach number is $(M_\infty = M_1)$, the intake is unstarted and the sonic area downstream of the bow shock is larger than the throat area A_e. By increasing the free-stream Mach number, the post-shock Mach number M_y and the respective sonic area A_y^* decreases (and hence, the required amount of spillage is decreased, and the bow shock is pushed toward the intake's inlet) until A_y^* is equal to (when the shock is exactly at the entrance of the intake) or less than the throat area. in the state when $(M_\infty = M_2)$, the shock is swallowed and the intake is started. Then,

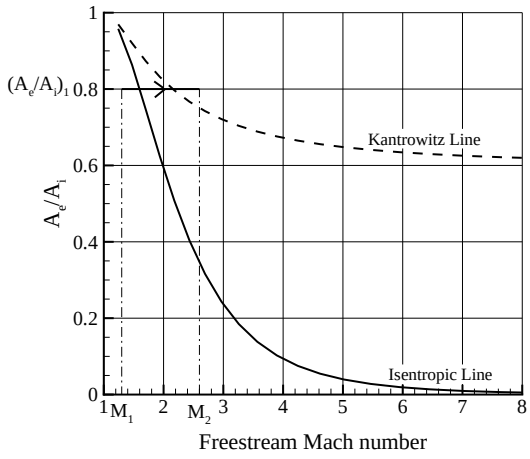

(a) Accelerating the supersonic vehicle

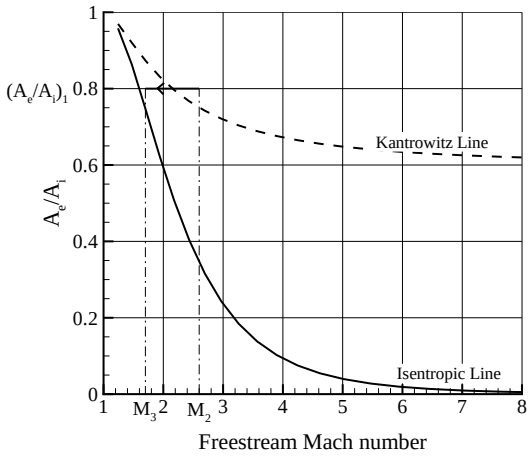

(b) Decelerating the supersonic vehicle

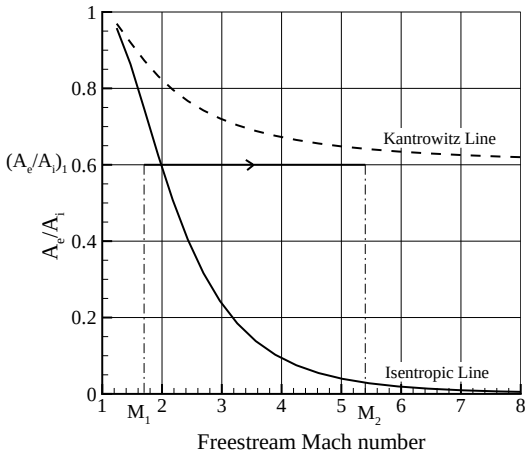

(c) The diagram explaining the constraints of the overspeeding technique.

Figure 1–9: Overspeeding starting technique illustrated on the area ratio/Mach number diagrams.

by lowering the free-stream Mach number to the design one M_3, the appropriate operational state for the intake is achieved, and the intake would remain started as

the throat area is greater than the sonic area for $M = M_3$ (the state is above the isentropic line).

It is to be noted that this technique is not suitable for supersonic intakes with high contractions (low area ratios) [70, 72, 108–110] because very large values of the shock Mach number ($M_\infty = M_x \longrightarrow \infty$) result in finite value of the Mach number downstream of the shock, M_y; i.e. (for $\gamma = 1.4$):

$$\lim_{M_x \to \infty} M_y = \lim_{M_x \to \infty} \sqrt{\frac{2 + (\gamma - 1)M_x^2}{2\gamma M_x^2 - (\gamma - 1)}} \simeq 0.378. \tag{1.4}$$

Subsequently, according to Eq. (1.3), the area ratio $(A_e/A_i)_{Kantrowitz} = (A_y^*/A_i)$ is limited to ~ 0.6, see Fig. 1–9c. Therefore, for an unstarted intake with the area ratio A_e/A_i lower than ~ 0.6, the overspeeding technique will not help to get a started flow.

1.5.2 Variable geometry

Changing the geometry of an intake is another method to start the intake by increasing its area ratio. To increase the area ratio, two general options are available: opening the exit of the intake or closing some part of the intake entry. The former option may be implemented via the installation of movable "doors" or flaps near the intake's exit [111, 112] while for the later one transferrable central bodies and/or cowls may be used [113,114]. For example, a movable cone along the intake's axis can be used to manage the incoming airflow. By moving the cone in and out, the entry area is changed, which results in changing the area ratio of the internal compression section of the intake and in starting of the intake.

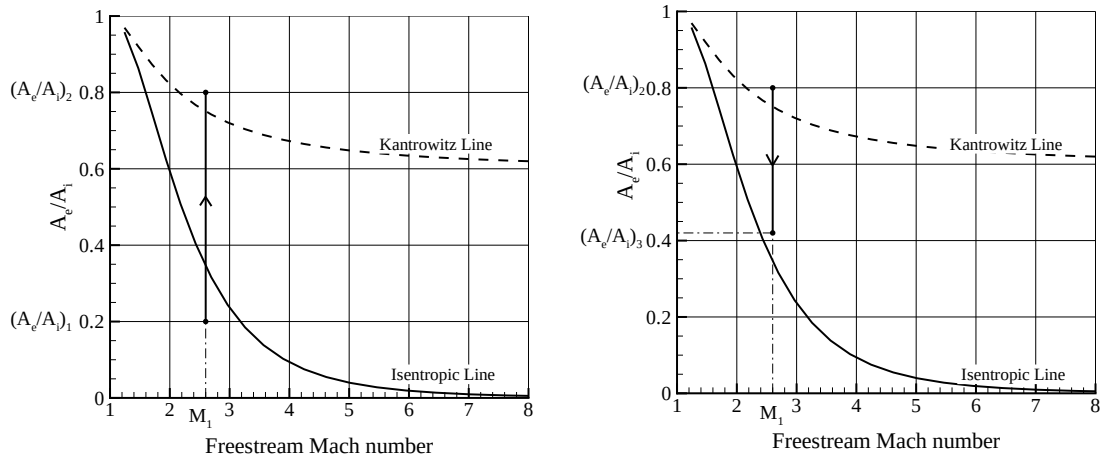

(a) Increasing the area ratio of the intake (b) Decreasing the area ratio of the intake

Figure 1–10: Intake starting process using the variable geometry technique.

To illustrate this technique on the area ratio/Mach number diagram, an unstarted intake with the area ratio $(A_e/A_i)_1$ is considered at the free-stream Mach number M_1 below the isentrope, see Fig. 1–10a. Then, by increasing A_e or decreasing A_i, the area ratio $(A_e/A_i)_2$ above the Kantrowitz limit is reached and the intake starts, see Fig. 1–10a. Then, by decreasing A_e or increasing A_i, the most efficient operation condition at a lower area ratio $(A_e/A_i)_3$ may be achieved, see Fig. 1–10b.

The variable geometry technique is a straight forward one to use but, it requires extra mechanisms to change the intake's area ratio and, therefore, leads to weight increase. This technique was explained and studied by many researchers [14, 70, 72, 109, 115, 116]. Recently, a comprehensive study was carried out by Dalle et al. [117]. They considered a variable geometry 2D intake design to change the intake's startability by moving the cowl forward and backward or up and down or by rotating the cowl leading edge. They found that the intake with a forward/backward moving

cowl had better startability, which leads us to another method of intake starting via overboard spillage. This method will be explained in Section 1.5.4 below.

In practice, two-dimensional intakes with variable geometry were used for example, in the US Air Force F-15 Eagle aircraft [118], the Anglo-French Concorde supersonic airplane [119, 120], the intake of Mach 2.0 B-58 Hustler bomber [121], and the YF-12/SR-71 series of Mach 3.0+ aircrafts [122]. In the 1990's, this starting technique was an essential part of the design of SR-71 Blackbird and Russian MiG-21 jet fighters [123], and it was used in the NASA's High-Speed Research Program [124]. During the last few years, the National Aero-Space Plane (NASP) and X-43C [125] were the flight vehicles using variable-geometry intakes; also, the Ground Demonstrator EngineBuild 2 (GDE-2) demonstrated a good performance at Mach number 4.5 to 6.5 using this method [125]. Furthermore, Morgenstern et al. [126] and Hirt et al. [127] studied and examined supersonic transportation systems in which this technique was used to start the engines.

1.5.3 Perforated diffusers

Using perforated diffusers is another starting technique based on having mass spillage through holes/slots in the walls of the intake. Therefore, the exit flow area and, subsequently, the area ratio of the intake increases so that the intake is effectively brought to the self-starting region above the Kantrowitz line [101, 128], see Fig. 1–10. The process of intake starting is similar to what is shown in Fig. 1–10a for the variable geometry technique. As shown in Fig. 1–10b, after having the started mode, the area ratio is decreased with closing the perforations to achieve an appropriate operational state. Using extra and rather sophisticated mechanisms to open and

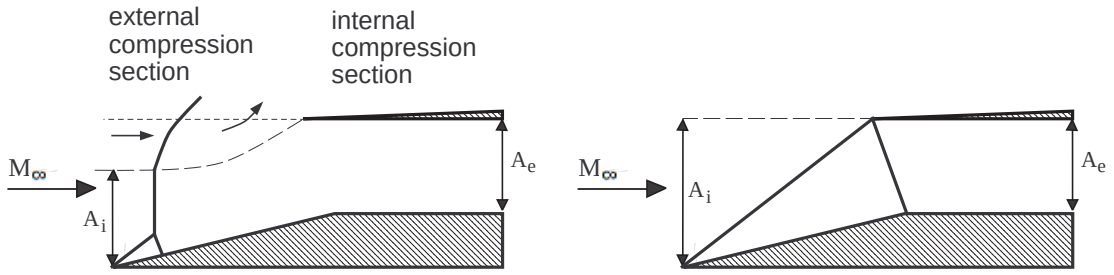

(a) Unstarted flowfield (b) Started flowfield

Figure 1–11: Illustration of flow spillage for intake starting using the overboard spillage technique.

close the perforations under high temperature and pressure conditions increases the intake's weight and its overall complexity and may reduce its operational reliability.

This method is also known as a "bleed system", practical benefits of which were recently considered by Liou and Benson [129]. Nowadays, because of the above mentioned disadvantages, the technique is not used to start intakes and is mostly applied in relation with boundary layer separation to lessen its effect.

1.5.4 Overboard spillage

The overboard spillage technique, as its name suggests, relies for starting an intake on the overboard spillage of the incoming flow during the starting process. The spillage mechanism is introduced via mixed compression intake design, as shown in Fig. 1–11. Mixed compression implies the presence of an internal compression section in which the flow is encased by the intake walls from all sides and a preceding external compression section, in which the wall is notably absent from one side, thus providing for the possibility of flow spillage over the intake cowl.

In an unstarted intake, the flow which cannot be ingested through the intake's exit is spilled from the cowl region (Fig. 1–11a). This spillage mechanism allows the

bow shock to move towards the cowl lip. In fact, the overboard spillage mechanism may be interpreted as using a large perforation of variable size located near the entrance of the intake. The process is continuing until the bow shock arrives to the cowl lip and no spillage occurs any more. Then, if the Kantrowitz limit is satisfied for the internal compression section, the bow shock is swallowed and the intake becomes started, see Fig. 1–11b. In the started mode, the external surface is used to pre-compress and decelerate the free-stream flow before entering the fully enclosed (internal compression) section.

The starting principle of an intake via overboard spillage can be explained by considering states 1 and 2 shown in Fig. 1–12a. State 1 on the Kantrowitz diagram represents the whole intake with the area ratio $(A_e/A_i)_1$ in the free-stream flow with the Mach number $M_1 = M_\infty$ while state 2 represents only the fully enclosed (internal compression) section of this intake with the area ratio A_e/A_s and the upstream Mach number M_s (Fig. 1–12b). As shown in Fig. 1–12b, it is clear that $(A_e/A_i) < (A_e/A_s)$ and $M_s < M_1 = M_\infty$. At state 2, the incoming flow has a lower Mach number and the fully enclosed (internal compression) section has a larger area ratio, which effectively brings the intake above the Kantrowitz limit (Fig. 1–12a) and it starts spontaneously. Thus, without using any additional mechanisms, the intake can start using the overboard spillage technique just by virtue of its design.

In other words, the one-dimensional Kantrowitz theory and the resulting constraints are applicable only for fully enclosed intakes, i.e., in the present context, for the internal compression section. The external compression section then serves as a

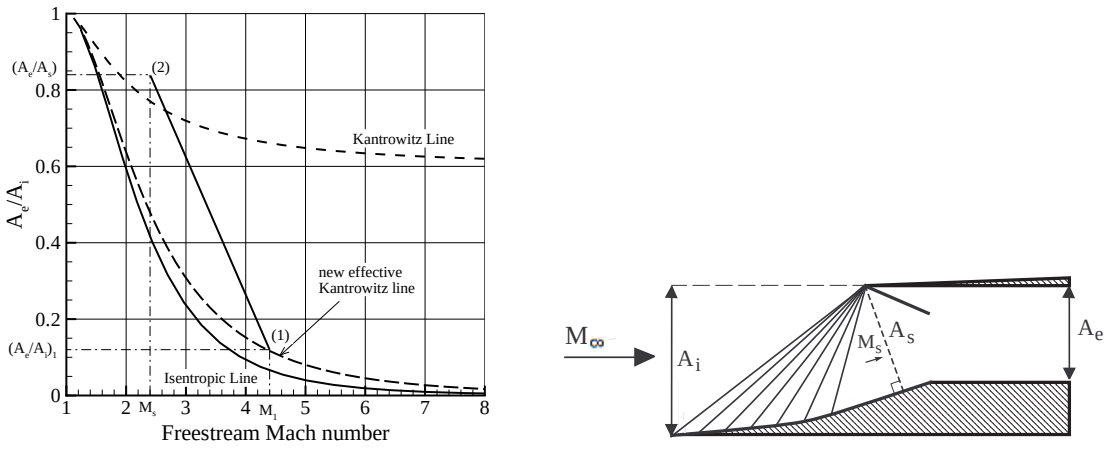

(a) Effective starting process (b) Started intake flowfield

Figure 1–12: The principle of the overboard spillage technique.

"pre-conditioner" modifying the flow Mach number and the area ratio in a manner favorable for easier starting of the internal compression section.

It is important to mention that the started flowfield may be identical to that for the same intake design without the provision for overboard spillage (e.g. see Figs. 1–3 and 1–4). In other words, this starting technique allows to improve starting characteristics without modifying the started flowfield itself. This fact will be further used and illustrated in the next chapters.

The theory of using spillage to lower the Kantrowitz limit was generally studied by such researchers as Molder et al. [130] and Najafiyazdi et al. [131]. Veillard et al. [132] and Sun and Zhang [133] continued these studies for different types of intakes. Hohn and Gulhan [134] experimentally investigated the moveable cowl effect on the starting of a 3D ramp intake at Mach number 7, which confirmed the benefits of using this method to increase the startability of the intake. Most recently,

Zhang et al. [78] showed that the overboard spillage technique has an appreciable effect on startability of a 2D curved-shock intake, even in off-design conditions, while Rosli et al. [135] showed that for low Mach numbers, overboard spillage increases startability up to 40% (in terms of area ratio). Virtually all recent experimental hypersonic vehicles (X-51A, HyShot, HiFIRE etc) relied on overboard spillage for intake starting [18, 20–22, 25, 26].

Veillard et al. in [132] considered the whole family of two-shock ramp intakes with overboard spillage and found which intakes in this family possess the lowest self-starting area ratio or the highest self-starting contraction. They also put forward the strong-shock-based design principle which may be viewed as a simple and straight forward way to obtain such intakes with the best starting characteristics via overboard spillage. This line of study will be continued in the present thesis as explained in Section 1.6.

1.5.5 Starting with unsteady effects

The Kantrowitz theory is based on the quasi-steady flow assumption and, therefore, its conclusions and constraints are not valid in case the starting flow is essentially unsteady. This observation led researchers to investigate the influence of flow unsteadiness and its potential usefulness for intake starting.

Unsteady free-stream flows or unsteady flows inside the intake were considered by Degani and Steger [136] and Park et al. [103], who numerically analyzed the inviscid, unsteady flow past a moving compression ramp. Coon and Chapman [137] conducted an experimental study of the unsteady, three-dimensional flow over an oscillating flap at $M = 2.4$. Molder et al. [138] widely investigated various unsteady

flows in scramjet intakes. In the last decade, VanWie [12], Tahir et al. [104], Li et al. [105] and Grainger et al. [106] carried out some more studies on this subject.

All these researchers found that, indeed, the intake can be started with a lower area ratio when the incoming flow is unsteady or unsteady flow can be induced inside the intake. Mostly, they considered 2D or axisymmetrical intakes with a diaphragm or a "door" at the entrance, opening of which at different speeds may produce unsteady flow and, subsequently, lead to starting of the intakes which would not start spontaneously otherwise.

The present thesis deals with quasi-steady intake starting theories and, hence, any potential influence of unsteady effects in the respective numerical starting experiments is to be avoided. More detailed discussion of this issue is presented in Chapter 3.

1.6 Research objectives and outline of the thesis

The overboard spillage technique described above is, arguably, the simplest way of intake starting. It does not require any additional arrangements, such as movable intake components, opening/closing of doors or perforations etc., which significantly increase the intake's complexity. Provisions for overboard spillage are simply included at the geometrical intake design stage by means of having both an external compression section and an internal compression one. Thus, there is a clear incentive for an in-depth study of overboard spillage for various intake families. Among the questions to be answered are: is it possible to maximize the overboard spillage effect for a given intake family? Are there particular designs providing better starting characteristics via overboard spillage? Does the strong shock design principle

by Veillard et al. [132] hold for other types of intakes? How to introduce overboard spillage into the existing high-efficiency intake designs? One of the first attempts along these lines was undertaken by Veillard et al. [132] for two-shock ramp intakes. The present study may be considered as a direct, systematic continuation of their efforts towards more complex and practical intakes.

More specifically, in this study the startability analysis is carried out analytically and using numerical modelling for two-dimensional ramp intakes and three-dimensional Busemann intakes with overboard spillage. At first, for the sake of completeness and subsequent comparisons the theoretical analysis of two-shock ramp intake starting considered by Veillard et al. [132] is presented in Chapter 2 in detail. Then this analysis is generalized for Prandtl-Meyer ramp intakes of various designs, in which the ramp shock is replaced with a centered Prandtl-Meyer expansion fan. Chapter 3 is concerned with the methodology of intake starting numerical experiments to be presented in the subsequent chapters. In particular, Chapter 4 contains the results of numerical intake starting trials for both ramp intake families (two-shock and Prandtl-Meyer ones) and the comparison of these results with the theoretical self-starting curves from Chapter 2. In Chapter 5, at first the structure and properties of Busemann flow is reviewed, and the axisymmetrical Busemann intakes designed on the basis of such flow are introduced. Then a way to introduce overboard spillage for the Busemann intakes is suggested. A theory to predict the self-starting (Kantrowitz) lines for the Busemann intakes via overboard spillage is then developed. In Chapter 6, three-dimensional numerical simulations of flow starting in the Busemann intakes with overboard spillage are described, and the outcomes

of these numerical experiments are compared with the theoretical predictions from Chapter 5. Finally, Chapter 7 summarizes the obtained results and their implications.

CHAPTER 2
Theory: Ramp Intakes

2.1 Introduction

The planar, or two-dimensional, ramp-type intakes with a rectangular cross-section belong, arguably, to the simplest type of supersonic intakes. Typical representatives of this intake family are the two-shock and Prandtl-Meyer ramp intakes, see Figs. 1–3 and 1–4. By virtue of their design, the tip of the intake's cowl is located downstream from the ramp leading edge, thus resulting in the presence of internal and external compression sections and ensuring overboard spillage of the incoming flow during starting.

The self-starting characteristics of two-shock ramp intakes were considered by Veillard et al. [132]. They analyzed the flowfields of two-shock ramp intakes at all possible combinations of free-stream Mach numbers and angles of the ramp shock to find the minimum area ratio required for intake self-starting (spontaneous starting upon gradual acceleration). In other words, the researchers generalized for the two-shock ramp intakes the classical Kantrowitz limit for spontaneous starting, which was formulated for fully enclosed intakes.

It is to be mentioned that Veillard et al. [132] identified, within the whole intake family, a few specific designs based on a particular flowfield or a particular geometry. For example, the so-called weak and strong shock designs correspond to the started flowfields in which the first oblique shock (the ramp shock) reaches the tip of the cowl

and the second, reflected, oblique shock (the cowl shock), which can be either a weak shock or a strong shock, comes to the trailing edge of the ramp surface. The so-called "normal-line" design is based on the geometrical principle that the line issued from the cowl tip perpendicularly to the ramp surface comes to the ramp trailing edge.

Veillard et al. [132] obtained the limiting self-starting contractions for the entire family of two-shock intakes and observed that these limiting contractions are very close to those for two-shock intakes designed with strong shock. Thus, the strong-shock-based design principle can be viewed as a simple method to achieve the best self-starting characteristics (to minimize the self-starting area ratio). The startability analysis for the two-shock ramp intakes generally following the one in [132] are presented in detail and discussed bellow in Section 2.2.1 for the sake of completeness as well as for it to serve as a logical starting point for the present study.

The Prandtl-Meyer intake is another type of ramp intake with a planar (two-dimensional) geometry. It allows to improve the intake's efficiency (i.e., to decrease the total pressure loss) as compared to the two-shock ramp intakes. As shown in Fig. 1–4, a concave surface is used instead of a straight ramp for deflecting the incoming flow, which results in an isentropic Prandtl-Meyer compression fan. Following the general methodology from [132], the starting characteristics of the Prandtl-Meyer intake family are theoretically studied below in Section 2.2.2 to determine the minimum area ratios required for self-starting of Prandtl-Meyer intakes. Various designs within the constraints of the given intake family are to be considered with the aim of finding the best one in terms of resulting self-starting characteristics. Of particular

interest is to find out whether the strong-shock-based design principle would hold for the Prandtl-Meyer intakes as well.

2.2 Relations for the startability analysis of ramp intakes

The flowfields of the two-shock and Prandtl-Meyer ramp intakes have many common features, as may be seen in Figs. 2–1 and 2–4. Likewise, the startability analysis for the intakes follows the same general steps.

The first important step is to establish the external and internal compression sections. To capture all the incoming stream, the ramp shock or the Mach waves of the Prandtl-Meyer fan should reach the cowl leading edge as shown in Figs. 2–1a and 2–4a. The free-stream flow is processed by the attached oblique shock (the ramp shock) or Prandtl-Meyer fan and directed along the ramp surface. It would be logical to assume that the internal compression section, or, in other words, the fully enclosed intake section, begins from the normal line, which is issued from the cowl leading edge perpendicularly to the ramp surface. The line is shown as A_s area in Figs. 2–1a and 2–4a. It is to be noted that it is assumed that the intake has a width length of one unit. Downstream from that line, the flow is encased by the intake's walls from both sides. The preceding section, in which the flow is bounded by the ramp only from one side, is the external compression section, where overboard spillage is possible. The second step in startability analysis of the ramp intakes is to apply the classical theory (or the Kantrowitz theory; see Section 1.4.2) to the internal compression section. These two steps are followed in detail in the next subsections.

2.2.1 Two-shock ramp intake

Similar to the previous study [132], the free-stream Mach number, M_∞, the shock angle, σ, and the area ratio, A_e/A_i, are chosen as the parameters defining a two-shock ramp intake. At any free-stream Mach number, the shock angle varies from the Mach angle $\sin^{-1}(1/M_\infty)$ to σ_{upper} corresponding to the sonic flow downstream of the ramp shock, i.e. $M_2 = 1$. The deflection angle, δ, for the ramp shock is then given by:

$$\tan\delta = \frac{(M^2\sin^2\sigma - 1)\cot\sigma}{\frac{(\gamma+1)}{2}M^2 - M^2\sin^2\sigma + 1}. \tag{2.1}$$

where $M = M_\infty$.

The Mach number of the flow downstream of the ramp shock is given by $M_2 = M_y \sin(\sigma - \delta)$ where

$$M_y = \sqrt{\frac{2 + (\gamma-1)M_x^2}{2\gamma M_x^2 - (\gamma-1)}}. \tag{2.2}$$

and $M_x = M_\infty \sin\sigma$.

In order to apply the classical theory, a normal shock is placed at A_s location, which is the entry of the fully enclosed section of the intake, see Fig. 2–1b. The Mach number of the flow downstream of the normal shock, M_3, can be found using Eq. (2.2) with $M_x = M_2$. Equation (1.1) for M_3 (or Eq. (1.3) for M_2) gives the area ratio limit for self-starting in terms of the internal compression section area ratio $(A_e/A_s)_{Kantrowitz}$. Finally, using the geometrical relation between A_i and A_s (see Fig. 2–1), the Kantrowitz (self-starting) area ratio for the whole two-shock ramp intake using overboard spillage, $(A_e/A_i)_{Kantrowitz}$, is obtained as follows:

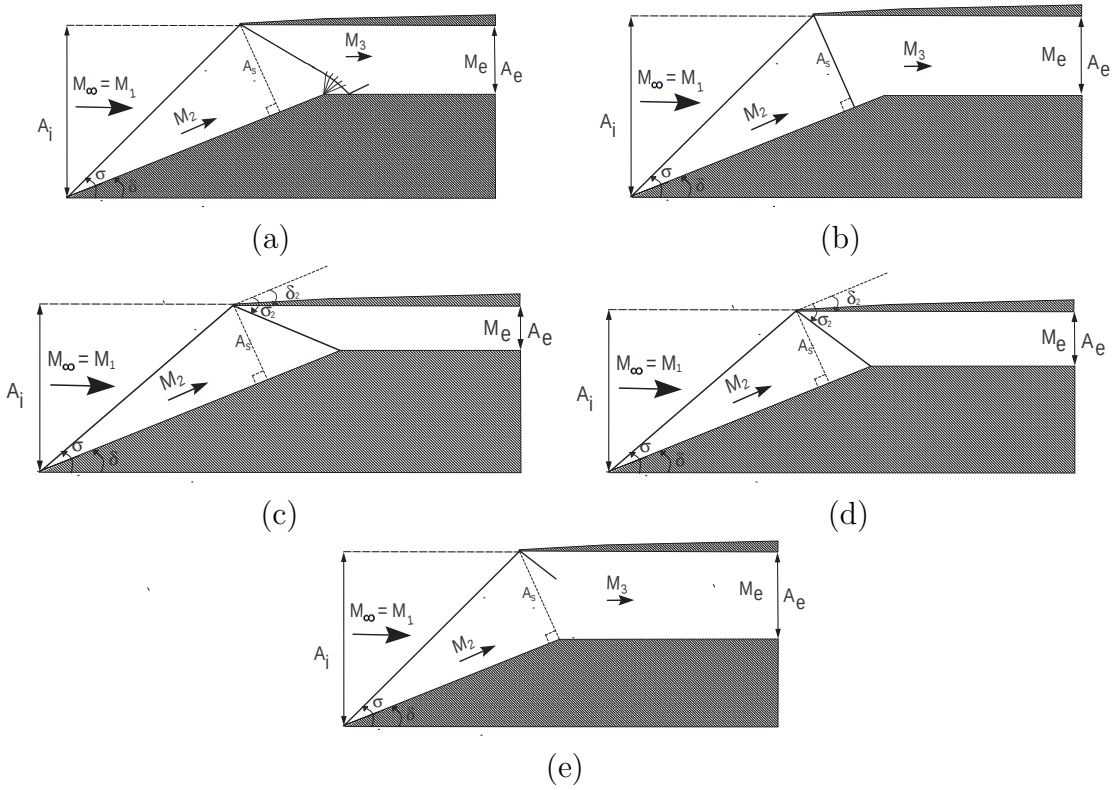

Figure 2–1: Two-shock ramp intake schematics: a) general two-shock ramp intake, b) two-shock ramp intake with normal shock at its internal compression section entry, c) two-shock ramp intake with weak reflected shock, d) two-shock ramp intake with strong reflected shock, and e) normal-line design two-shock ramp intake.

$$\left(\frac{A_e}{A_i}\right)_{Kantrowitz} = \left(\frac{A_e}{A_s}\right)_{Kantrowitz} \frac{\sin(\sigma - \delta)}{\sin(\sigma)}. \tag{2.3}$$

A two-shock ramp intake area ratio A_e/A_i should be equal to or higher than $(A_e/A_i)_{Kantrowitz}$ for the intake to start spontaneously.

It should be mentioned that as seen in Fig. 2–1e, the maximum exit area of an intake is limited to $A_s \cos(\delta)$. Otherwise, the flow at the cross-section A_s, would be non-uniform and the Kantrowitz theory cannot be applied. Another constraint is

that the reflected (cowl) shock must be attached to the cowl leading edge. Otherwise, if the shock detaches and becomes a bow shock at the cowl leading edge, some part of the incoming flow will be spilled over the edge. Therefore, the flow deflection angle for the reflected shock, δ_2, must not exceed the detachment angle for Mach number M_2, i.e. $\delta_2 < (\delta_2)_{max}$. The value of $(\delta_2)_{max}$ can be obtained from Eq. (2.1) with $M = M_2$ and $\sigma = \sigma_{(\delta_2)_{max}}$, where the shock angle $\sigma_{(\delta_2)_{max}}$ is given by [108]:

$$\sin^2(\sigma_{(\delta_2)_{max}}) = \frac{1}{\gamma M_2^2}\left\{\frac{\gamma+1}{4}M_2^2 - 1 + \left[(\gamma+1)\left(1 + \frac{\gamma-1}{2}M_2^2 + \frac{\gamma+1}{16}M_2^4\right)\right]^{0.5}\right\}. \tag{2.4}$$

In the present study (as in [132]), the cowl is considered to be horizontal; therefore, $\delta = \delta_2$ should be used in the above relations.

Thus, Eq. (2.3) and the relevant preceding relations give us the minimum self-starting area ratio of two-shock ramp intakes for any possible combination of σ and M_∞. Among all intakes in the (σ, M_∞) parametric space, there are intakes representing some specific designs such as the intakes with weak reflected (cowl) shock or strong reflected (cowl) shock, which terminates at the ramp trailing edge. Figures 2–1c and 2–1d provide a graphical representation of such designs. In these two-shock ramp intakes, the reflected shock angle can be obtained from:

$$\sigma_2 = \tan^{-1}\left(\frac{\sin\delta}{\cos\delta - \frac{A_e}{A_s}}\right). \tag{2.5}$$

If the shock angle σ_2 is less than $\sigma_{(\delta_2)_{max}}$, the reflected shock is a weak shock and if $\sigma_2 > \sigma_{(\delta_2)_{max}}$, it is a strong shock. The other specific design of intake is the

normal-line design intake. The geometrical relation for the normal-line design is $A_e/A_s = \cos\delta$ (see Fig. 2–1e).

The flowcharts of the theoretical startability analysis process of two-shock ramp intakes are shown in Figs. 2–2 and 2–3. In the process of the startability analysis shown on the flowcharts, the parametric space (σ, M_∞) is explored within the following limits: $1 \leq M_\infty \leq 8$ and $\sin^{-1}(1/M_\infty) < \sigma < \frac{\pi}{2}$ using 1000 points for each variable. As a result, the Kantrowitz area ratio $(A_e/A_i)_{Kantrowitz}$ is obtained for each admissible (σ, M_∞) pair. The results of the analysis are presented and discussed in Section 2.3.1.

It is to be noted that only particular intake designs from the entire parametric space (σ, M_∞) result in uniform exit flow, while in the majority of cases, the exit flow is non-uniform because the reflected (cowl) shock is not terminated at the ramp trailing edge (Fig. 2–1a). In fact, the only design producing uniform exit flow is the weak shock design (Fig. 2–1c). In the case of normal-line design (Fig. 2–1e), the exit flow is obviously non-uniform for the reason stated above. The strong shock design would result in uniform exit flow only if in the started state, the strong shock is indeed maintained by the application of the regained back pressure. In this case, the exit flow is subsonic and significant total pressure losses would be incurred due to the strong shock. Thus, it is likely that in practice such an intake would be operated with a weak reflected shock and, therefore, with a non-uniform exit flow. The strong shock solution would be used for design purposes only.

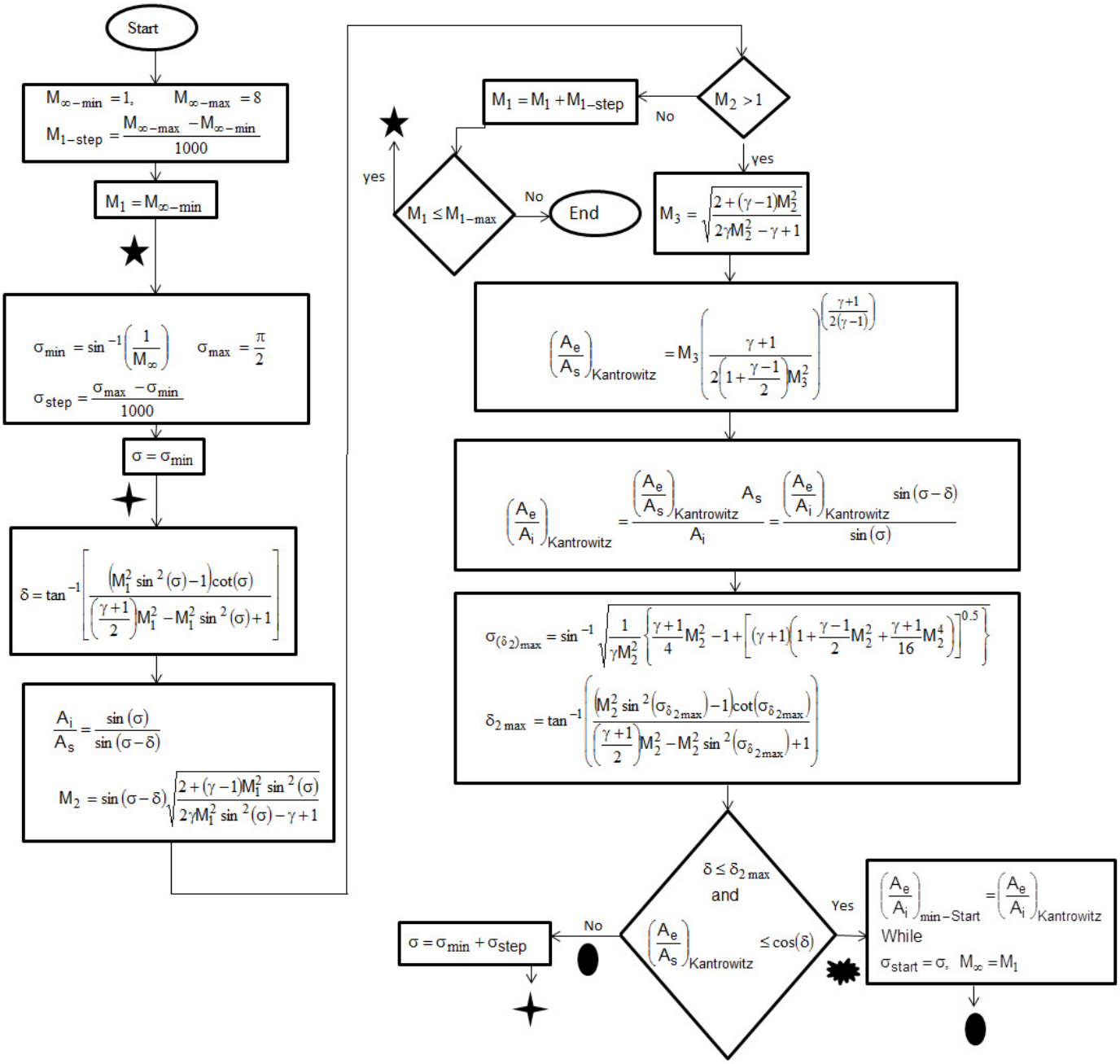

Figure 2–2: The general flowchart of the two-shock intake startability analysis.

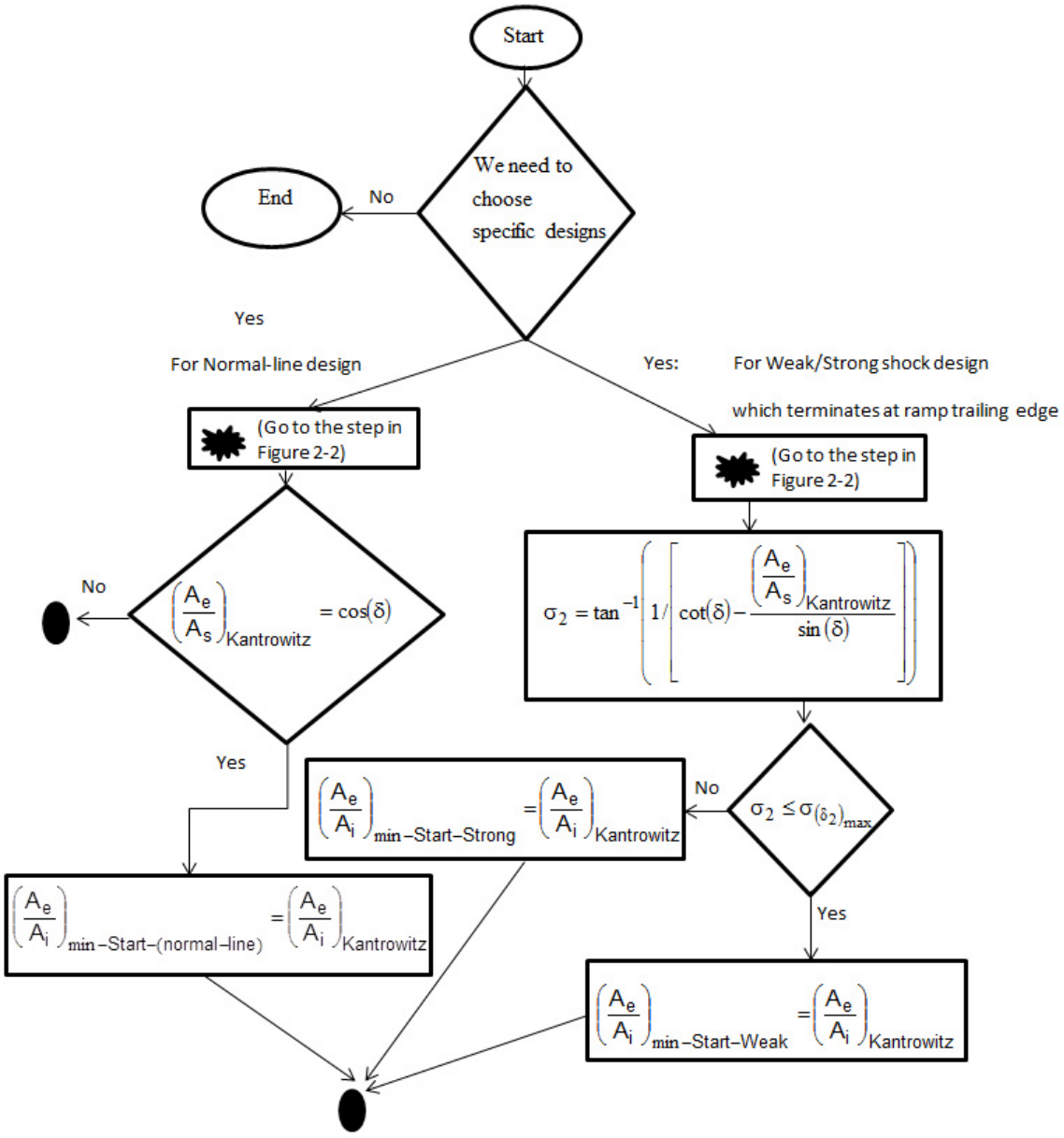

Figure 2–3: The flowchart of the two-shock intake startability analysis for specific designs.

2.2.2 Prandtl-Meyer intake

In the Prandtl-Meyer intakes, the isentropic Prandtl-Meyer external compression fan decreases the flow Mach number from the free-stream value M_∞ to M_2 and turns

the flow by deflection angle δ, as shown in Fig. 2–4a. In the external compression fan, each Mach wave forms the Mach angle $\alpha = \sin^{-1}(1/M)$ with the local flow direction. The Prandtl-Meyer angle as a function of Mach number is given by the following relation [108]:

$$\upsilon = \sqrt{\frac{\gamma+1}{\gamma-1}}\tan^{-1}\sqrt{\left(\frac{\gamma-1}{\gamma+1}\right)(M^2-1)} - \tan^{-1}\sqrt{M^2-1}. \tag{2.6}$$

and the flow deflection angle can be obtained as the difference of the Prandtl-Meyer angles for the free-stream Mach number M_∞ and the Mach number downstream from the fan M_2, i.e. $\delta = \Delta\nu = \nu(M_\infty) - \nu(M_2)$. Thus, the family of Prandtl-Meyer intakes can be defined via the free-stream Mach number M_∞, the deflection angle δ and the area ratio A_e/A_i. The compression angle φ or the Mach number M_2 (see Fig. 2–4a) could be also used as the parameter defining the Prandtl-Meyer intake instead of the deflection angle δ.

To determine the Kantrowitz (self-starting) area ratio $(A_e/A_i)_{Kantrowitz}$ for a given point (M_∞, δ) in the chosen parametric space, the length S, which represents the distance from the starting point of a Mach wave on the ramp surface to the cowl lip (or the focal point of all Mach waves) is introduced (see Fig. 2–4b). The highest S value corresponds to the length of the Mach wave extending from the ramp leading edge to the cowl lip (S_i). For considering of units in subsequent derivations, the length S can be converted to area by multiplying it by the unit width of the intake. Then, such ratio as S/A can be considered to be nondimensional. In fact, likewise, any cross-sectional area A can be converted to length by dividing it by the unit

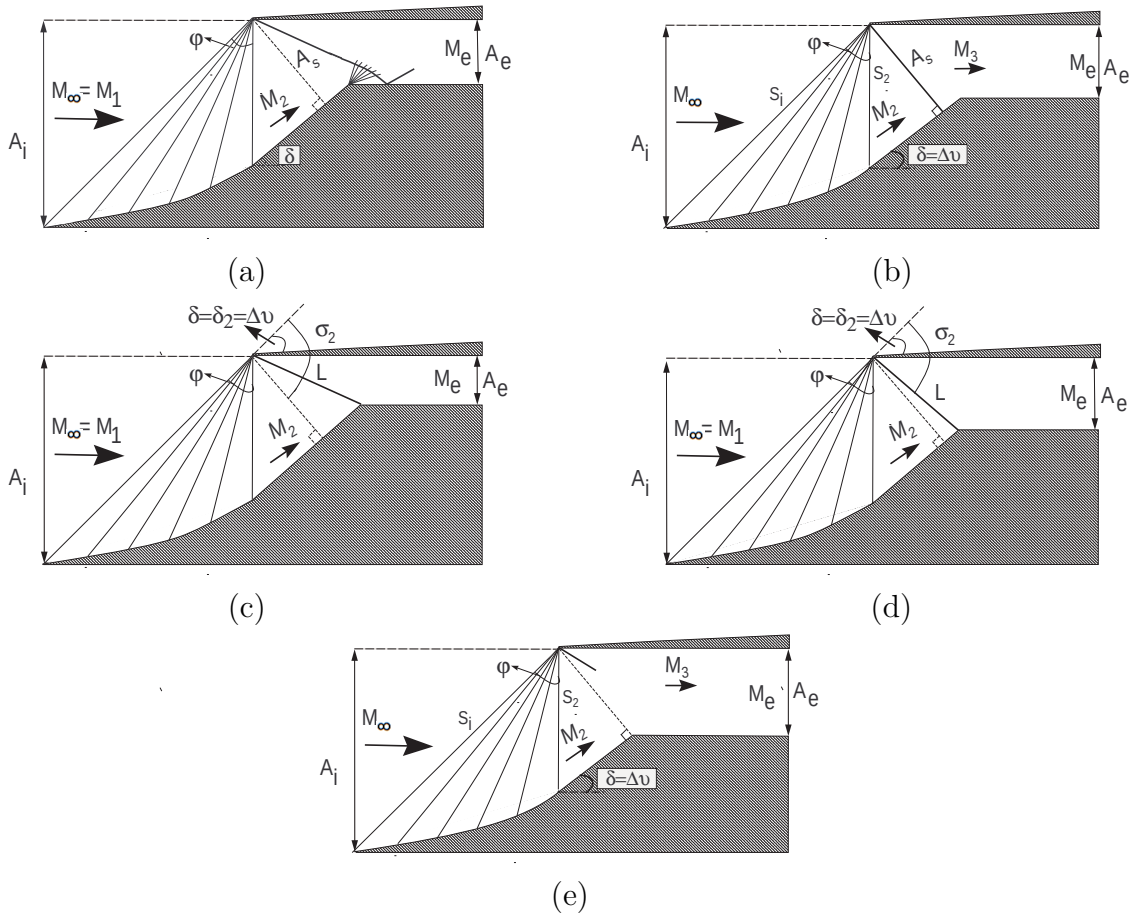

Figure 2–4: Prandtl-Meyer intake schematics: a) general Prandtl-Meyer intake, b) Prandtl-Meyer intake with normal shock at its internal compression section entry, c) Prandtl-Meyer intake with weak shock, d) Prandtl-Meyer intake with strong shock, and e) normal-line design Prandtl-Meyer intake.

width of the intake. The value of S can be calculated on the basis of the geometrical relations illustrated in Fig. 2–5:

$$\sin\alpha = \frac{A}{S} = \frac{1}{M} \Rightarrow A = \frac{S}{M}. \tag{2.7}$$

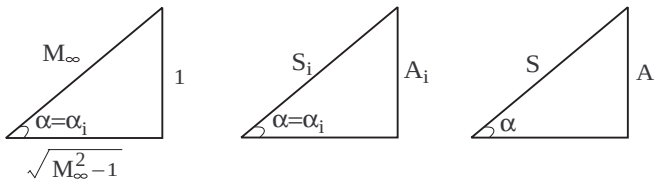

Figure 2–5: Schematics illustrating the relation between the Mach wave length (area) S and the local cross-sectional area A in the Prandtl-Meyer compression fan.

At the imaginary sonic Mach number (in case, the flow is decelerated in the Prandtl-Meyer compression fan to sonic speed ($M_2 = 1$)), one would have from Eq. (2.7) that $A^* = S^*$. Furthermore, since only area ratios are important for the present analysis, it can be assumed that $S^* = 1$. The flow in the fan is isentropic, and, hence, the isentropic Mach-area ratio relation Eq. (1.1) can be used in Eq. (2.7), resulting in:

$$S = \left[\left(\frac{\gamma-1}{\gamma+1}\right)(M^2-1)+1\right]^{\frac{\gamma+1}{2(\gamma-1)}}. \tag{2.8}$$

Applying Eq. (2.7) to the first and the last Mach wave in the fan, one would get

$$A_i = \frac{S_i}{M_1}; \qquad A_2 = A_s = \frac{S_2}{M_2} \qquad \textit{and} \qquad \frac{A_s}{A_i} = \frac{\frac{S_2}{M_2}}{\frac{S_i}{M_1}}. \tag{2.9}$$

where A_s is the flow area downstream from the compression fan as shown in Fig. 2–4a.

As the next step, in order to analyze the startability of Prandtl-Meyer intakes, the minimum self-starting area ratio of the internal compression section should be determined using the classical theory. Therefore, a normal shock is placed at the entry of the fully enclosed section of the intake (Fig. 2–4b, cross-section A_s), and the Mach number of the flow downstream of the normal shock M_3 is calculated using

Eq. (2.2) with $M_x = M_2$. Then, $(A_e/A_s)_{Kantrowitz}$ can be calculated using Eq. (1.1) for M_3 or Eq. (1.3) for M_2. The Kantrowitz (self-starting) area ratio $(A_e/A_i)_{Kantrowitz}$ for whole intake can be then obtained using Eq. (2.10):

$$\left(\frac{A_e}{A_i}\right)_{Kantrowitz} = \left(\frac{A_e}{A_s}\right)_{Kantrowitz} \frac{A_s}{A_i} = \left(\frac{A_e}{A_s}\right)_{Kantrowitz} \frac{S_2/M_2}{S_i/M_1}. \tag{2.10}$$

This area ratio $(A_e/A_i)_{Kantrowitz}$ represents the limit at which or above it a Prandtl-Meyer intake with chosen M_∞ and M_2 (or δ) starts spontaneously.

As it may be seen from Fig. 2–4e, the exit area A_e should not exceed $A_s \cos\delta$. Otherwise, the normal-line issued from the cowl leading edge would be downstream from the trailing edge of the ramp, and the flow in front of the normal shock would become non-uniform due to the expansion wave at the ramp trailing edge. Thus, the intake self-starting area ratio $(A_e/A_s)_{Kantrowitz}$ should be either equal to or less than $\cos\delta$.

Similarly to the case of two-shock intakes, the detachment of the reflected oblique shock from the cowl leading edge would lead to spillage of some flow overboard, and, therefore, should be avoided. Thus, for each Mach number of the flow downstream from the Prandtl-Meyer compression fan, M_2, there is the maximum possible deflection angle, $(\delta_2)_{max}$, corresponding to the maximum reflected shock angle $\sigma_{(\delta_2)_{max}}$. The shock angle $\sigma_{(\delta_2)_{max}}$ for the given M_2 can be obtained from Eq. (2.4), and the maximum deflection angle $(\delta_2)_{max}$ from Eq. (2.1) with $M = M_2$ and $\sigma = \sigma_{(\delta_2)_{max}}$. In this study, as the cowl inner surface is considered to be horizontal, the deflection angles of the compression fan and the oblique shock are equal, i.e. $\delta_2 = \delta$.

To further illustrate the above constraints, Fig. 2–6 shows the Kantrowitz area ratio, $(A_e/A_s)_{Kantrowitz}$, and $\cos\delta$ values as functions of the deflection angle δ for free-stream Mach numbers of 3 and 7. The intersection of these lines gives the maximum δ satisfying the constraint $A_e/A_s \leq \cos\delta$. The intersection of $M_2 = M_2(\delta)$ and $(\delta_2)_{max} = (\delta_2)_{max}(M_2)$ lines is also shown in Fig. 2–6. It gives the maximum δ to have the started intake without the detached bow shock in front of the cowl leading edge. It is clear that the second constraint on δ (related to the shock detachment) is always more restrictive than the first one (related to the flow uniformity at A_s). The implications of this observation are further discussed in Section 2.3.2.

Similarly to two-shock ramp intakes, there are some specific designs of Prandtl-Meyer intakes to be considered. For each deflection angle δ, it is possible to have either a weak reflected shock with smaller σ_2 or a strong reflected shock with larger σ_2. The intakes with the reflected weak/strong shock terminating at the ramp trailing edge represent two specific designs termed weak shock design and strong shock design, see Figs. 2–4c and 2–4d. When the reflected shock terminates at the ramp trailing edge, the shock angle σ_2 can be determined from Eq. (2.5). If the obtained σ_2 is less than $\sigma_{(\delta_2)_{max}}$, the reflected shock is a weak shock and if $\sigma_2 > \sigma_{(\delta_2)_{max}}$, it is a strong shock. There is also a possibility to have the Prandtl-Meyer intake with normal-line design (Fig. 2–4e), in which case A_e is exactly equal to $A_s\cos\delta$. It is to be noted that, as it follows from Fig. 2–6, in the normal-line design intakes, the reflected shock will be always detached from the cowl leading edge, and hence, such intakes may not be considered as started ones (not all incoming flow will be captured).

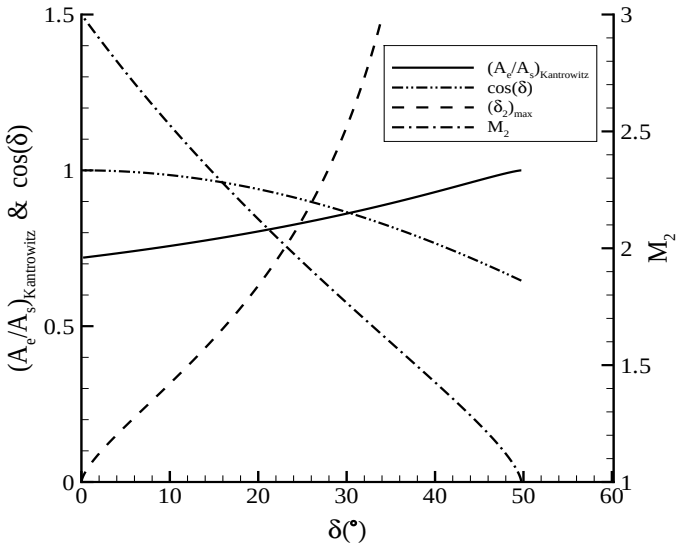

(a) Free-stream Mach number of 3

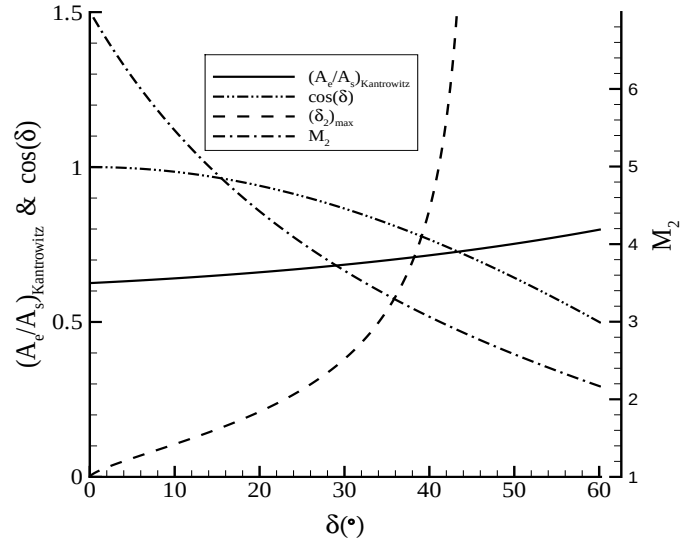

(b) Free-stream Mach number of 7

Figure 2–6: Various geometrical and gasdynamical characteristics of the Prandtl-Meyer intake for two free-stream Mach numbers; the internal compression Kantrowitz area ratio $(A_e/A_s)_{Kantrowitz}$, the Mach number M_2 and $\cos\delta$ are given as functions of the deflection angle δ; the maximum deflection angle $(\delta_2)_{max}$ is given as function of the Mach number M_2.

The flowcharts representing the theoretical startability analysis of Prandtl-Meyer intakes are shown in Figs. 2–7 and 2–8. The startability analysis is performed in the (M_∞, M_2) parametric space. For each considered and admissible (M_∞, M_2) pair, the Kantrowitz (self-starting) area ratio $(A_e/A_i)_{Kantrowitz}$ is obtained. The results of the analysis are presented and discussed in Section 2.3.2.

It is to be noted that similarly to the two-shock intakes, only the weak shock design would lead to the Prandtl-Meyer intake with uniform exit flow. The flowfield with the strong reflected shock is again considered here only as the basis for intake design. The resulting strong-shock-design intakes would most likely be operated with a weak reflected shock and, hence, non-uniform exit flow.

2.3 Results of self-started ramp intake

2.3.1 Two-shock ramp intake

The surface shown in Fig. 2–9a [132] corresponds to the minimum area ratio required for spontaneous starting of two-shock ramp intakes at different free-stream Mach numbers ranging from $M_\infty = 1.01$ to $M_\infty = 8$ and for the ramp shock angles ranging from $\sigma = \sin^{-1}(\frac{1}{M})$ to σ_{upper} (see section 2.2.1). At the lower limit of σ, the deflection angle approaches zero and A_s becomes equal to A_i. Thus, the classical Kantrowitz starting limit is recovered. The upper limit of the ramp shock angle in Fig. 2–9b represents the condition of having sonic flow downstream of the ramp shock ($M_2 \to 1$). The difference between Figs. 2–9a and 2–9b is related to the oblique shock detachment at the cowl leading edge. Figure 2–9a includes all theoretically possible two-shock ramp intakes without reflected shock detachment at the cowl lip.

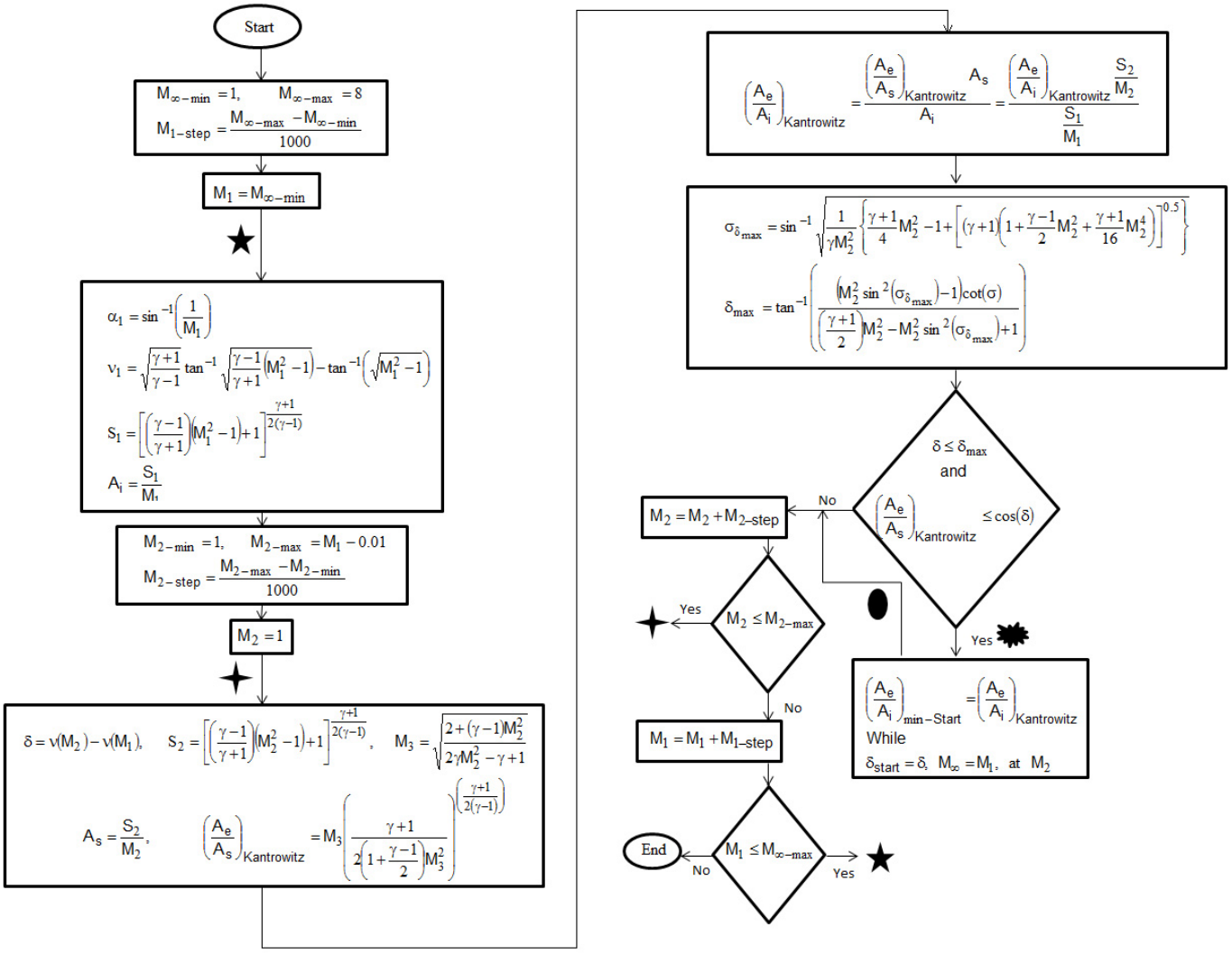

Figure 2–7: The general flowchart of the Prandtl-Meyer intake startability analysis.

In this case, the ramp shock angle upper limit is the value resulting in the post shock Mach number M_2 for which the detachment angle is equal to δ.

The results show that the Kantrowitz limit is lowered using the overboard spillage technique. Furthermore, it is clear from the theoretical results (Fig. 2–9)

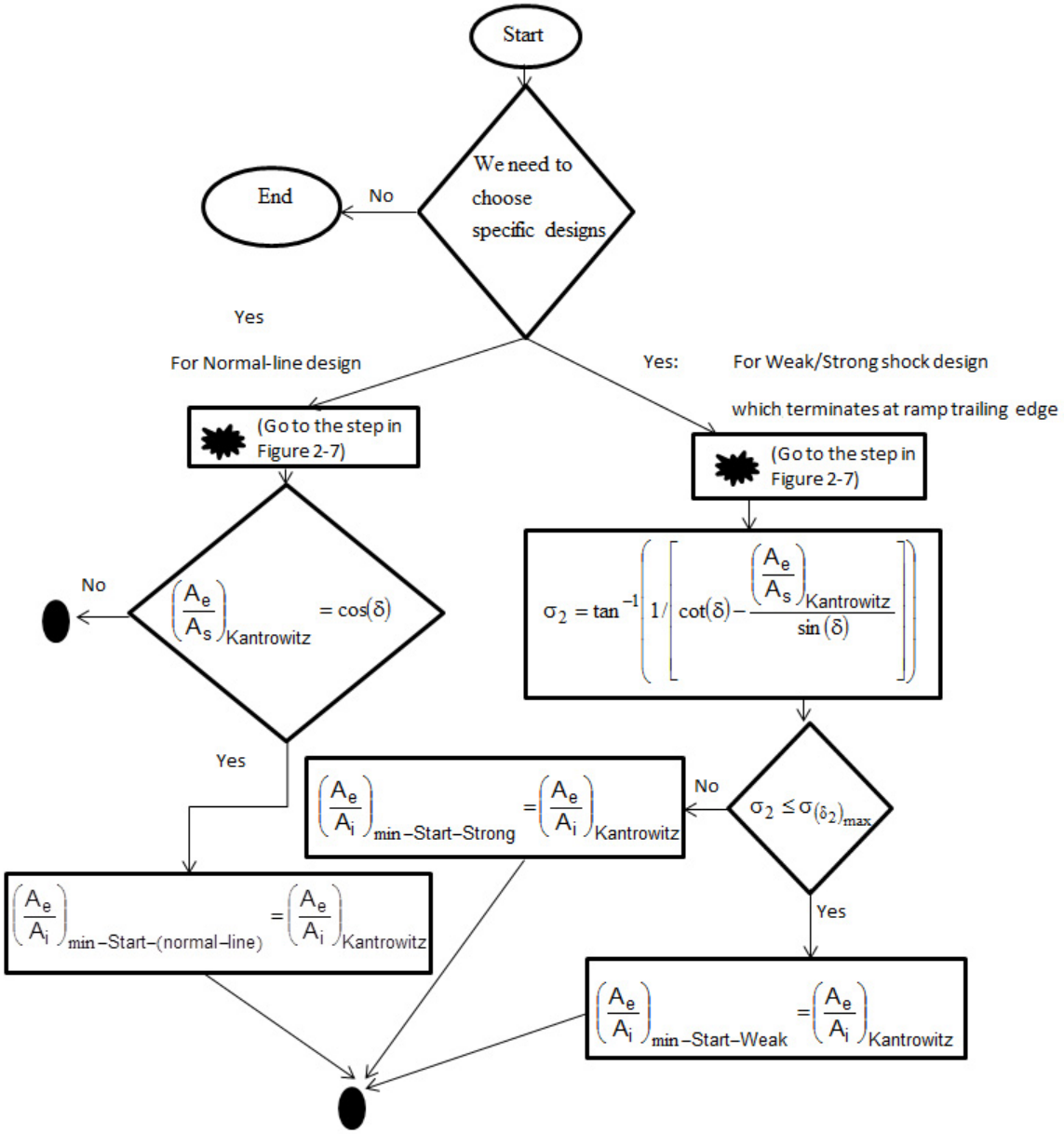

Figure 2–8: The flowchart of the Prandtl-Meyer intake startability analysis for specific designs.

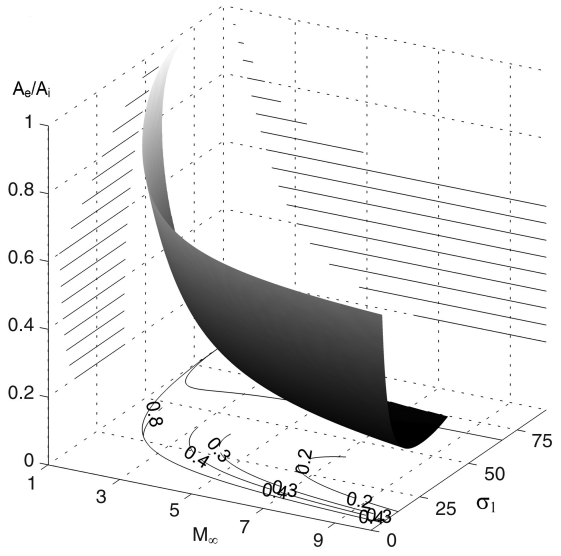

(a)

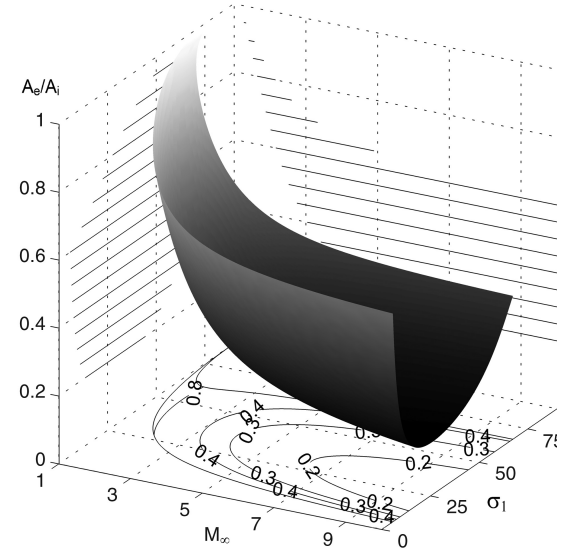

(b)

Figure 2–9: The Kantrowitz surface for two-shock ramp intakes with the upper boundary of the ramp shock angle σ_1 corresponding to: a) detachment of the reflected shock at a horizontal cowl leading edge and b) sonic flow downstream of the ramp shock. Reproduced from [132]

.

that at a given free-stream Mach number, there is an optimal intake geometry providing the best starting characteristics via overboard spillage; one can observe a minimum on the Kantrowitz surfaces of Fig. 2–9. The presence of the optimal geometry may be explained as follows [132]. At a given free-stream Mach number, if the ramp shock angle is increased, the post shock Mach number M_2 is decreased (see Fig. 5 in [132]) which is unfavorable for starting. At the same time, the internal compression section area ratio would increase (and hence, internal contraction would decrease), Fig. 5 in [132], which is favorable for starting. The two effects compete in such a way that an optimal point exists.

In order to get further insight into the usage of the overboard spillage technique for intake starting, the maximum contraction ratios (the minimum area ratios) of two-shock ramp intakes with weak or strong reflected shock and normal-line design intakes can be found as explained in Section 2.2.1. The results for these three designs are shown in Fig. 2–10. The Kantrowitz line of a fully enclosed intake and the isentropic area ratio limit are also shown in Fig. 2–10. As it is seen in Fig. 2–10, in all cases, the starting limit is less than the Kantrowitz value for a fully enclosed intake, which represents the benefit of usage of the overboard spillage technique to improve startability of the two-shock ramp intakes. It is also clear that the Kantrowitz line corresponding to the strong shock design intakes almost coincides with the limiting self-starting contraction line for the whole two-shock intake family. Therefore, the strong shock design principle may serve as a convenient tool to obtain intakes' geometries corresponding to the best starting characteristics. It should be mentioned that

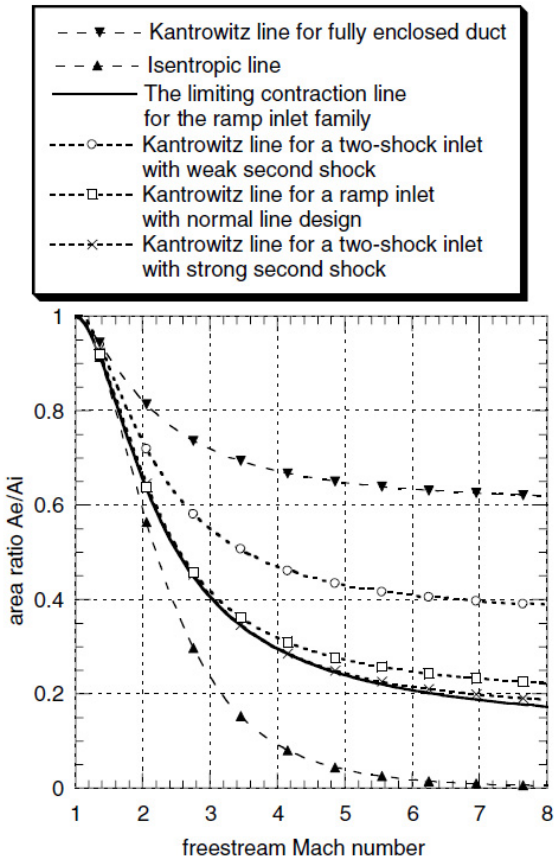

Figure 2–10: The Kantrowitz (self-starting) lines for two-shock ramp intakes of various designs on area-ratio/free-stream Mach number plane. Reproduced from [132].

the normal-line design intakes also exhibit superior starting characteristics. However, as shown in [132] (see Fig. 7), the reflected shock in such an intake cannot be attached to the cowl leading edge. The detachment of the cowl shock would lead to partial incoming flow spillage and, hence, strictly speaking, the normal-line design intakes cannot be started.

2.3.2 Prandtl-Meyer intake

The minimum self-starting area ratios of Prandtl-Meyer intakes are shown in Fig. 2–11 as an elevated surface for (M_∞, δ) parametric space. The derivation of the Kantrowitz surface is explained in Section 2.2.2. It should be noted that even though in Section 2.2.2, the Mach number M_2 is used as one of the defining parameters, it is replaced in Fig. 2–11 with its interchangeable counterpart, the deflection angle δ. This is done to make Fig. 2–11 to more closely resemble Fig. 2–9 for the two-shock intakes, in which the shock angle σ is used as a parameter. This Kantrowitz surface in Fig. 2–11 allows finding the optimal designs from the point of view of maximizing the overboard spillage effect for starting Prandtl-Meyer intakes. The minimum possible deflection angle δ is equal to $0°$. In this limiting case, there would be no flow deflection at all, A_s would be equal to A_i and the classical Kantrowitz limit is recovered. The maximum possible deflection angle δ is dictated by the necessity of having uniform flow entering the internal compression section or, as explained in section 2.2.2, by the condition $A_e/A_s = \cos\delta$. This condition also corresponds to the normal-line design, so that the maximum possible deflection angle belong to the intakes of that design. Unlike the Kantrowitz surface for two-shock ramp-type intakes (Fig. 2–9), which exhibits a minimum, the self-starting surface for the Prandtl-Meyer intakes for a given free-stream Mach number slopes down monotonically with increasing deflection angle between the above mentioned minimum and maximum values. Therefore, for a given free-stream Mach number, the best starting characteristics are achieved at the highest possible deflection angle. When the deflection angle is increasing the self-starting area ratio $(A_e/A_i)_{Kantrowitz}$ is decreasing because, as seen in Fig. 2–6,

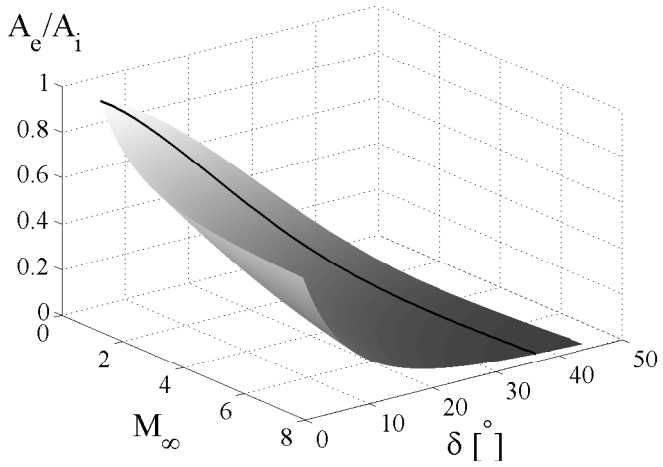

Figure 2–11: The Kantrowitz (self-starting) area ratio for Prandtl-Meyer intakes as a function of free-stream Mach number M_∞ and the deflection angle δ. The black line corresponds to the shock detachment from the cowl leading edge.

the internal compression section area ratio $(A_e/A_s)_{Kantrowitz}$ is increasing which is favorable for starting. However, the rate of $(A_e/A_i)_{Kantrowitz}$ decrease is decreasing (see Fig. 2–11) because of the opposite effect of decreasing the Mach number M_2 in front of the internal compression section, see Fig. 2–6, (that effect is unfavorable for starting). Unlike in two-shock intakes, the influence of M_2 decrease does not result in a minimum point on the Kantrowitz surface. Such influence only reduces the slope of $(A_e/A_i)_{Kantrowitz}$ surface.

It is to be noted that advantageous area ratios close to the normal-line design cannot be used because of the detachment of the reflected oblique shock from the cowl leading edge resulting in a detached bow shock at $\delta > (\delta_2)_{max}$ and flow spillage. The thick black line in Fig. 2–11 shows the maximum δ, which can be used without the cowl shock detachment.

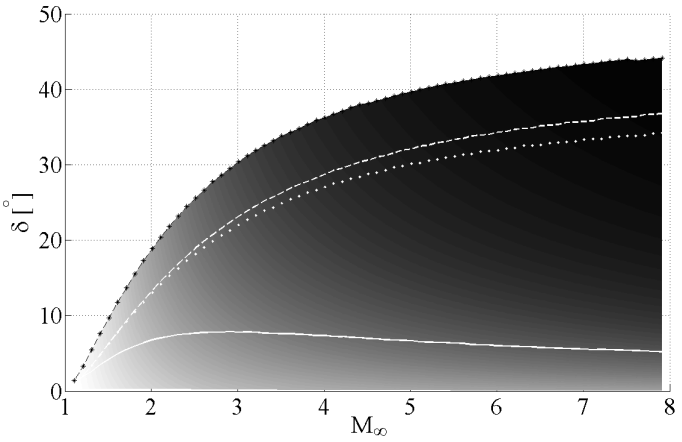

Figure 2–12: Top view of the Kantrowitz surface for Prandtl-Meyer intakes shown in Fig. 2–11. The following lines are shown: Kantrowitz line for a Prandtl-Meyer intake with weak reflected shock (solid); Kantrowitz line for a Prandtl-Meyer intake with strong reflected shock (dotted); the line of reflected-shock detachment from the cowl leading edge (dashed); Kantrowitz line for Prandtl-Meyer intakes with normal-line design (black dash-dotted).

The self-starting area ratios of Prandtl-Meyer intakes at each free-stream Mach number for the normal-line design as well as for the weak shock and the strong shock designs along with the limiting contraction line to have the intake started without a detached shock at the lip of the cowl, are shown in Figs. 2–12 and 2–13. Figures 2–12 and 2–13 may be considered as the top and side views of Fig. 2–11, respectively. The Kantrowitz limit for a fully enclosed intake and the isentropic area ratio limit are also shown for comparison. First of all, the results confirm better startability of Prandtl-Meyer intakes using the overboard spillage technique. Secondly, it is seen that the self-starting line for Prandtl-Meyer intake with normal-line design is lower than the limiting contraction line for the whole intake family, which corresponds to the shock detachment from the cowl leading edge. This should be considered as

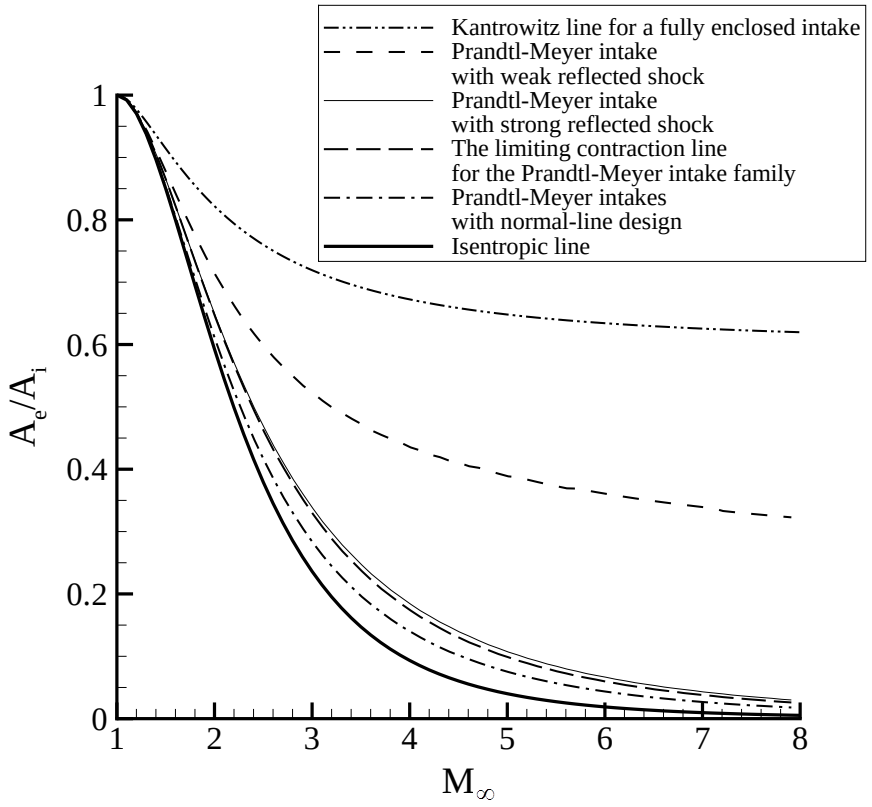

Figure 2–13: The Kantrowitz (self-starting) lines for different Prandtl-Meyer intake designs.

another manifestation of the already mentioned fact: normal-line design intakes with the attached cowl shock do not exist. Finally, the self-starting line for Prandtl-Meyer intakes with strong shock design is only slightly higher than the limiting contraction line for the entire family of Prandtl-Meyer intakes. Therefore, the strong shock design principle, first suggested in [132] for the two-shock ramp intakes, appears to be valid for the Prandtl-Meyer intakes, too. It is also to be noticed that the strong shock design leads to very significant gains in startability as compared to the weak shock design intakes. The respective Kantrowitz line is rather close to the isentropic line.

2.4 Conclusion

In the present chapter, the self-starting characteristics of the Prandtl-Meyer intakes were investigated and compared with those of the two-shock intakes [132]. The Kantrowitz (self-starting) area ratios are obtained in parametric space of free-stream Mach number M_∞ and the deflection angle δ. It is shown that the presence of overboard spillage improves the startability of the intakes as compared to fully enclosed intakes. For a given free-stream Mach number, the minimum self-starting area ratio decreases monotonically when the deflection angle is increased. Therefore, the best starting characteristics (i.e. the limiting contractions) are achieved at the maximum allowable deflection, which corresponds to the detachment of the reflected shock from the cowl leading edge (at $\delta > (\delta_2)_{max}$).

Furthermore, it is found that the Prandtl-Meyer intakes with strong shock design exhibit the self-starting contractions which are very close to the established limiting values for the entire family of the intakes. Therefore, the strong shock design principle appears to be rather general. It can be applied to Prandtl-Meyer intakes to obtained the designs starting at area ratios close to the theoretically established minimum for this intake family.

If total pressure losses are to be minimized and/or a supersonic flow into the combustor is required, the strong-shock design Prandtl-Meyer intake should operate with a weak reflected shock, and, therefore, with a non-uniform flow into the combustor. This can be considered as a 'trade off' of having better starting characteristics.

CHAPTER 3
Methodology of Intake Starting Numerical Experiments

3.1 Introduction

The preceding Chapter 2 presented the theoretical startability analysis of ramp intakes. Conceptually similar startability analysis for Busemann intakes is given in Chapter 5. These theoretical findings are to be verified via numerical experiments on intake starting. For the comparison of the theoretical predictions and the outcomes of numerical starting trials to be meaningful, it is necessary to ensure that the numerical method and codes as well as the procedures of numerical experiments faithfully reproduce the underlying assumptions of the theoretical treatments. The present Chapter 3 is devoted to detailed discussions of the methodology of intake-starting numerical experiments.

At first (Section 3.2), the consequences of the necessity to consider only so-called "on-design" intakes are considered. The next Section 3.3 is devoted to the quasi-steady flow assumption and the means to ensure the validity of this assumption in numerical starting trials. As a result, the most appropriate flow acceleration and grid resolution are determined. Then (Section 3.4), the general characteristics of the 2D and 3D Euler adaptive unstructured finite-volume flow solvers used in this study to simulate the inviscid, non-heat-conducting flows of calorically perfect gas are reviewed. In Section 3.5, more details about the mesh sizes and boundary conditions

used in subsequent numerical simulations are given. Finally (Section 3.6), the steady analysis in numerical studies are discussed.

3.2 Modeling of on-design intake starting

In this study, the theoretical startability considerations implicitly assume that the intake is always on-design. In other words, along any trajectory on the Kantrowitz diagram not only the free-stream Mach number but also the area ratio of the intake (and hence its geometry) changes continuously, in correspondence with the particular design principle of the intake under consideration. For example, in the analysis of two-shock intakes, the ramp angle and the cowl leading edge location should be changed along with decreasing or increasing the area ratio. In the analysis of Busemann intakes, when varying the area ratio of the intake, the conical shock angle and, consequently, the intake wall contour are to be changed as well.

Reproduction of that in numerical experiments would require modifying the intake's geometry in the course of each computational run, at each time. The codes used in the present work do not have provisions for variable geometry. Therefore, numerical validation of theoretical starting boundaries requires multiple runs conducted in the following manner. A point $(M_\infty, A_e/A_i)$ is chosen on the Kantrowitz diagram in the vicinity of the theoretical starting boundary for that particular intake family. The geometry of the intake is calculated in correspondence with the chosen $(M_\infty, A_e/A_i)$ pair and the design principle of the intake. For example, for the two-shock intake with the strong reflected shock, the cowl leading edge and ramp trailing edge coordinates are determined from the condition of having the incident and reflected shocks as shown in Fig. 2–1d. Then, the intake is accelerated from

zero velocity to its design free-stream Mach number M_∞, resulting in either started or unstarted outcome after reaching the steady state condition at the design point. Such experiment is repeated for lower and/or higher design area ratios for the same design Mach number to narrow the difference between the highest area ratio resulting in unstarted flow and the lowest area ratio resulting in started flow. In this way, the self-starting boundary of the on-design intake is determined with the accuracy corresponding to the difference between these two area ratios.

It should be emphasized that further acceleration from an unstarted design point with the goal of starting via overspeeding would not produce the theoretical self-starting point because during such an experiment the area ratio and intake geometry would remain "frozen" and would not correspond to the changing free-stream Mach number. Therefore, the intake would become "off-design", thus not satisfying the always-on-design principle underlying the theoretical considerations. It is indeed possible to predict such off-design starting, at least for relatively simple intake geometries (see [139]), but this line of investigation is beyond the scope of the present research.

3.3 Modeling of quasi-steady flow

The classical Kantrowitz theory itself and all theoretical startability considerations taking into account overboard spillage are based on the quasi-steady assumption, i.e., during the starting process the free-stream velocity is assumed to vary gradually so that the starting process is considered as a sequence of steady states. To reproduce this quasi-steady condition in numerical experiments, it is necessary

to increase the free-stream velocity V_∞ with sufficiently low acceleration a from zero to a value corresponding to chosen M_∞.

A scale analysis in the proceeding studies [81, 104] indicates that the intake starting process may be considered quasi-steady if the characteristic time of acceleration, V_∞/a, is much greater than the characteristic time L/c_∞ of disturbance propagation along the intake's length L, where c_∞ is the free-stream speed of sound, i.e, $V_\infty/a \gg L/c_\infty$, or $a \ll M_\infty c_\infty^2/L = a_{crit}$. For a 5m long intake at sea level ($c_\infty = 345m/s$) and $M_\infty = 5$, we get $a_{crit} \sim 10^4 g$, where g is the free fall acceleration. It may be more instructive to compare the acceleration a with a reference value a_{ref} more pertinent to the flow under consideration. One may choose $a_{ref} = a_{crit}$. Then, for $a = a_{crit} \sim 10^4 g$ the non-dimensional acceleration $\bar{a} = a/a_{ref}$ would be equal to 1; for $a = 10^3 g$, it is equal to 0.1, and for $a = 100g$, $\bar{a} \sim 0.01$.

It would be safe to assume that for $a \simeq 100g$, the condition $a \ll a_{crit}$ is met and the quasi-steady assumption is closely obeyed. However, computations with acceleration of $100g$ are very time-consuming, especially in view of the necessity of multiple runs including those for 3D geometries. In the present work, computations were performed with both $a = 100g$ and $a = 1{,}000g$ for selected 2D and 3D cases. It is found that the starting outcome remains the same for both accelerations. The numerical computations using either an acceleration of $100g$ or $1{,}000g$ have an accuracy of 0.1% in 2D analysis and 1% in 3D analysis in terms of area ratio. These accuracies are corresponding to the difference between the minimum area ratio of the started intake and the maximum area ratio of the unstarted one at each considered

case. Therefore, $a = 1{,}000g$ can be used in self-starting numerical experiments if such accuracy is acceptable. More detailed information is provided below.

A two-shock ramp intake at a free-stream Mach number of 3.5 with a shock angle of 30° (the deflection angle is 15.784°) is simulated numerically. Its minimum area ratio required for spontaneous starting is found using flow accelerations of $100g$, $1{,}000g$ and $10{,}000g$. At the same time, to reveal the possible influence of grid resolution on the starting outcome, the analysis is done for six different grid resolutions, from zero to five levels of grid refinement. Each refinement level decreases the minimum grid step by a factor of two. As shown in Table 3–1, when the acceleration is equal to $10{,}000g$, the flow is unsteady ($a \sim a_{crit}$) and the achieved minimum starting area ratio is lower than the theoretical one (0.370314) and the values obtained with lower accelerations, especially in the cases with grid refinement levels greater than 3. It may be conjectured that higher flow acceleration produces higher volumetric force which pushes the flow toward the exit and helps to start the intake with a lower area ratio. The comparison of the results with flow accelerations of $100g$ and $1{,}000g$ shows no significant difference. The results (Table 3–1) also show that by increasing the resolution up to 3 refinement levels, the starting area ratio is changed but at higher resolutions, it remains constant. Thus, the grid refinement level of 3 appears to be sufficient for subsequent studies.

Table 3–1: Startability analysis of the two-shock ramp intake at $M_\infty = 3.5$ and $\sigma = 30°$. The theoretical minimum starting area ratio is 0.370314.

Flow acceleration	Resolution	Minimum area ratio to get started [1]
$10{,}000g$	0	0.353
	1	0.358
	2	0.360
	3	0.350
	4	0.346
	5	0.347
$1{,}000g$	0	0.367
	1	0.369
	2	0.373
	3	0.376
	4	0.376
	5	0.376
$100g$	0	0.367
	1	0.370
	2	0.373
	3	0.376
	4	0.376
	5	0.376

It is to be emphasized that in the present chapter, we are concerned with the dependance of self-starting area ratio on flow acceleration and grid resolution. The discrepancies, if any, between the theoretical values and acceleration/grid-independent numerical results will be discussed in the subsequent chapters.

[1] The accuracy of 0.1% in terms of area ratio is chosen for 2D analysis. It means that for example when the minimum area ratio of the started intake is 0.376, the maximum area ratio of the unstarted intake is 0.375.

Table 3–2: Startability analysis of three Prandtl−Meyer intakes at $M_\infty = 3$ with grid refinement level equal to 3. The theoretical minimum starting area ratios are respectively 0.47248, 0.44128, and 0.38902.

Deflection angle	Acceleration	Minimum area ratio to get started
10.639	$10{,}000g$	0.451
	$1000g$	0.473
	$100g$	0.473
12.603	$10{,}000g$	0.395
	$1000g$	0.442
	$100g$	0.442
16.746	$10{,}000g$	0.324
	$1000g$	0.389
	$100g$	0.389

A similar study is done for Prandtl-Meyer intakes. At a free-stream Mach number of 3 and deflection angles of 10.639°, 12.603° and 16.746°, the minimum self-starting area ratios of started Prandtl-Meyer intakes are found when the flow accelerations are $100g$, $1{,}000g$ and $10{,}000g$, see Table 3–2. It is again verified that the acceleration of $10{,}000g$ results in unsteady flow and marked deviation of the obtained minimum self-starting area ratios from the ones for lower accelerations and from their theoretical values. At the same time, there is no difference between the results for $a = 1{,}000g$ and $a = 100g$.

Based on the above two-shock ramp intake study, three refinement levels are used to obtain the results for Prandtl-Meyer intakes in Table 3–2. To additionally verify the influence of grid refinement for Prandtl-Meyer intakes accelerated with $a = 1{,}000g$, the minimum area ratios A_e/A_i for spontaneous starting at $M_\infty = 3$ and $\delta = 16.746°$ are found with refinement levels from 0 to 5. As seen in Table 3–3, there

Table 3–3: Startability analysis of the Prandtl−Meyer intake with deflection angle of 16.746° at $M_\infty = 3$ with different grid refinement levels.

Resolution	Minimum area ratio to get started
0	0.382
1	0.386
2	0.385
3	0.389
4	0.389
5	0.389

is no difference between the results for 3, 4, and 5 refinement levels. Therefore, it is confirmed that three refinement levels are sufficient for simulations of Prandtl-Meyer intakes, too.

In 3D studies, at free-stream Mach number of 3, the minimum self-starting area ratio of a half-Busemann intake with weak conical shock (see Chapter 5 for details about its design) is found to be equal to 0.6 with accuracy of 1% for both accelerations of $100g$ and $1{,}000g$, i.e., in other word, using both accelerations result in the maximum area ratio of 0.59 for unstarted half-Busemann intake with weak conical shock at $M_\infty = 3$. Therefore, it is confirmed that there is no difference between using $100g$ and $1{,}000g$ accelerations in this numerical study, neither in 2D simulations nor in 3D ones.

In 3D analysis, grid resolutions from 0 to 3 refinement levels are used to find the minimum self-starting area ratio of a half-Busemann intake with strong conical shock (see Chapter 5 for details of its design) at $M_\infty = 3$. The results are the same within the accuracy of 1%. It is possible that the influence of grid refinement would be revealed in more accurate computations, which are very time-consuming. In the

present work, 1% accuracy of self-starting area ratios in 3D simulations is considered to be sufficient for comparison with theoretical predictions.

Further savings in computational time are possible if one begins the acceleration not from zero velocity but from an unstarted flow at a free-stream Mach number lower than the design Mach number, e.g., from $M_\infty = 2.85$ for $M_{design} = 3$. This can be achieved by, first, computing the unstarted steady state flowfield in the intake designed for $M_{design} = 3$ with the closed exit (the solid wall boundary condition) at, for example, $M_\infty = 2.85 < 3$. Sudden insertion of the intake into $M_\infty = 2.85$ free-stream can be used as the initial condition. Then, after achieving a steady state, the exit is suddenly opened (the low pressure boundary condition at the exit), and the computation proceeds until a new steady state is reached. If this steady state corresponds to unstarted flow, it serves as the initial condition for subsequent free-stream flow acceleration towards $M_\infty = M_{design} = 3$. If not, an initial Mach number of $M_\infty < 2.85$ should be chosen and the process should be repeated.

In order to verify the accuracy of the above approach, the minimum self-starting area ratios of various intakes (two-shock ramp intakes, Prandtl-Meyer intakes and Busemann intakes), which are designed for Mach number of 3, are found. The initial condition is the sudden insertion of the intakes with closed exit into $M_\infty = 2.85$ free-stream, and, subsequently, flow acceleration of $1{,}000g$ is used. The results along with the intakes' properties, are listed in Table 3–4. It is clear that both methods give the same results; therefore, when computational time is an issue (typically, in 3D studies), the above method of beginning the acceleration stage, not from zero velocity but from an unstarted flow at a slightly lower Mach number can be used.

Table 3–4: Startability analysis of various intakes at $M_{design} = 3$ using acceleration of $1{,}000g$ and different initial Mach numbers.

Intake type	Intake's properties	$(\frac{A_e}{A_i})_{start}$ when $(M_\infty)_{initial} = 0$	$(\frac{A_e}{A_i})_{start}$ when $(M_\infty)_{initial} = 2.85$
Two-shock	$\sigma = 25°$	0.536	0.536
	$\sigma = 30°$	0.463	0.463
Prandtl-Meyer	$\delta = 12.603°$	0.442	0.442
	$\delta = 16.746°$	0.389	0.389
Busemann with weak-conical-shock	capture angle = 180°	0.60	0.60
	capture angle = 270°	0.58	0.58

Furthermore, it turns out that the above approach can be applied directly at the design point, i.e., at first, an unstarted steady state with the closed exit for $M_\infty = M_{design}$ is established as the initial condition. Then, the exit is opened and the computation proceeds until reaching the final started or unstarted steady-state. Strictly speaking, the sudden exit opening induces an unsteady flow which potentially may alter the starting outcome [81]. However, even in [81] it is indicated that, in contrast to sudden opening of the intake entry, unsteady flow induced at the exit does not influence the self-starting limits considerably. In agreement with that our 3D numerical experiments show that the starting outcome with sudden exit opening is the same as the one resulting from gradual acceleration. Therefore, this method can be also used instead of the more time-consuming accelerative one, especially in 3D computations.

3.4 Numerical methods and codes

The theoretical intake startability analysis in this study is based on the assumption of inviscid, non-heat-conducting flow of an ideal gas with constant specific heats. Accordingly, in order to numerically simulate 2D and 3D intakes and analyze their startability in quasi-steady flow as explained in the previous sections, two Euler finite-volume flow solvers are used, namely, a 2D/axisymmetric flow solver Masterix [140] and a 3D code Candifix [141].

Both codes features are essentially the same. Numerical methods are conceptually similar to the MUSCL-Hancock method [142, 143]. Unstructured grids with triangular and tetrahedral elements are used to discretize 2D/axisymmetric and 3D computational domains, respectively. Both codes employ local grid adaptation via the classical h-refinement to achieve high resolution of localized flow features (e.g., discontinuities) at low computational cost. Control volumes are established around grid nodes. A linear reconstruction with a TVD limiter is applied to achieve the second order of approximation in space on smooth solutions and avoid spurious oscillations near discontinuities. The second order in time is achieved via a two-step predictor-corrector procedure. The fluxes across control volume faces are determined via a Riemann solver.

Unstructured grid generation in 2D is performed using a 2D unstructured grid generator which is a part of the Masterix software package. Three-dimensional tetrahedral unstructured meshes are generated using existing open source software; specifically, the OpenCASCADE library [144] is used for parameterizing the surfaces directly from the solid model (CSG), and the Netgen library [145] is used to generate

both the surface and the volume meshes. The code Masterix features built-in post-processing capabilities while for postprocessing of 3D flowfields a stand-alone utility Renderix [146] is used.

3.5 Setting up the numerical codes

To initiate a computational experiment two important preparatory steps should be considered: 1) Mesh generation and finding and adjusting the appropriate mesh size; 2) Initial and boundary conditions' specification. These steps are discussed in the next subsections.

3.5.1 Mesh generation

Typical computational domain for numerical intake starting trials includes the intake's interior as well as an external domain, as shown in Figs. 3–1 and 3–2. The external domain is necessary to accommodate the bow shock and spilling flow in case of unstarted flow configuration.

Different background meshes are used inside the intake and within the surrounding area in order to achieve more accurate results, especially in the areas which include shocks and other waves. The mesh generation and mesh sizes used with Masterix and Candifix codes are explained below.

Typical triangular unstructured meshes for 2D computations are shown in Fig 3–1. The rectangular computation domain has an approximate height of $\sim 6L$ and length of $\sim 15L$, where L is the intake's exit cross-section length ($A_e = L \times 1$). As it is seen, three main regions with different grid steps are specified. The smallest grid steps are limited to $0.05L$, whereas the largest ones are kept below $0.3L$, approaching the far-field boundaries of the computational domain. Mostly, in exit region of

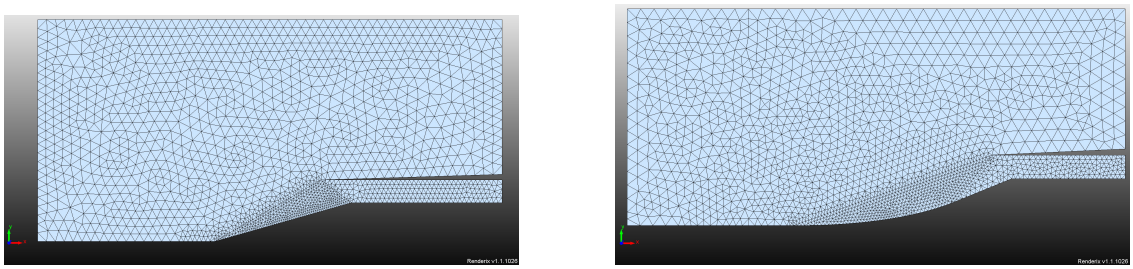

(a) Two-shock ramp intake (b) Prandtl-Meyer intake

Figure 3–1: The computational domains and the baseline triangle meshes for 2D intake starting experiments.

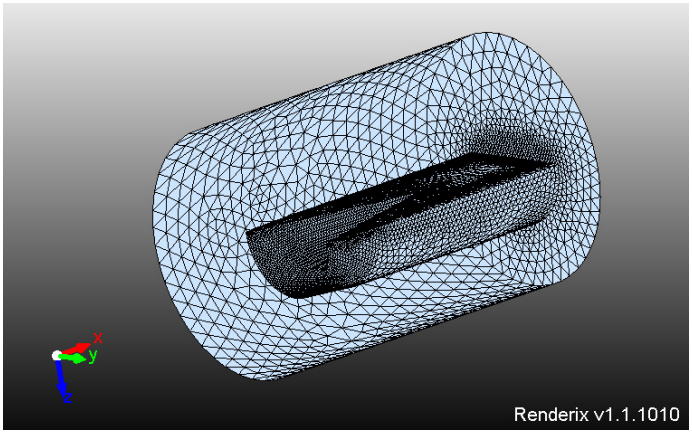

Figure 3–2: The computational domain and the baseline tetrahedral mesh for 3D intake starting experiments (a half-Busemann intake).

the intakes, the grid steps are about $0.08L$. It is clear that to better resolve flow features, finer mesh is used in the regions where shocks and Mach waves are expected. The typical background (baseline) mesh contains $\sim$ 5,000 nodes. In the course of computation, due to local grid adoption, this number maybe increased up to 10,000 nodes, depending on the number of refinement levels used, see Fig. 3–3.

A typical tetrahedral unstructured mesh for 3D computations is shown in Fig. 3–2. The computation domain is enclosed by a cylinder with approximate dimensions

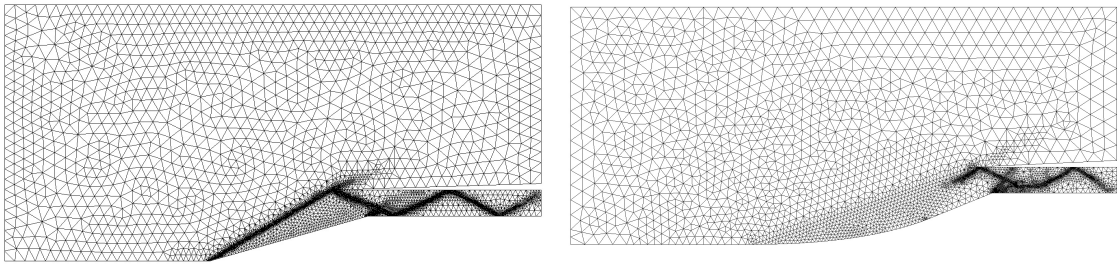

(a) Two-shock ramp intake (b) Prandtl-Meyer intake

Figure 3–3: The view of grids in the course of computations for 2D intake starting experiments.

$\sim 5.8R \times \sim 4.2R$ (height vs. diameter), where R is the radius of the intake's entry cross-section ($A_i = \pi R^2$). It consists of approximately 0.5M tetrahedral cells (around 100,000 grid nodes), with linear size of $0.05R$ near the intake's wall boundaries. The smallest cells, near delicate geometric features, are limited to $0.001R$, whereas the largest cells are kept below $0.3R$, approaching the far-field boundaries of the computational domain. In the course of computation and adoptive refinement, the number of grid nodes and tetrahedral cells varies in a following ranges: $110{,}000 - 210{,}000$ and 0.5M-1.2M, respectively similar to what is shown in Fig. 3–4.

3.5.2 Initial and boundary condition

In the startability analysis of all types of intakes, the free-stream properties are specified at the external boundaries of computation domains. The impermeable wall boundary condition is used on all boundaries corresponding to the intake's surfaces. At the exit of the intake a low pressure value (free-stream pressure) is specified. Proper accounting for incoming and outgoing disturbances at all boundaries is achieved via a Riemann problem solution. As initial conditions, free-stream values are usually used in the whole computational domain.

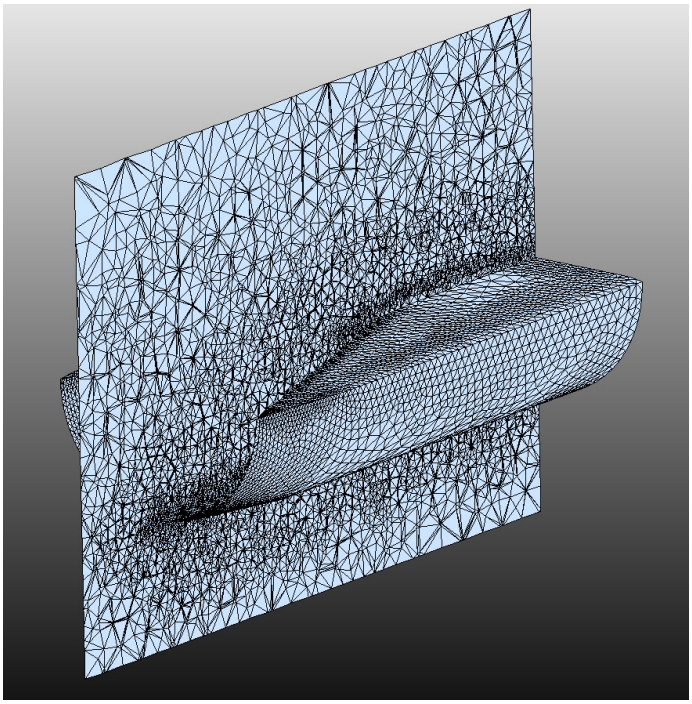

Figure 3–4: The view of grids in the course of computations for 3D intake starting experiments (a half-Busemann intake).

It is to be noted that in the numerical model and the codes no assumptions are made regarding flow symmetry of any kind or particular flow features/characteristics.

3.6 Steady-state convergence analysis

All numerical starting trials are continued until a final (started or unstarted) steady-state is reached. Achieving the steady-state condition can be controlled by plotting the histories of residuals of different flow properties, such as density or velocity or pressure. Figures 3–5a and 3–5b show two samples of the flow steadiness analysis of ramp intakes while Figs. 3–5c and 3–5d show two samples of the flow steadiness analysis of Busemann intakes. It is to be noted that the values of residuals are rather low throughout the whole computation because the free-stream flow

acceleration is chosen to be deliberately low to ensure that the numerical starting process would resemble a quasi-steady process as closely as possible (see Section 3.3). However, it is clear from Fig. 3–5 that during the starting process the residuals are changing. Eventually, when either the bow (starting) shock leaves the computation domain through the intakes's exit or stabilizes in front of the internal compression section, the residuals become to fluctuate around a low constant value. Then, it is assumed that the steady state has been reached.

3.7 Conclusion

The methodology of intake starting numerical experiments presented in this chapter allows to reproduce in numerical modeling two main assumptions used in the theoretical analysis: quasi-steady flow throughout the intake and on-design intake starting. The limiting contractions for on-design intake starting are obtained by conducting starting experiments at many design points. The best methods to satisfy the quasi-steady flow assumption in a computationally efficient manner are: 1) in 2D simulations, to increase the flow velocity with $1{,}000g$ acceleration; 2) in 3D analysis, to begin with the sudden insertion of the intake with closed exit into $M_\infty < M_{design}$ free-stream, get the unstarted steady state at $M_\infty < M_{design}$ and then, accelerate the flow to $M_\infty = M_{design}$ with $1{,}000g$ acceleration. These methods reduce the time needed for each computational run. It is also shown that the refinement level of three gives quite accurate (0.1%) results in 2D startability analysis while the refinement level does not have any marked effect in 3D analysis within 1% accuracy.

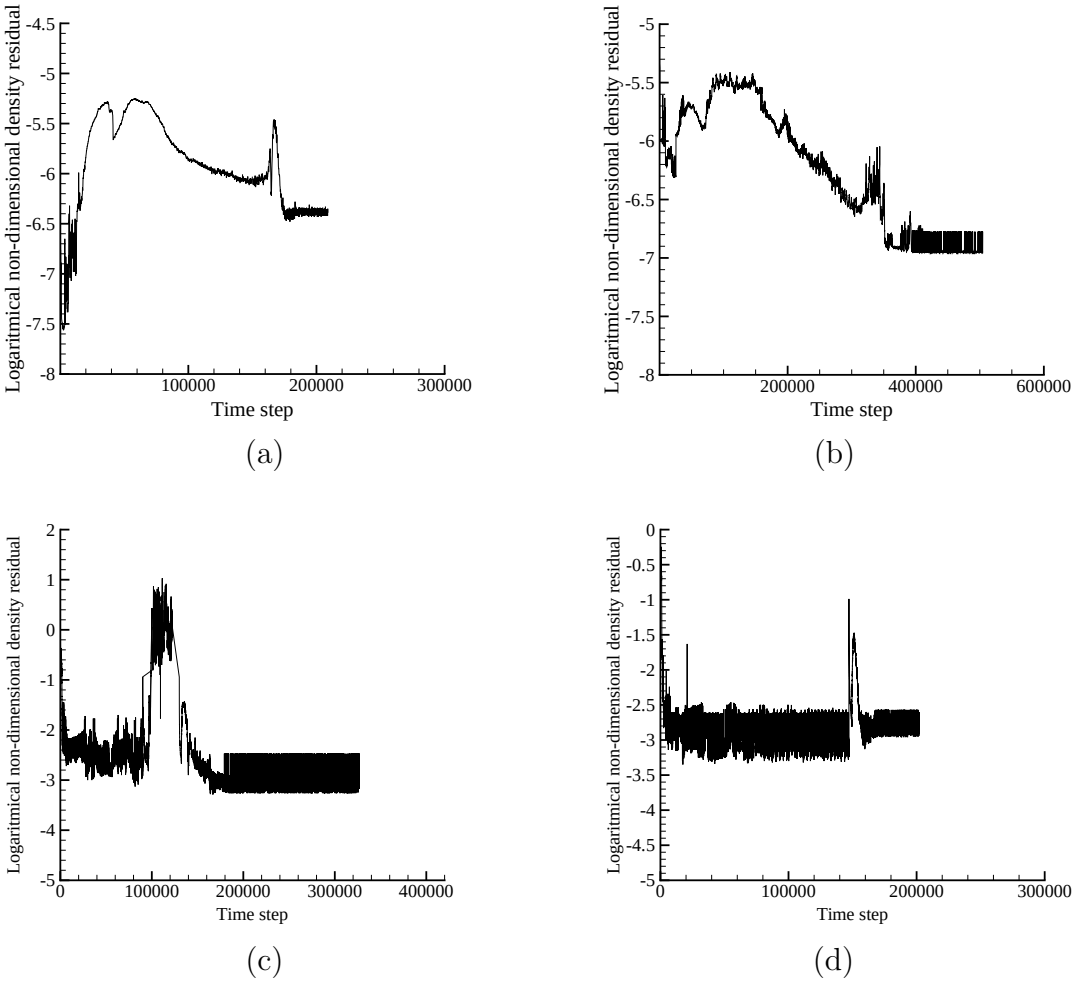

Figure 3–5: Typical residual histories in numerical studies of intake starting: a) two-shock ramp intake at $M_\infty = 3$ with $\sigma = 25°$ and $(\frac{A_e}{A_i})_{start} = 0.533$, b) Prandtl-Meyer intake at $M_\infty = 3$ with $\delta = 22.0386°$ and $(\frac{A_e}{A_i})_{start} = 0.336$, c) half-Busemann intake with weak conical shock with $(\frac{A_e}{A_i})_{start} = 0.57$, d) half-Busemann intake with strong conical shock with $(\frac{A_e}{A_i})_{start} = 0.42$.

CHAPTER 4
Computational Startability Analysis of Ramp Intakes

4.1 Introduction

Computational analysis of on-design ramp intakes is carried out for five different free-stream Mach numbers of 2.5, 3.0, 3.5, 4.0 and 4.5 in order to find the maximum self-starting contraction ratios (the minimum self-starting area ratios) of the intakes. These free-stream Mach numbers are chosen having in mind the characteristics of the available experimental facility (the supersonic wind tunnel [147]) so that to be able to compare the experimental and numerical results in future studies. The two-shock ramp intakes with various ramp shock angles, σ, as well as the Prandtl-Meyer intakes with different Mach numbers downstream of the Prandtl-Meyer fan, M_2, or with different deflection angles, δ, are simulated. Non-uniformity of exit flow of started intakes is discussed.

4.2 Ramp intake geometry calculation

Any numerical intake starting experiment begins with the determination of the geometry of the intake to be simulated. The next two subsections describe some details of this procedure for the two-shock and the Prandtl-Meyer ramp intakes.

4.2.1 Two-shock ramp intake

For a particular free-stream Mach number M_∞ among the five chosen ones and a shock angle, σ, the intake geometry is designed with area ratios close to the self-starting value found in the theoretical study (Section 2.3.1), in accordance with the

methodology described in Chapter 3. By assigning an arbitrary inlet area A_i, the exit area A_e is then determined from the chosen area ratio value ([cd] length in Fig. 4–1a). The intake and flow is planar, and, therefore, "areas" A_i and A_e are considered per unit width and, hence, the dimension of length. Subsequently, how far the cowl is to be moved downstream to have overboard spillage can be determined by specifying the location of the cowl leading edge (point e: $x_{cowl-lip}, y_{cowl-lip}$) using the following relation (under the assumption that the coordinate origin $(0, 0)$ is at the ramp leading edge):

$$\tan\sigma = \frac{A_i}{x_{cowl-lip}} \longrightarrow \begin{cases} x_{cowl-lip} = \frac{A_i}{\tan\sigma} \\ y_{cowl-lip} = A_i \end{cases} . \tag{4.1}$$

Then, the location of the ramp trailing edge (point b: $x_{ramp-trail}, y_{ramp-trail}$) is found as follows:

$$\tan\delta = \frac{A_i - A_e}{x_{ramp-trail}} \longrightarrow \begin{cases} x_{ramp-trail} = \frac{A_i - A_e}{\tan\delta} \\ y_{ramp-trail} = A_i - A_e \end{cases} . \tag{4.2}$$

where the deflection angle δ is calculated by Eq. (2.1).

The [bc] and [de] boundaries are chosen to be long enough so that the cowl (reflected) shock and a few re-reflections, if any, would be within the computational domain and any interference of the exit boundary [cd] with the starting process would be avoided. The cowl is made as thin as possible (the angle between the boundaries [eg] and [ed] is $\sim 0.03°$) so that the leading edge of the cowl would be sharp and its possible influence on the starting process and the starting outcome would be minimized. As the last step, the computational domain is completed by defining the

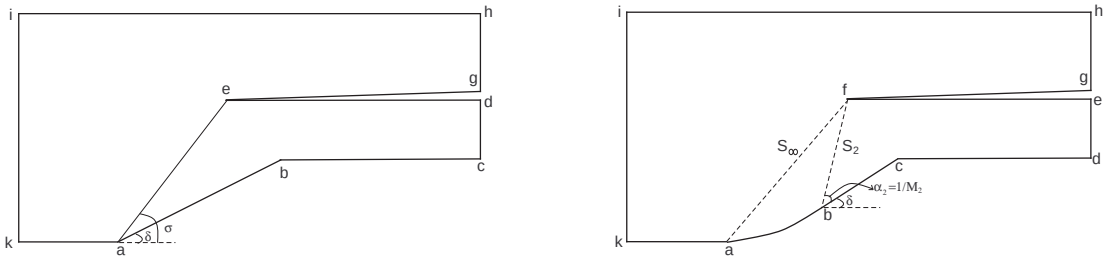

(a) Two-shock ramp intake (b) Prandtl-Meyer intake

Figure 4–1: Ramp intakes geometries.

boundaries [ak], [ki], [ih] and [hg], see Fig. 4–1a. This area surrounding the intake is needed to accommodate the bow shock in front of the internal compression section of the intake.

During the numerical study according to the procedure described in Chapter 3, changing the area ratio is done by increasing or decreasing the exit area, A_e, and, subsequently, changing the length of the ramp surface and the location of the ramp trailing edge.

4.2.2 Prandtl-Meyer intake

The Prandtl-Meyer intake to be considered is defined by specifying one of the chosen free-stream Mach number M_∞, a deflection angle value δ, and and area ratio A_e/A_i close to the minimum self-starting area ratio. By choosing an arbitrary inlet area A_i, the exit area A_e=[de] distance is determined using the area ratio. Using M_∞ and δ, the Mach number downstream of the compression fan M_2 (Eq. (2.6) when $\upsilon(M_2) = \delta - \upsilon(M_\infty)$) and the Mach wave lengths S_∞ and S_2 (Fig. 4–1b and Eq. (2.8)) can be determined.

The coordinate origin $(0,0)$ is placed at the leading edge of the ramp. The location of the cowl leading edge (point f) can be found using the following relations (see Fig. 4–1b):

$$\begin{cases} x_f = x_{cowl-lip} = S_\infty \times \cos\left(\sin^{-1}\left(\frac{y_f}{S_\infty}\right)\right) = \sqrt{S_\infty^2 - A_i^2} \\ y_f = y_{cowl-lip} = A_i \end{cases} . \tag{4.3}$$

The Prandtl-Meyer fan ends at point b (Fig. 4–1b) with the following coordinates:

$$\begin{cases} x_b = x_f - S_2 \times \cos\left(\delta + \sin^{-1}\left(\frac{1}{M_2}\right)\right) \\ y_b = A_i - S_2 \times \sin\left(\delta + \sin^{-1}\left(\frac{1}{M_2}\right)\right) \end{cases} . \tag{4.4}$$

In order to generate points on the Prandtl-Meyer fan surface (the curve from point a to point b), (see Fig. 4–1b), the above explained process (Eq. (4.4)) is repeated N times while the deflection angle is increased N times from 0 to δ with the step $\Delta\delta = \delta/N$ ($N = 50$ is used in the present simulations). Each time, the newly calculated point is connected to the previous one by a straight line to reach the final point b after N steps.

The location of the ramp trailing edge (point c) is determined by:

$$\begin{cases} x_c = x_b + x' & \text{where} \quad x' = \frac{y_c - y_b}{\tan\delta} \\ y_c = A_i - A_e \end{cases} . \tag{4.5}$$

The determination of all other boundaries is carried out in the same way as for the two-shock intake. During numerical experiments, new intake's geometries (new

area ratios) are obtained by changing the exit area of the intake and the coordinates of the point c (the ramp trailing edge).

The computational domain geometries obtained as described in Sections 4.2.1 and 4.2.2 are used as an input to the unstructured grid generator to produce the mesh to be used in the starting simulations.

4.3 Numerical startability results for ramp intakes

In the present section, the maximum contraction ratio of started ramp intakes are found numerically with flow acceleration of $1{,}000g$ and 3 levels of grid refinement as explained in Chapter 3.

4.3.1 Two-shock ramp intake

In [132] Veillard et al. provided only a few numerical results on the startability of two-shock ramp intakes. Much more extensive study is presented in this subsection. At five different free-stream Mach numbers M_∞ of 2.5, 3.0, 3.5, 4.0 and 4.5 and shock angles σ of 22°, 25°, 30°, and 33°, the minimum self-starting area ratios of two-shock ramp intakes are numerically found. The reflected shock in these chosen intakes do not necessarily terminate at the ramp trailing edge, i.e. the general design of two-shock ramp intakes is considered, see Fig. 2–1a. In other words, the presented results are for a set of on-design two-shock ramp intakes on the self-starting (Kantrowitz) surface (Fig. 2–9a), which do not necessarily correspond to the weak-shock, strong-shock, and normal-line designs.

Both theoretical and numerical results are shown in Table 4–1 and Fig. 4–2 in which all numerical data represents the started intakes. For each of the individual cases, the maximum area ratio of the unstarted intake is found to be $0.1\% = 0.001$

less than the related presented value in Table 4–1 and Fig. 4–2. In other words, as explained in Chapter 3, the 2D code used for numerical analysis results in the numerical values with an "error bar" of 0.1% in terms of area ratio, i.e. the difference between the numerical values of the minimum area ratio of the self-started intake, shown in Table 4–1 and Fig. 4–2, with the maximum area ratio of the unstarted intake at each considered case is 0.001)

As shown in Table 4–1 and Fig. 4–2, it is clear that the differences between the theoretical and numerical results are small. For the considered cases, the maximum deviation of the numerical results from the theoretical values is $\sim 1.30\%$ in terms of area ratio.

As seen in Table 4–1, the numerical results deviate slightly from the theoretical values both in positive (the numerical value is higher) and negative (the numerical value is lower) directions. In order to explain these differences, the main theoretical assumptions of having steady and quasi-one-dimensional flow downstream from the bow shock are to be recalled. In numerical analysis, the flow is not completely steady due to a low but non-zero value of acceleration, which reduces the minimum area ratio of the started intake (unsteady effect due to acceleration are favorable for starting).

Furthermore, in the internal compression section, the flow is not one-dimensional. In fact, there is a two-dimensional flow although the turning angle and, subsequently, the vertical velocity are relatively small. This may increase the minimum self-starting area ratio. This phenomenon can be explained by comparing the flow Mach number, M_{2x}, along the free-stream flow direction in the internal compression region in 1D

Table 4–1: Minimum self-starting area ratios of two-shock ramp intakes.

M_∞	$\sigma(^\circ)$	$(\frac{A_e}{A_i})_{Theory}$	$(\frac{A_e}{A_i})_{Numerical}$	Relative difference of the numerical and the theoretical values, %
2.5[1]	25	0.68758	0.687	-0.08
	30	0.58001	0.578	-0.35
	33	0.54113	0.542	+0.16
3.0	22	0.61873	0.617	+0.28
	25	0.53764	0.536	-0.31
	30	0.45821	0.460	+0.39
	33	0.43159	0.431	-0.14
3.5	22	0.48559	0.485	-0.12
	25	0.42639	0.427	+0.14
	30	0.37031	0.368	-0.62
	33	0.35302	0.353	-0.01
4.0	22	0.39726	0.398	+0.19
	25	0.35286	0.353	+0.04
	30	0.31286	0.316	+1.00
	33	0.30139	0.304	+0.87
4.5	22	0.33664	0.336	-0.19
	25	0.30232	0.300	-0.77
	30	0.27332	0.273	-0.12
	33	0.26564	0.269	+1.26

and 2D flow. In one-dimensional flow, M_{2x} is higher than the one in two-dimensional flow. Thus, based on Eq. (1.1), the intake with two-dimensional flow and, subsequently, with lower M_{2x} would need a larger area ratio to get started.

[1] At $M_\infty = 2.5$, if $\sigma = 22^\circ$, the deflection angle is small and the ramp section of the intake is very long, s that this case is not considered.

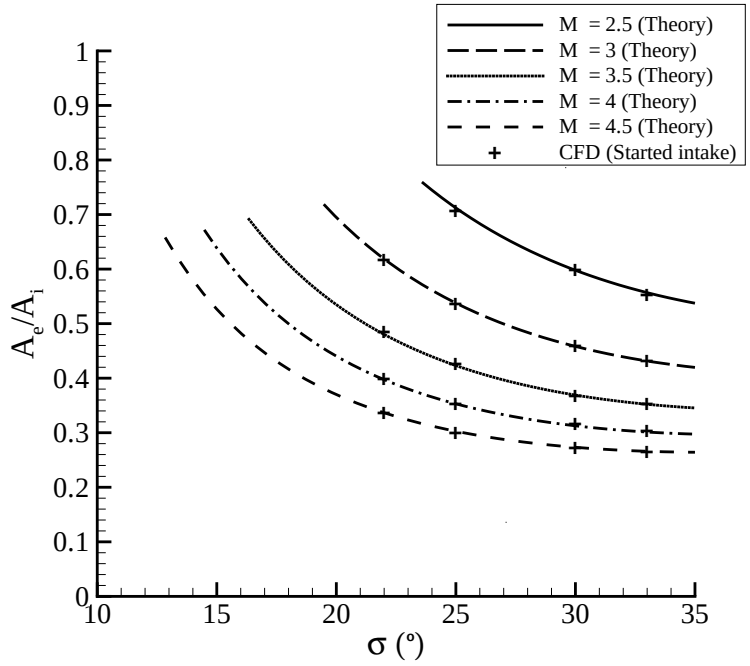

Figure 4–2: Comparison between the minimum self-starting area ratios of two-shock ramp intakes obtained numerically and theoretically. Area ratios A_e/A_i vs. the ramp shock angle σ are shown.

4.3.2 Prandtl-Meyer intake

The numerical simulations for 25 Prandtl-Meyer intakes are done at free-stream Mach numbers of 2.5, 3.0, 3.5, 4.0 and 4.5. At $M_\infty = 3.0$, five Prandtl-Meyer intakes with deflection angles of 7.820°, 10.639°, 12.604°, 16.746°, and 22.039° are simulated. Similarly, at $M_\infty = 2.5$, 3.5, 4.0 and 4.5, the minimum self-starting area ratios of started Prandtl-Meyer intakes with deflection angles of 7.702°, 10.569°, 13.026°, 16.113° and 18.170° (at $M_\infty = 2.5$), 7.599°, 12.582°, 17.575°, 21.072° and 24.910° (at $M_\infty = 3.5$), 7.355°, 12.860°, 18.004°, 23.934° and 27.074° (at $M_\infty = 4.0$)

and, finally, 6.959°, 12.203°, 15.591°, 17.302° and 28.755° (at $M_\infty = 4.5$) are found and shown in Fig. 4–3 and Table 4–2.

All data presented in Fig. 4–3 and Table 4–2 are related to started intakes. For any chosen cases, the difference between the given CFD result of the area ratio of the started intake and the maximum area ratio of the same intake when it is unstarted, is equal to 0.001. For example, at $M_\infty = 2.5$, when minimum area ratio of the started intake with $\delta = 7.702°$ is equal to 0.594, the maximum area ratio of the unstarted intake with same characteristics is equal to 0.593.

From considering Fig. 4–3 and Table 4–2, it is clear that the numerical results are very close to the theoretical ones. The maximum deviation of the numerical and theoretical results is ~ 1.45 in terms of area ratio (see Table 4–2). All these intakes are chosen from the Kantrowitz surface which represents the theoretical minimum self-starting area ratios of Prandtl-Meyer intakes at different M_∞ and δ (Fig. 2–11). The intakes are of general design (Fig. 2–4a), which means that the reflected shock does not necessary terminate at the ramp trailing edge.

As expected from the previous explanation (Section 4.3.1), self-starting intakes' area ratios from numerical simulations are slightly different from the theoretical ones because of the assumptions of having steady and quasi-one-dimensional flow in the Kantrowitz theory.

4.3.3 Numerical results of ramp intakes with weak-shock and strong-shock designs

In Section 2.3.2, the minimum self-starting area ratios for a few specific designs of ramp intakes are calculated, in particular the ramp intakes with weak and strong reflected shocks which terminate at the ramp trailing edge (Figs. 2–1 and 2–4). The

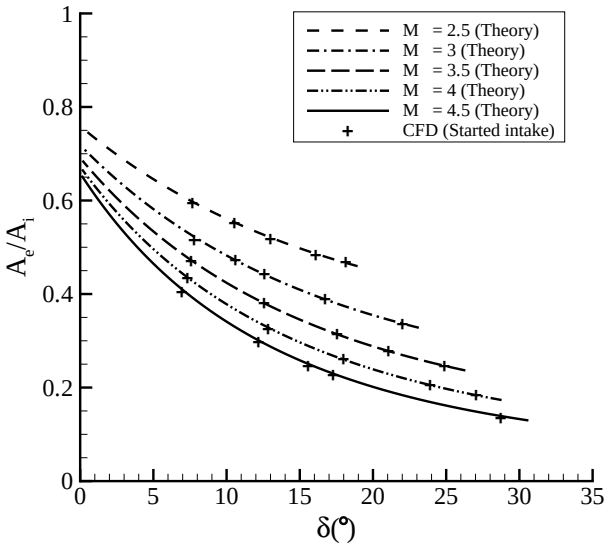

Figure 4–3: Comparison of the numerical and theoretical minimum self-starting area ratios of Prandtl−Meyer intakes. Area ratios A_e/A_i vs. the deflection angle in the compression wave are shown.

theoretical results lead to the conclusion that ramp intakes designed on the basis of strong reflected shock have the self-starting (Kantrowitz) limit which is very close to the theoretical minimum for the given intake family. Therefore, it is important to validate the theoretical results, especially, for the strong-shock-design intakes, with numerical starting trials.

For five two-shock intakes and five Prandtl-Meyer intakes with weak-shock design and for the same number of ramp intakes with strong-shock design, the minimum self-starting area ratios are found via numerical simulation. The results are given in Table 4–3 and shown in Fig. 4–4 in comparison with the theoretical ones. It is clear that again there is a very good agreement for both intake designs, including

Table 4–2: Minimum self-starting area ratios of self-started Prandtl-Meyer ramp intakes.

M_∞	$\delta(^\circ)$	$(\frac{A_e}{A_i})_{Theory}$	$(\frac{A_e}{A_i})_{Numerical}$	Relative difference of the numerical and the theoretical values, %
2.5	7.702	0.59687	0.594	-0.48
	10.569	0.55310	0.552	-0.20
	13.026	0.51989	0.517	-0.56
	16.113	0.48615	0.484	-0.44
	18.170	0.46643	0.468	+0.34
3.0	7.820	0.52193	0.516	-1.14
	10.639	0.47248	0.473	+0.11
	12.604	0.44128	0.442	+0.16
	16.746	0.38902	0.389	-0.01
	22.039	0.33671	0.336	-0.21
3.5	7.599	0.47204	0.471	-0.22
	12.582	0.38106	0.381	-0.02
	17.575	0.31358	0.314	+0.13
	21.072	0.27867	0.279	+0.12
	24.909	0.24642	0.246	-0.17
4.0	7.355	0.43497	0.434	-0.22
	12.861	0.32842	0.326	-0.74
	18.004	0.25918	0.260	+0.32
	23.934	0.20530	0.206	+0.34
	27.074	0.18352	0.184	+0.26
4.5	6.959	0.41011	0.405	+1.25
	12.203	0.30024	0.298	-0.75
	15.591	0.25031	0.248	-0.92
	17.302	0.22891	0.226	-1.27
	28.755	0.13800	0.136	-1.45

the strong-shock design. It is to be noted that as explained in above sections and in Chapter 3, at all presented cases here, for any chosen intake, the difference between

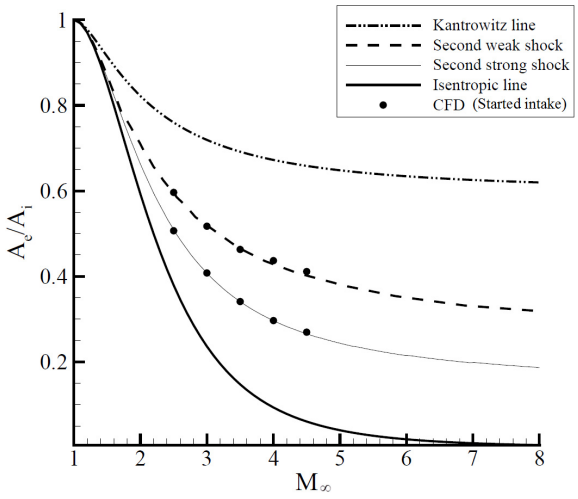

(a) Two-shock ramp intake

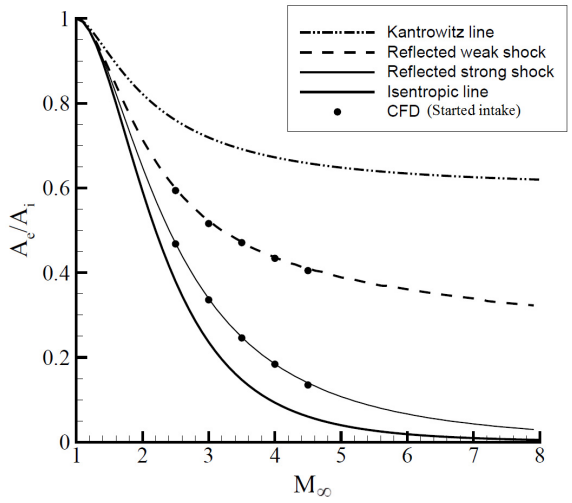

(b) Prandtl-Meyer Intake

Figure 4–4: Comparison between the numerical and theoretical results for the minimum self-starting area ratio of ramp intakes with weak/strong reflected shock which terminates at the ramp trailing edge (weak-shock and strong-shock designs).

the numerical data of the intake's maximum area ratio when it is unstarted and its minimum area ratio when it is started are equal to 0.1%

Table 4–3: Minimum self-starting area ratios of ramp intakes with weak-shock and strong-shock designs.

Ramp intake type	Reflected shock type	M_∞	$(\frac{A_e}{A_i})_{Theory}$	$(\frac{A_e}{A_i})_{Numerical}$	Relative difference of the numerical and the theoretical values, %
Two-shock	Weak	2.5	0.59675	0.596	-0.13
	Weak	3.0	0.51996	0.517	-0.57
	Weak	3.5	0.46523	0.463	-0.48
	Weak	4.0	0.43448	0.437	+0.58
	Weak	4.5	0.40895	0.411	+0.50
	Strong	2.5	0.50908	0.507	-0.41
	Strong	3.0	0.40583	0.408	+0.53
	Strong	3.5	0.34099	0.341	+0.00
	Strong	4.0	0.29587	0.296	+0.04
	Strong	4.5	0.26564	0.269	+1.26
Prandtl-Meyer	Weak	2.5	0.59687	0.594	-0.48
	Weak	3.0	0.52193	0.516	-1.14
	Weak	3.5	0.47204	0.471	-0.22
	Weak	4.0	0.43497	0.434	-0.22
	Weak	4.5	0.41011	0.405	-1.25
	Strong	2.5	0.46643	0.468	+0.34
	Strong	3.0	0.33671	0.336	-0.21
	Strong	3.5	0.24643	0.246	-0.17
	Strong	4.0	0.18352	0.184	+0.26
	Strong	4.5	0.13800	0.136	-1.45

4.4 Flowfield views of started and unstarted ramp intakes

For the purpose of illustration, typical started (area ratio 0.463) and unstarted (area ratio 0.400) flowfields for the two-shock ramp intakes with ramp shock angle of 30° at free-stream Mach number of 3.0 and are shown in Figs. 4–5a and 4–5b. Respectively, Figs. 4–5c and 4–5d show typical started (area ratio 0.391) and unstarted

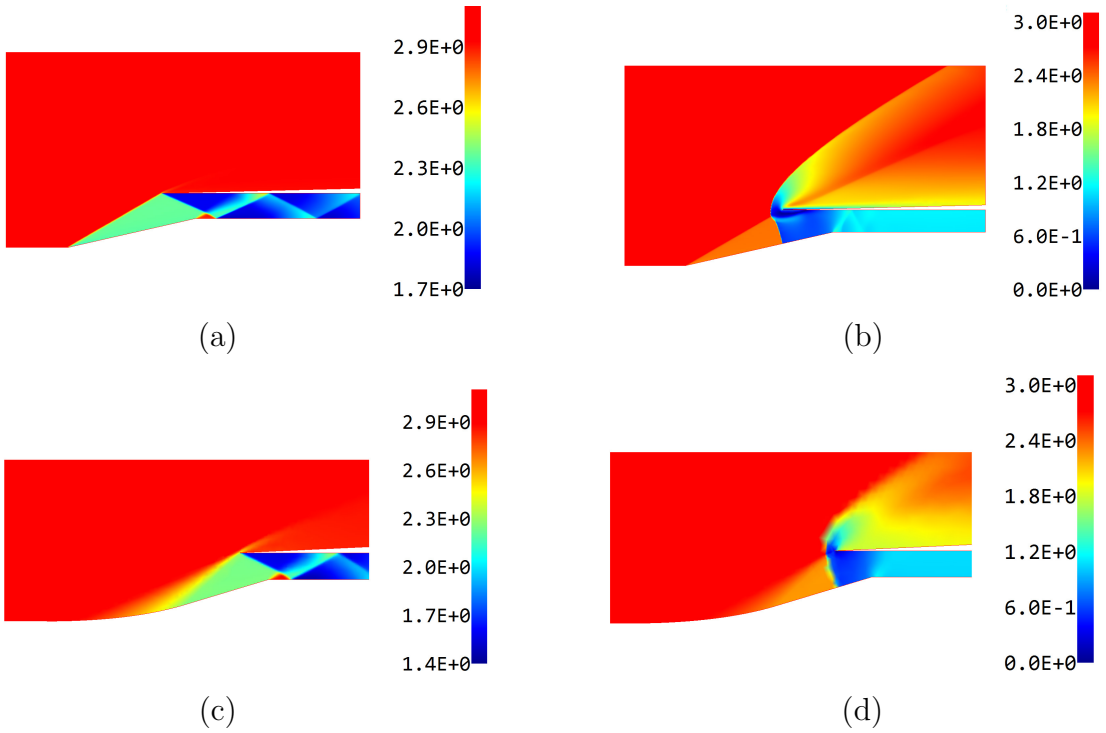

Figure 4–5: Computational flowfield images for ramp intakes at free-stream Mach number of 3: a) started two-shock ramp intake ($\sigma = 30°$, area ratio 0.463), b) unstarted two-shock ramp intake ($\sigma = 30°$, area ratio 0.400), c) started Prandtl-Meyer intake ($\delta = 16.746°$, area ratio 0.391), d) unstarted Prandtl-Meyer intake ($\delta = 16.746°$, area ratio 0.370). Mach number distributions are shown.

(area ratio 0.370) flowfields for the Prandtl-Meyer intakes with the deflection angle of 16.746° at free-stream Mach number of 3.0. In unstarted intakes, the bow shock is clearly present, which provides the mechanism spilling the excessive amount of mass flow. In started intakes, all incoming flow is captured. These intakes are of general designs, so that the reflected shock comes to intake's wall downstream from the ramp trailing edge, thus leading to an oblique shock train in the constant area section of the intakes. For other free-stream Mach numbers, similar results are achieved.

4.5 A note on exit flow non-uniformity

As it is shown in Chapter 2 and the present chapter, the ramp intakes with strong-shock design exhibit the starting characteristics which are close to the theoretical minimum self-starting area ratios for a given intake family. It is to be emphasized that such intakes are *designed* under the assumption that the strong reflected shock terminates at the ramp trailing edge. However, this does not necessarily mean that the intakes will/should *operate* with a strong reflected shock and a subsonic outflow. This is possible only if a specific high back pressure corresponding to the strong-shock reflected pressure is applied. In all other cases, the reflected shock will be a weak one and will not terminate at the ramp trailing edge, thus, resulting in an oblique shock re-reflections and, hence, a non-uniform flow. In other words, better starting characteristics via overboard spillage are achieved for such intakes on the expense of having a non-uniform exit flow.

The degree of non-uniformity of the flow entering the combustor from the intake is an important issue for engine performance. For example, significant intake flow distortion may affect the stability margin of the combustion system [148]. From the other side, some degree of flow non-uniformity is usually induced in the combustor to enhance fuel-air mixing. Therefore, a certain degree of non-uniformity of the intake's exit flow may be tolerated and even exploited for better mixing efficiency. These aspects are, however, out of the scope of present study.

4.6 Conclusion

In the present chapter, the limiting self-starting contractions of ramp intakes with overboard spillage found via theoretical analysis are verified by numerical simulations. The theoretical and numerical results are found to be in a very good agreement. The small differences between them can be explained by considering the underlying assumptions of the Kantrowitz theory (quasi-steady, quasi-one-dimensional flow). In particular, numerical experiments confirm the theoretically established self-starting limits for ramp intakes with strong-shock design, which allow to maximize the overboard spillage effect. These results encourage one to generalize this approach to 3D Busemann intakes based on Busemann flow and using overboard spillage, which may result in high-contraction/compression, efficient intakes with good starting characteristics.

CHAPTER 5
Theory: Busemann Intakes

5.1 Introduction

The existence of Busemann flow and the advantages of using Busemann-flow-based intakes were previously confirmed and discussed in a number of theoretical and experimental studies [81, 138]. Applications to flight vehicles were considered in [83]. The streamline tracing approach allows to introduce overboard spillage for Busemann intakes [64], however, the Kantrowitz (or self-starting) limits on the exit-to-inlet area ratio vs. free-stream Mach number diagram were not determined so far for such Busemann intakes with overboard spillage. In this chapter, the structure of Busemann flow used to design the Busemann intakes is reviewed (Section 5.2). Then, the process of designing a Busemann intake is explained in detail (Section 5.3). Another way to introduce overboard spillage into Busemann intake design is suggested in Section 5.4, which is amenable to the analytical startability analysis. Then, the theoretical approach to account for overboard spillage and predict spontaneous starting characteristics (the Kantrowitz limit) for Busemann intakes with overboard spillage is presented (Section 5.5). Various designs of Busemann intakes are then studied as explained in Sections 5.6 and 5.7 from the point of view of achieving better starting characteristics. Similar to 2D analysis, it is of interest to find out whether the strong-shock-based design principle would hold for Busemann intakes as well.

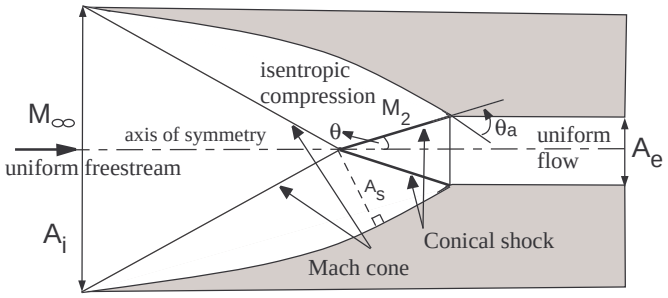

Figure 5–1: Flowfield schematics in an axial cross-section of a fully enclosed, axisymmetrical, Busemann intake.

5.2 Busemann flow and Busemann intake

Busemann flow is an axisymmetric conical internal flow [82], see Fig. 5–1. Its isentropic compression starts at the free-stream Mach angle and decelerates the flow from a high free-stream Mach number to a lower one. Busemann flow is a conical one with the focal point at the axis of symmetry (see Fig. 5–1). The compressed flow passes through a conical shock, resulting in an irrotational and uniform downstream flow parallel to the free-stream flow. In principle, the flow downstream of the conical shock may be subsonic or supersonic depending on whether the conical shock is strong or weak. In the previous studies only Busemann flows with a weak conical shock were considered. In the present thesis, the strong shock option is used as well.

The Busemann intake is designed on the basis of Busemann flow, see Fig. 1–5. The isentropic compression of flow from the Mach cone to the shock cone is schematically shown in Fig. 5–1. The Busemann intake's wall corresponds to the streamline of Busemann flow, which can be obtained by integration of the Taylor-Maccoll and

streamline equations with for example, a fourth order Runge-Kutta method [86]. Details about the Taylor-Maccoll and streamline equations are explained in subsection 5.2.1.

The main advantage of Busemann intakes is their ability to provide high contraction and compression at a very high efficiency (e.g. exceeding 90% [86]) because compression in the intake is predominantly isentropic, with only a small portion of it being achieved via an oblique conical shock. This makes Busemann intakes an attractive choice for practical applications and stimulates the research on the ways to start such intakes because the above mentioned advantages are available only when the intake flow started.

One of the disadvantages of Busemann intakes is related their operation at a certain angle of attack. In that case, the streamlines no longer follow the wall contour of the intake, which might cause flow separation. Furthermore, relatively long compression surfaces especially at higher Mach numbers increase boundary-layer losses [55]. Trimming the intake at the leading edge to the desired truncation angle may solve this problem [85, 149]. However, in this case, an oblique shock is generated at the leading edge, which increases the total pressure losses. Addressing these problematic issues is out of the scope of the present study.

5.2.1 Taylor-Maccoll equations

As mentioned before, by assuming isentropic, conical, axisymmetrical and irrotational flow upstream of a conical shock in Busemann flow, the streamline which would represent the Busemann intake's wall contour, can be obtained by integrating the Taylor-Maccoll equations. The original Taylor-Maccoll equation is a non-linear,

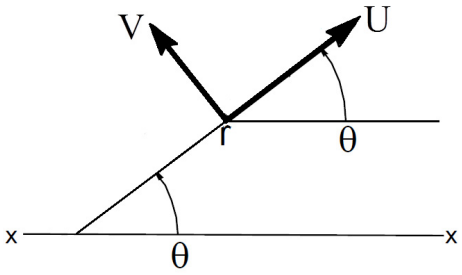

Figure 5–2: The schematics of the polar coordinates used for the analysis of Busemann flow.

second-order, total differential equation in which the polar angle, θ, is the independent variable, and the radial flow velocity, U, is the dependent variable [150, 151]:

$$\frac{\gamma-1}{2}\left[1-U^2-\left(\frac{dU}{d\theta}\right)^2\right]\left[2U+\frac{dU}{d\theta}\cot\theta+\frac{d^2U}{d\theta^2}\right]-\frac{dU}{d\theta}\left[U\frac{dU}{d\theta}+\frac{dU}{d\theta}\frac{d^2U}{d\theta^2}\right]=0. \tag{5.1}$$

In the analysis of Busemann flow, the polar system of coordinate (r, θ) is used, where r is radial coordinate and the angular coordinate is θ measured from the downstream coordinate at the focal point of Busemann flow.

In order to solve this second-order equation, it is transformed to two first-order equations:

$$dV/d\theta = -U + \frac{c^2(U + V\cot\theta)}{V^2 - c^2}, \tag{5.2}$$

$$dU/d\theta = V. \tag{5.3}$$

In the above equations, c is the speed of sound, and V is the angular flow velocity. Equation (5.3) represents the irrotationally condition.

Using radial and angular Mach number components $u = U/c$ and $v = V/c$ as dependent variables instead of the corresponding velocity components U and V, one can get:

$$du/d\theta = v + \frac{\gamma - 1}{2} uv \frac{u + v\cot\theta}{v^2 - 1} = f(u, v, \theta), \tag{5.4}$$

$$dv/d\theta = -u + \left(1 + \frac{\gamma - 1}{2} v^2\right) \frac{u + v\cot\theta}{v^2 - 1} = g(u, v, \theta). \tag{5.5}$$

These equations are coupled and can be integrated, for example, using a fourth order Runge-Kutta method. The flow Mach number is $M = \sqrt{u^2 + v^2}$. The third equation, which should be solved simultaneously to obtain the Busemann intake wall shape, is the streamline equation, $dr/d\theta = ru/v = h(u, v, \theta)$, where $r = r(\theta)$ is the distance between the Busemann flow focal point and the Busemann surface (streamline) along the ray $\theta = const$. The Runge-Kutta method evaluates the differential equations at four different points using the initial values of u_2, v_2 and r_2 (see Appendix A).

5.2.2 Busemann streamline contour curvature

The leading edge of the Busemann intake corresponds to zero flow deflection and zero wall curvature while the component of Mach number normal to the flow axis, $u + v\cot\theta$, is zero. Therefore, as mentioned above, as the leading edge does not have any effect in producing compression, it can be shortened to decrease viscous

losses. The curvature equation can lead us to the same conclusion and also reveal other important properties of the Busemann streamline.

The curvature equation of a planar curve $r = r(\theta)$ in polar coordinates [152] is:

$$D = \frac{r^2 + 2(\frac{dr}{d\theta})^2 - r\frac{d^2r}{d\theta^2}}{(r^2 + (\frac{dr}{d\theta})^2)^{\frac{3}{2}}}. \tag{5.6}$$

This equation can be simplified by substituting $dr/d\theta$ and $d^2r/d\theta^2$ from the streamline equation, $dr/d\theta = ru/v$, and then, $du/d\theta$ and $dv/d\theta$ from the Taylor-Maccoll equations (5.4) and (5.5); thus resulting in:

$$D = \frac{uv(u + v\cot\theta)}{r(v^2 - 1)(v^2 + u^2)^{\frac{3}{2}}}. \tag{5.7}$$

The curvature equation shows that the Busemann streamline can have a zero curvature at two locations. As explained before, one location with zero D is the intake leading edge where $u + v\cot\theta = 0$. The other one is at the point where the radial Mach number u is zero. In other words, every Busemann streamline has an angular location θ at which the flow is normal to r direction or $\theta = const$ line. The line starts at the focal point of Busemann flow and is normal to the Busemann streamline contour. The r value corresponding to that point denoted is r_s and the side area of the cone is denoted A_s. The curvature sign upstream and downstream of the mentioned point with polar angle of θ_s is changed from negative to positive, which shows that the streamline concave towards the axis is changed to a convex one. As will become clear below, the point s is very prominent in startability analysis of Busemann intakes.

Having zero curvature ($D = 0$) because of zero circumferential Mach number v is not possible in Busemann flow, i.e., there is no $v = 0$ point in Busemann flow. In Busemann flow, at no location, the streamlines become normal to the Busemann intake surface as the surface itself is a streamline of the flow.

5.3 Designing process of Busemann intake

As mentioned in the previous sections, the Taylor-Maccoll and streamline equations should be integrated to obtain the Busemann contour surface. The nature of these equations is such that the integration cannot start from the free-stream and proceed downstream due to the fact that there is an infinite number of solutions starting from a given free-stream Mach number and having a uniform exit flow which is parallel to the free-stream. The reason of the existence of an infinite number of solutions is because there is no possibility of specifying the boundary conditions at the free-stream to reach the desired exit flow. Therefore, the integration should be carried out starting from a chosen Mach number M_2 upstream of the conical shock with the aerodynamic shock angle θ_a (see Fig. 5–1) and proceeding in the upstream direction. The free-stream Mach number M_∞ and the intake's area ratio A_e/A_i result from the integration (a trial and error procedure is needed if a particular value of M_∞ is desired).

As mentioned in Section 5.2.1, to start integrating the Taylor-Maccoll equations, the initial values of u_2, v_2 and θ_2 are required, which can be found using two specified parameters, M_2 and θ_a. The angular location of the shock is given by:

$$\theta_2 = \theta_a - \delta_a, \tag{5.8}$$

where δ_a is the flow deflection angle for the conical shock.

The flow deflection δ_a through the conical shock is obtained by substituting Mach number upstream of the conical shock M_2 and the aerodynamic conical shock angle θ_a into the following oblique shock equation [102]:

$$\tan \delta_a = \frac{2 \cot \theta_a (M_2^2 \sin^2 \theta_a - 1)}{2 + M_2^2 (\gamma + 1 - 2 \sin^2 \theta_a)}. \tag{5.9}$$

The initial values of the radial and circumferential Mach numbers, u_2 and v_2, are found using known θ_a and M_2:

$$u_2 = M_2 \cos \theta_a, \tag{5.10}$$

$$v_2 = -M_2 \sin \theta_a. \tag{5.11}$$

The integration of the Taylor-Maccoll equations is continued by decreasing the polar angle from θ_2 to θ_1 in which the vertical Mach number becomes zero, i.e. $u \sin \theta_1 + v \cos \theta_1 = u + v \cot \theta_1 = 0$. To integrate the streamline equation simultaneously with the Taylor-Maccoll ones, the value of $r = r_2 = 1$ at $\theta = \theta_2$ is assigned. The Busemann flow is self-similar so that any arbitrary value of r_2 can be assigned out of convenience, thus here, the streamline originates from $(r, \theta) = (1, \theta_2)$. All such integrations should always terminate with exact theoretical flow deflection of zero and the flow parallel to the free-stream flow, thus making the Busemann streamline-based surface useful for compressing a uniform free-stream. It is to be noted that in the

actual numerical integration, the tolerance of $\delta < 0.001$ is used to stop the integration which lead us to terminate the integrations with flow with very small defection angle close to zero. In other words, in order to find θ_1 limit to stop the integration, a criteria value is chosen for vertical Mach number such as $u + v \cot \theta_1 < 0.001$ in the actual numerical integration.

The integration of the Taylor-Maccoll and streamline equations (more details are in Appendix A) gives in r, u and v as functions of θ, and, consequently, the coordinates (x, y) via $x = r \cos \theta$ and $y = r \sin \theta$, and Mach number $M = \sqrt{u^2 + v^2}$ and deflection angle δ (using Eq.(2.1) where θ is shock angle) at any location on the Busemann contour.

When performing the integration, the point which represents the location with the minimum deflection angle on the Busemann contour, is assumed to correspond to the inlet of the intake with the Mach number $M_\infty = \sqrt{u^2_{\delta_{min}} + v^2_{\delta_{min}}}$ and the inlet area $A_\infty = A_i = \pi y^2_{\delta_{min}}$. The exit flow properties can be found using the values of r_2, θ_2 and M_2, which give the exit area $A_e = \pi y_2^2$ with $y_2 = r_2 \sin \theta_2$.

For subsequent startability analysis of Busemann intakes with overboard spillage (Section 5.5), the flow properties at the point s with zero curvature $r = r(\theta = \theta_s)$ and the respective area $A = A_s$ are to be determined. It should be noted that in actual numerical integration to specified the point s, a criteria or in another word a tolerance is defined to reach the location on the surface which curvature in close to zero (< 0.001). In actual numerical integration with a step $\Delta\theta$, at r_s, the the radial Mach number $u = u_s$ has a minimum value close to zero ($u_s \longrightarrow 0$). Subsequently,

the flow Mach number is $M_{u_{min}} = M_s = \sqrt{u_{min}^2 + v_{u_{min}}^2} = \sqrt{u_s^2 + v_s^2} \simeq \sqrt{v_s^2} = v_s$ and the intake area is equal to $A_s = \pi y_s r_s$ with $y_s = r_s \sin\theta_s$.

As a result of the explained procedure, the Busemann intake with the inlet and exit areas $A_\infty = A_i$ and A_e in the free-stream flow with Mach number M_∞ is designed for the chosen values M_2 and θ_a, and, the parameters of M_s and A_s are also calculated.

5.4 Busemann intakes with overboard spillage

The suitability of Busemann intakes for hyper/supersonic engines with subsonic (ramjet) or supersonic (scramjet) combustion characteristics was studied by Molder [55, 86]. However, the fully enclosed Busemann intake with high contraction (e.g., Fig. 5–1) is difficult to start. One of the ways to overcome this difficulty is to design an intake which would allow overboard spillage in the starting process while retaining the Busemann flowfield in the started mode.

One of the known ways to introduce overboard spillage into Busemann intakes is to design them using the streamline tracing technique and issue the streamlines from off-center (not axisymmetric) contour. This would lead to so-called "sugar-scoop" intake geometries. The leading edge of such intakes is of complex, 3D geometry, and, therefore, the theoretical analysis of the starting characteristics of such 3D intakes is far from straight forward.

In the present thesis, another way to introduce overboard spillage for Busemann intakes is proposed, which is more amenable to analytical assessment of the starting characteristics.

In order to design Busemann intakes with overboard spillage, it is suggested, as the first step, to select a portion of full axisymmetrical Busemann flow characterized by the central angle ϕ ranging from 0° to 360°. The value of ϕ equal to 360° would correspond to the full axisymmetrical Busemann intake, see Fig. 1–5, while angle ϕ tending to 0° would result in a very thin 'slice' of the original axisymmetrical Busemann flow. Figures 5–3a-c show some intermediate cases with $\phi = 90°$, $\phi = 180°$, and $\phi = 270°$, respectively. In all cases, the selected portion of the intake is bounded by two cutting planes intersecting at the axis of symmetry of Busemann flow. The angle between the planes is equal to ϕ (for $\phi \leq 180°$) or $(360° - \phi)$ (for $\phi \geq 180°$). For $\phi < 360°$, the flow capture area of the original full intake is reduced proportionally; therefore, the angle ϕ is therein to be called 'flow capture angle' or simply 'capture angle'.

As the second step, the selected portion is covered by two flat plates, one plate per each above-mentioned cutting plane. The purpose of the plates is twofold: (a) to provide some opening for overboard spillage, or, in other words, to introduce an external compression into the design; (b) to ensure that in case of started flow, the intake flow would remain to be Busemann flow, the same one as in the fully enclosed Busemann intake. These two goals can be achieved simultaneously by considering flat plates with the leading edges forming the Mach angle with the free-stream and extending from the leading edge of the intake to the focal point (the tip of the conical shock) of the Busemann flow. Indeed, as visualized in Figs. 5–3a-c, in such a case, the intake design would feature a V-shaped opening in the external compression part which would provide overboard spillage during the starting process. Furthermore,

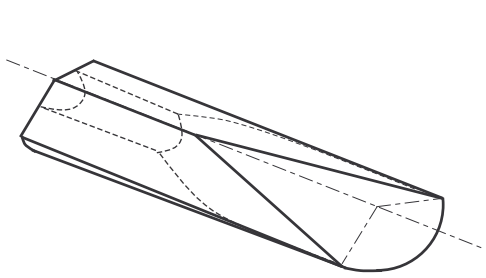

(a) 3D view; capture angle $\phi = 90°$

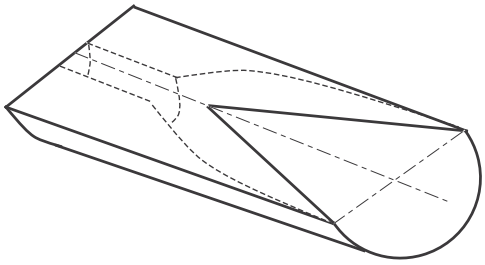

(b) 3D view; capture angle $\phi = 180°$

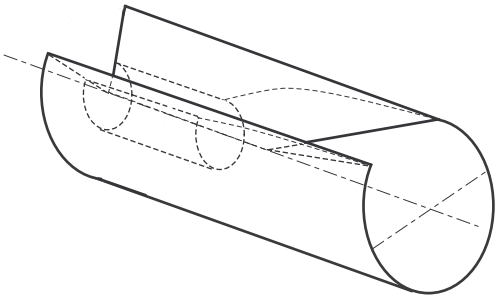

(c) 3D view; capture angle $\phi = 270°$

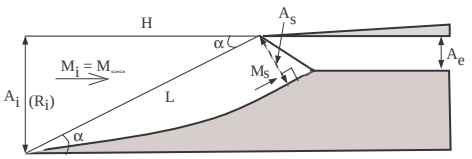

(d) Cross-sectional view

Figure 5–3: Busemann intakes with overboard spillage.

since the leading edges of the flat plates belong to the Mach cone, the started flow, regardless of the value of ϕ, would coincide with the Busemann flow (provided that viscous friction on the plates' surfaces is neglected). Hence, the modified intakes would retain all superior characteristics of the original full Busemann intake (high compression, efficiency) but would presumably possess better self-starting characteristics.

The side view of the flowfields in the intakes with overboard spillage is shown in Fig. 5–3d, which is the same for all angles $\phi < 360°$. However, as it is obvious from Figs. 5–3a-c, the amount of spillage increases with decrease of the capture angle

ϕ. Therefore, it would be logical to expect better self-starting characteristics when $\phi \to 0$. The respective analysis will be found in the next section.

5.4.1 Spillage calculation for Busemann intakes with different capture angles

Busemann intakes can have different capture angles ϕ, from 0° to 360°. Decreasing the capture angle of the Busemann intake increases the magnitude of spillage amount. For subsequent determination of the self-starting (Kantrowitz) area ratios of Busemann intakes with overboard spillage, it is necessary to evaluate the magnitude of mass spillage for various capture angles. In general, the amount of the mass spillage depends on the intake's geometrical characteristics, such as the spillage area, and flow parameters downstream from the bow shock of the unstarted flow configuration. The starting flow in Busemann intakes shown in Fig. 5–3 is three-dimensional and complex. Therefore, in this study, the spillage amount is obtained from purely geometrical considerations on the basis of the magnitude of spillage area A_{spill} alone. Three different ways or theories are suggested to evaluated A_{spill} for Busemann intakes with different capture angles. Furthermore, the maximum spillage area $A_{max-spill}$ for small capture angle ($\phi \to 0$) is evaluated too within each theory.

Theory I)

The Busemann intakes are divided into two main categories based on their capture angles:

I) $0° < \phi \leq 180°$: Busemann intakes with capture angles greater than zero and less than or equal to 180° (half-Busemann intake);

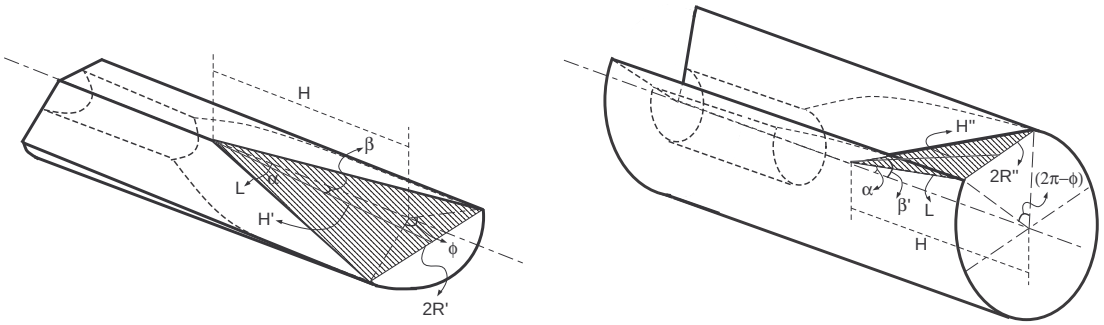

(a) $0° < \phi \leq 180°$ (b) $180° \leq \phi < 360°$

Figure 5–4: Schematic representation of the spillage area in Busemann intakes (Theory I).

II) $180° \leq \phi < 360°$: Busemann intakes with capture angles equal to or greater than 180° and less than 360° (full intake).

In this theory, as shown in Figs. 5–4a and 5–4b, for both categories the opening area in the external compression section is covered by an imaginary planar surface, which area represents the spillage area A_{spill}.

For Busemann intake in category (I), may be easily deduced from Fig. 5–4a, the spillage area is equal to:

$$\left.\begin{array}{l} A_{spill-(\phi\leq 180°)} = R'H' \\ R' = R_i \sin\left(\frac{\phi}{2}\right) \\ H' = \frac{H}{\cos\beta} \\ H = \frac{R_i}{\tan\alpha} \end{array}\right\} \Rightarrow A_{spill-(\phi\leq 180°)} = \frac{HR_i \sin\left(\frac{\phi}{2}\right)}{\cos\phi} = \frac{R_i^2 \sin\left(\frac{\phi}{2}\right)}{\tan\alpha\cos\beta}, \quad (5.12)$$

where

$$\left.\begin{array}{l} H' = \frac{H}{\cos\beta} \\ H'\sin\beta = R_i\cos\left(\frac{\phi}{2}\right) \\ H = \frac{R_i}{\tan\alpha} \end{array}\right\} \Rightarrow \tan\beta = \frac{R_i}{H}\cos\left(\frac{\phi}{2}\right) = \tan\alpha\cos\left(\frac{\phi}{2}\right).$$

where R_i is the radius of the inlet cross-section, and α is the Mach angle of the free-stream flow, and other notations are shown in Figs. 5–4a and 5–3d.

For Busemann intake in category (II), as shown in Fig. 5–4b, the spillage area is equal to:

$$\left.\begin{array}{l} A_{spill-(\phi\geq 180^\circ)} = R''H'' \\ R'' = R_i\sin\left(\frac{\phi}{2}\right) \\ H'' = \frac{H}{\cos\beta'} \\ H = \frac{R_i}{\tan\alpha} \end{array}\right\} \Rightarrow A_{spill-(\phi\geq 180^\circ)} = \frac{HR_i\sin\left(\frac{\phi}{2}\right)}{\cos\beta'} = \frac{R_i^2\sin\left(\frac{\phi}{2}\right)}{\tan\alpha\cos\beta'}, \quad (5.13)$$

where

$$\left.\begin{array}{l} H'' = \frac{H}{\cos\beta'} \\ H''\sin\beta' = R_i\cos\left(\frac{2\pi-\phi}{2}\right) = -R_i\cos\left(\frac{\phi}{2}\right) \\ H = \frac{R_i}{\tan\alpha} \end{array}\right\} \Rightarrow \left\{\begin{array}{l} \tan\beta' = \frac{-R_i}{H}\cos\left(\frac{\phi}{2}\right) \\ \qquad\quad = -\tan\alpha\cos\left(\frac{\phi}{2}\right) \end{array}\right. .$$

It is to be noted that even though in this theory the spillage area is obtained from geometrical considerations, some implicit influence of free-stream Mach number is present because the angles α, β and β' depend on it.

The maximum spillage amount for a thin ($\phi \longrightarrow 0$) Busemann intake $A_{max-spill}$ is represented by the length of L, see the side view in Fig. 5–3d and Fig. 5–4.

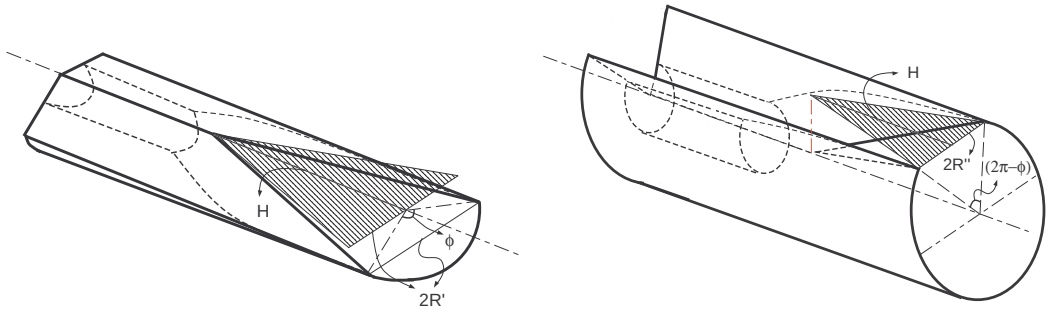

(a) $0° < \phi \leq 180°$ (b) $180° \leq \phi < 360°$

Figure 5–5: Schematic representation of the spillage area in Busemann intakes (Theory II).

Theory II)

The main difference between this theory (Theory II) and the first one (Theory I) is related to the assumption of that only spillage in upward direction is essential. In other words, the projections of the shaded areas in Fig. 5–4 to the horizontal plane are considered, as illustrated in Fig. 5–5. In this case, when $\phi \to 0$, the maximum spillage area $A_{max-spill}$ can be represented by the length H (Figs. 5–3d and 5–5). The new spillage areas for Busemann intakes with different capture angles can be then found as (see Fig. 5–5 for details):

$$\left.\begin{array}{l} A_{spill-(\phi\leq 180°)} = R'H \\ A_{spill-(\phi\geq 180°)} = R''H \\ R' = R'' = R_i \sin\left(\frac{\phi}{2}\right) \\ H = \frac{R_i}{\tan\alpha} \end{array}\right\} \Rightarrow \left\{\begin{array}{r} A_{spill-(\phi\leq 180°)} = A_{spill-(\phi\geq 180°)} \\ = HR_i \sin\left(\frac{\phi}{2}\right) = \frac{R_i^2 \sin\left(\frac{\phi}{2}\right)}{\tan\alpha} \end{array}\right. , \tag{5.14}$$

It is obvious from Eqs. (5.12), (5.13) and (5.14) that the spillage area A_{spill} predicted by Theory I and Theory II tends to zero when the capture angle $\phi \to 0$.

This is consistent with the fact that the inlet area $A_{(i-\phi)} = (R_i^2/2)\phi$ tend to zero as well when $\phi \to 0$. What is important for starting is the relative magnitude of the spillage area in comparison with the inlet area. Therefore, the spillage area A_{spill} is to be normalized by the inlet area A_i. In this case, one would have the dependency on ϕ as $\frac{\sin\phi}{\phi}$ which tends to unity when $\phi \to 0$. Therefore, the ratio A_{spill}/A_i has an finite limit when $\phi \to 0$. The maximum spillage area $A_{max-spill}$ should be also normalized by the inlet area $A_{(i-0)}$ for every thin intake, which can be presented by the length R_i. This approach is taken in Section 5.5 when accessing the starting characteristics of the intakes.

Theory III)

This theory is inspired by numerical starting experiments to be presented in Chapter 6. These experiments reveal that for capture angles greater than 180°, the amount of overboard spillage is just slightly more than the one predicted by Theory I and Theory II. Therefore, for $180° < \phi < 360°$, Theory III coincides with Theory II:

$$A_{spill-(\phi \geq 180°)} = HR_i \sin\left(\frac{\phi}{2}\right). \tag{5.15}$$

This area represents the projection of the shaded areas in Fig. 5–6b on horizonal plane. When the capture angle changes from 360° till 180°, the spillage area increases from zero to HR_i, which corresponds to area of V-shaped opening when $\phi = 180°$.

For the capture angles lower than 180°, the assumptions is made that the spillage area consist of two terms: HR_i, which is independent from the capture angle, and an additional contribution, corresponding to side ways spillage, which was closed for

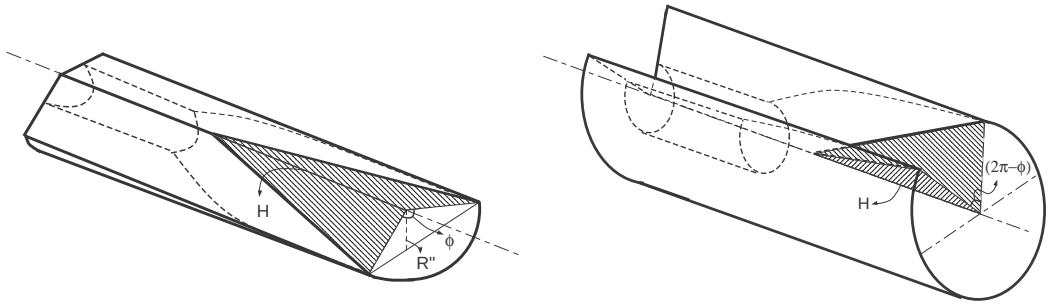

(a) $0° < \phi \leq 180°$ (b) $180° \leq \phi < 360°$

Figure 5–6: Schematic representation of the spillage area in Busemann intakes (Theory III).

$\phi > 180°$. The second terms corresponds to the projection of the the shaded areas in Fig. 5–6a to a vertical plane $(\frac{1}{2})HR_i \cos(\phi/2)$. Thus, for $0 < \phi < 180°$, the spillage area is expected as:

$$A_{spill-(\phi \leq 180°)} = HR_i \left(1 + \frac{\cos\left(\frac{\phi}{2}\right)}{2} \right). \tag{5.16}$$

It changes from HR_i for $\phi = 180°$ to $(3/2)HR_i$ for $\phi = 0°$, i.e. the maximum spillage $A_{spill-max} = (3/2)HR_i$. It is obvious that in contrast to Theory I and Theory II, the normalization of spillage area is not required in this case.

5.5 Starting of Busemann intakes via overboard spillage

The startability of fully enclosed (internal compression only) Busemann intakes can be determined using the classical Kantrowitz approach (Chapter 1). A normal shock is placed at the entry cross-section of the intake, producing subsonic flow which accelerates isentropically towards the intake's exit. The exit-to-entry area ratio resulting in flow choking at the exit ($M_e = 1$) corresponds to the self-starting limit for the given free-stream Mach number (Chapter 1). For the area ratios equal

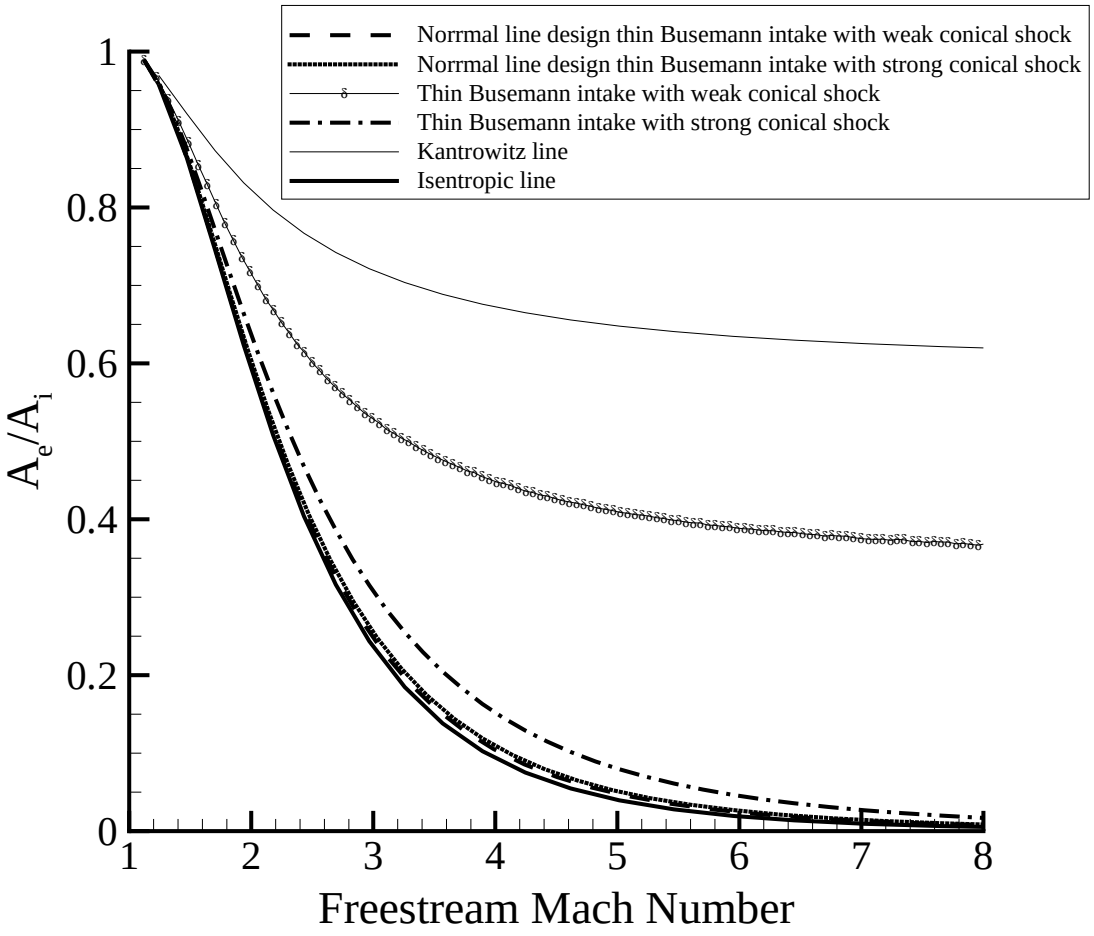

Figure 5–7: Self-starting (Kantrowitz) limits for Busemann intakes.

or exceeding this limiting value, the intake would start spontaneously. By calculating the limiting area ratios of started intakes for various free-stream Mach numbers, one can obtain the Kantrowitz (or self-starting) line shown as a thin solid line on the area ratio/free-stream Mach number diagram (the Kantrowitz diagram) in Fig. 5–7.

For intakes with mixed (external and internal) compression, i.e., with overboard spillage, the same basic principle is used similar to what is explained in Chapter 2. A conical normal shock wave is placed between the focal point of Busemann flow (so that this would no spillage through the V-shaped opening) and the Busemann surface at the cross-section denoted as A_s, where the local Mach number is M_s, i.e., the normal conical shock is being placed at the entry of the enclosed section of the intake.

It is to be noted that according the analysis in Section 5.3, the line $\theta = const$ drawn from the focal point perpendicularly to the Busemann surface would come to the surface at the point of its zero curvature, where the flow is normal to the $\theta = const$ line. Therefore, it is indeed possible to place a conical normal shock at that location.

It is also to be noted that for all Busemann intake designs to be introduced below the Busemann surface should, at the very least, extend from the leading edge to the point s of zero curvature. Otherwise, the normal conical shock placed at $\theta = \theta_s$ would have a non-uniform flow upstream of it and, hence, would be of variable strength, thus complicating the subsequent startability analysis based on the Kantrowitz theory. This requirement is analogous to the one for ramp intakes to have the line issued from the cowl leading edge perpendicularly to the ramp surface, coming to the surface upstream from the ramp trailing edge.

The flow downstream from the shock is assumed to be isentropic. Based on the Kantrowitz theory, if the contraction downstream of the conical normal shock does not lead to choking, then the shock would move downstream and the intake would

start spontaneously. In other words, the exit-to-entry area ratio of the enclosed section of the intake A_e/A_s and the Mach number of M_s, must satisfy the Kantrowitz theory condition for fully enclosed ducts, i.e., the point (M_s,A_e/A_s) must belong to the Kantrowitz line for fully enclosed ducts. In this case, the area ratio A_e/A_s is named $(A_e/A_s)_{Kantrowitz}$.

The Busemann intake designs considered in the present study are illustrated in Fig. 5–8. Figure 5–8a shows the traditional design with a weak conical shock. Other three designs are newly produced in this thesis. The integration of the Busemann contour may begin from a strong conical shock, thus resulting in the strong shock design (Fig. 5–8b). Both Busemann contours (based on weak and strong shock) may be terminated at the point of zero curvature, where $\theta = const$ line (r_s) is perpendicular to the contour. Then, two other designs are obtained: normal cut design based on weak conical shock and normal cut design based on strong conical shock (Fig. 5–8c and Fig. 5–8d). It is to emphasized again that in all designs on the basis of strong shock, it is considered for design purposes only. The started flow will be with a weak shock unless special boundary conditions are imposed at the exit. The side view of thin Busemann intakes with all explained designs are also shown in Fig. 5–9.

As explained in Section 5.3, for any combination (M_2, θ_a), the Taylor-Maccoll and streamline equations are integrated to obtain the Busemann contour and subsequently, M_∞, M_s, M_e, A_s, A_e and A_i are calculated. It is necessary to specify one of the intake designs mentioned above to continue the process of the startability analysis.

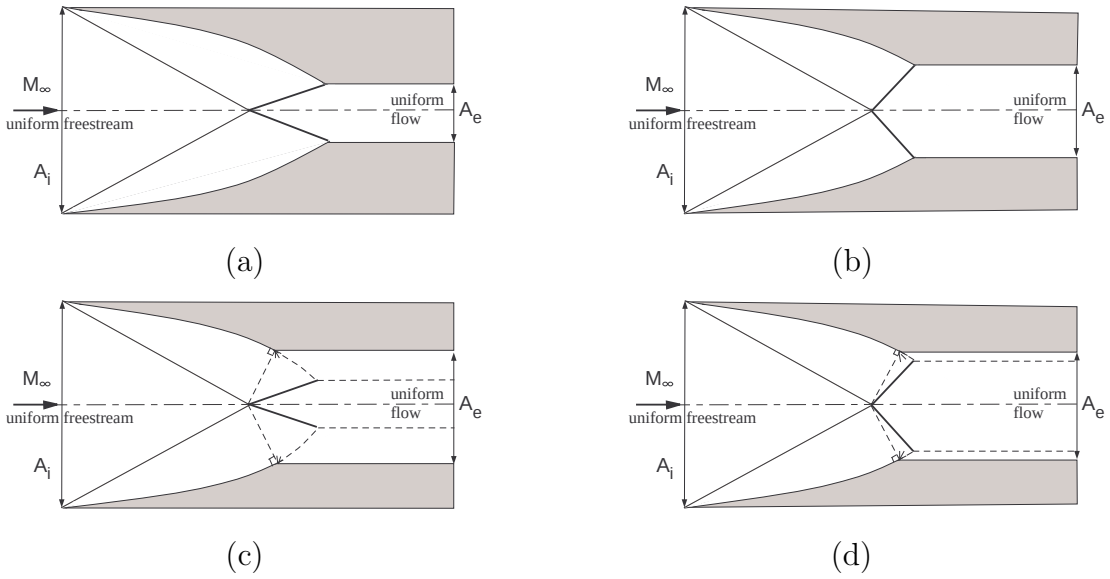

Figure 5–8: Busemann intake designs: (a) with weak conical shock; (b) with strong conical shock; (c) normal cut design based on weak conical shock; (d) normal cut design based on strong conical shock.

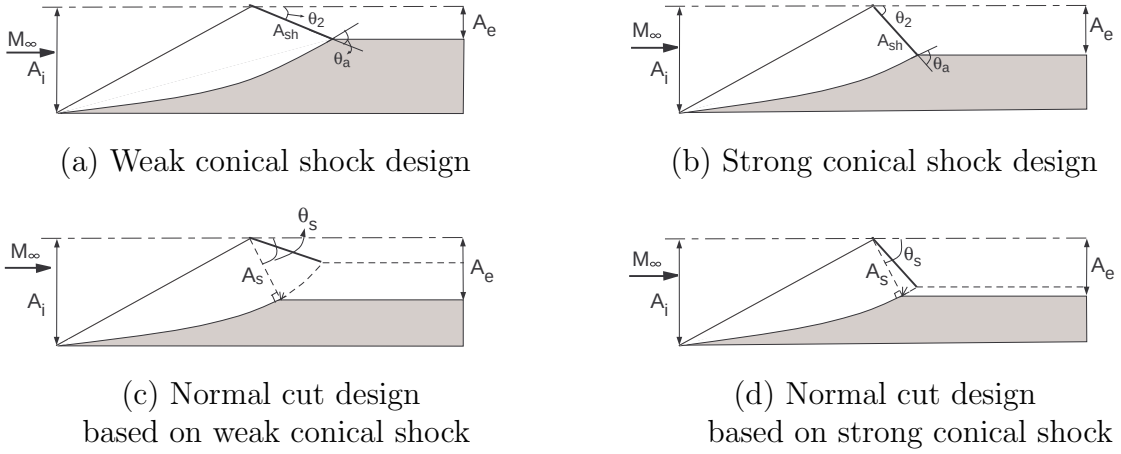

(a) Weak conical shock design

(b) Strong conical shock design

(c) Normal cut design based on weak conical shock

(d) Normal cut design based on strong conical shock

Figure 5–9: Thin Busemann intake designs side views.

Each intake design has an additional constraint related to the exit area. For the normal-cut-design intakes, the exit area A_e is equal to $A_s \sin\theta_s$, see Figs. 5–9c

and 5–9d. For Busemann intakes with weak or strong conical shock which terminates at the trailing edge of the Busemann surface, shown in Figs. 5–9a and 5–9b, one has $A_e = A_{sh} \sin\theta_2 = A_{sh} \sin(\theta_a - \delta_a)$ where the shock area A_{sh} is equal to $(\pi r_2^2 \sin\theta_2$. To find out the type of the shock, the maximum conical shock angle $(\theta_a)_{max}$ is calculated by Eq. (2.4) with $M = M_2$. Then, if the shock angle θ_a is less than the maximum one $(\theta_a)_{max}$, the shock is weak and if $\theta_a > \theta_{max}$, there is strong conical shock.

The next step in startability analysis of Busemann intakes is to compare the area ratio A_e/A_s of the intake calculated via the explained procedure with the Kantrowitz area ratio $(A_e/A_s)_{Kantrowitz}$ for Mach number M_s. Alternatively, the intake area ratio A_e/A_i can be compared with Kantrowitz value for $M = M_\infty$ If the intake area ratio satisfies the self-starting condition, $(A_e/A_i)_{Kantrowitz} \leq (A_e/A_i)$, the intake with chosen M_2 and θ_a starts spontaneously.

This process is repeated at different values of aerodynamic conical shock angle θ_a to find the smallest self-starting area ratio at M_2. Covering all the parametric space (M_2, θ_a), one can determine the Kantrowitz (self-starting) limit for the Busemann intakes with overboard spillage and different designs on the $(M_\infty, A_e/A_i)$ diagram, see Fig. 5–7.

However, it should be immediately pointed out that the above analysis is applicable only to Busemann intakes with small capture angles, when the overboard spillage is maximized. Strictly speaking, it is valid only in the limit $\phi \to 0$. With increase of ϕ, the spillage sideways and eventually upwards is gradually restricted by the Busemann surface walls and it is completely eliminated at $\phi = 360°$. To take into

account the change in overboard spillage at various capture angles, it is suggested to modify the area ratio for the internal compression section A_e/A_s as follows:

$$\frac{A_e}{\widetilde{A_s}} = \frac{A_e}{A_s - f(\phi)(A_s - A_i)}. \tag{5.17}$$

where $0 \leq f(\phi) \leq 1$ is a function of the capture angle satisfying the following conditions: $f(0) = 0$ and $f(2\pi) = 1$. These conditions ensure that for the fully enclosed case ($\phi = 2\pi = 360°$), the overall exit-to-entry ratio A_e/A_i is recovered while for the other limiting case, $\phi = 0$, the non-modified area ratio A_e/A_s is used.

In other words, the modified area ratio of the enclosed section of Busemann intakes with different capture angles ϕ is defined as the following weighted average of A_s and A_i:

$$\widetilde{A_s} = A_s + f(\phi)(A_i - A_s) = f(\phi)A_i + (1 - f(\phi))A_s. \tag{5.18}$$

where A_i is the inlet area of a Busemann intake and A_s is the inlet area of the enclosed section of the intake.

It would be logical to relate the weight function $f(\phi)$ to the magnitude of the spillage area, see Section 5.4. The function $f(\phi)$ should be equal to 1 in the absence of spillage and it will be equal to zero when spillage is maximized ($\widetilde{A_s} = A_s$).

The function of $f(\phi)$ is defined as:

$$f(\phi) = 1 - \frac{\lambda}{\mu}, \tag{5.19}$$

where $\lambda = A_{spill}/A_{(i-\phi)}$ and $\mu = A_{max-spill}/A_{(i-0)}$ in Theory I and/or Theory II are used to define the spillage area or $\lambda = A_{spill}$ and $\mu = A_{max-spill}$ in the case of using Theory III (see Section 5.4).

Thus, for any Busemann intake with capture angle of ϕ, the function $f(\phi)$ is defined as the difference between 1 and the ratio of the spillage area to the maximum spillage area. The spillage areas should be normalized by the inlet (capture) area when Theory I or II are used, see Section 5.4.

It is clear that for a full Busemann intake with $\phi = 360^\circ$ and no spillage, λ is equal to zero, $A_{spill}/A_{(i-360)} = 0$, $f(\phi = 360^\circ) = 1$ and, therefore, $\widetilde{A}_s = A_i$. On the other hand, when $\phi \longrightarrow 0^\circ$ for thin Busemann intake, $A_{spill}/A_{(i-\phi)}$ is equal to $A_{max-spill}/A_{(i-0)}$, which gives $f(0^\circ) = 0$ and $\widetilde{A}_s = A_s$.

The spillage area A_{spill} is given by Eqs. (5.12), (5.13) or (5.14). Then, using the capture area $A_{(i-\phi)}$ equal to $(\phi/2)R_i^2$, the value of λ is determined as follows:

$$\lambda_{\phi\leq 180^\circ} = \frac{A_{spill-(\phi\leq 180^\circ)}}{A_{(i-\phi)}} = \begin{cases} \lambda_{(Th.(I)-\phi\leq 180^\circ)} = \dfrac{\frac{R_i^2 \sin\left(\frac{\phi}{2}\right)}{\tan\alpha\cos\beta}}{\frac{\phi}{2}R_i^2} = \dfrac{\sin\left(\frac{\phi}{2}\right)}{\left(\frac{\phi}{2}\right)\tan\alpha\cos\beta} \\ \lambda_{(Th.(II)-\phi\leq 180^\circ)} = \dfrac{\frac{R_i^2 \sin\left(\frac{\phi}{2}\right)}{\tan\alpha}}{\frac{\phi}{2}R_i^2} = \dfrac{\sin\left(\frac{\phi}{2}\right)}{\left(\frac{\phi}{2}\right)\tan\alpha} \end{cases} . \tag{5.20}$$

$$\lambda_{\phi\geq 180^\circ} = \frac{A_{spill-(\phi\geq 180^\circ)}}{A_{(i-\phi)}} = \begin{cases} \lambda_{(Th.(I)-\phi\geq 180^\circ)} = \dfrac{\frac{R_i^2 \sin\left(\frac{\phi}{2}\right)}{\tan\alpha\cos\beta'}}{\frac{\phi}{2}R_i^2} = \dfrac{\sin\left(\frac{\phi}{2}\right)}{\left(\frac{\phi}{2}\right)\tan\alpha\cos\beta'} \\ \lambda_{(Th.(II)-\phi\geq 180^\circ)} = \dfrac{\frac{R_i^2 \sin\left(\frac{\phi}{2}\right)}{\tan\alpha}}{\frac{\phi}{2}R_i^2} = \dfrac{\sin\left(\frac{\phi}{2}\right)}{\left(\frac{\phi}{2}\right)\tan\alpha} \end{cases} . \tag{5.21}$$

For a thin Busemann intake, $A_{(i-0)}$ is equal to R_i. Thus, μ can be found as:

$$\mu=\frac{A_{max-spill}}{A_{(i-0)}}=\begin{cases}\mu_{Th.(I)}=\frac{L}{R_i}=\frac{\frac{R_i}{\sin\alpha}}{R_i}=\frac{1}{\sin\alpha}=M_\infty\\ \mu_{Th.(II)}=\frac{H}{R_i}=\frac{\frac{R_i}{\tan\alpha}}{R_i}=\frac{1}{\tan\alpha}\end{cases}. \tag{5.22}$$

It is good to remind that in the case of applying Theory III is theoretical analysis:

$$\begin{cases}\lambda_{\phi\geq 180^\circ}\overset{Th.(III)}{=}A_{spill-(\phi\geq 180^\circ)}=HR\times\sin\left(\frac{\phi}{2}\right)\\ \lambda_{\phi\leq 180^\circ}\overset{Th.(III)}{=}A_{spill-(\phi\leq 180^\circ)}=HR\times\left(1+\frac{\cos\frac{\phi}{2}}{2}\right)\\ \mu\overset{Th.(III)}{=}A_{max-spill}=\frac{3}{2}RH\end{cases}. \tag{5.23}$$

Finally, when any one of the above mentioned three theories is used, $f(\phi)$ can be determined for any chosen ϕ as:

$$f(\phi)_{(0^\circ<\phi\leq 180^\circ)}=\begin{cases}=1-\frac{\frac{A_{spill-(\phi\leq 180^\circ)}}{A_{(i-\phi)}}}{\frac{A_{max-spill}}{A_{(i-0)}}}=\begin{cases}\overset{Th.(I)}{=}1-\frac{\frac{\sin\left(\frac{\phi}{2}\right)}{\left(\frac{\phi}{2}\right)\tan\alpha\cos\beta}}{\frac{1}{\sin\alpha}}=1-\frac{\cos\alpha\sin\left(\frac{\phi}{2}\right)}{\left(\frac{\phi}{2}\right)\cos\beta}\\ \overset{Th.(II)}{=}1-\frac{\frac{\sin\left(\frac{\phi}{2}\right)}{\left(\frac{\phi}{2}\right)\tan\alpha}}{\frac{1}{\tan\alpha}}=1-\frac{\sin\left(\frac{\phi}{2}\right)}{\frac{\phi}{2}}\end{cases}\\ \overset{Th.(III)}{=}1-\frac{A_{spill-(\phi\leq 180^\circ)}}{A_{max-spill}}=1-\frac{RH\left(1+\frac{\cos\left(\frac{\phi}{2}\right)}{2}\right)}{\frac{3}{2}RH}=1-\left(\frac{2+\cos\left(\frac{\phi}{2}\right)}{3}\right)\end{cases} \tag{5.24}$$

$$f(\phi)_{(180^\circ\leq\phi\leq 360^\circ)}=\begin{cases}=1-\frac{\frac{A_{spill-(\phi\geq 180^\circ)}}{A_{(i-\phi)}}}{\frac{A_{max-spill}}{A_{(i-0)}}}=\begin{cases}\overset{Th.(I)}{=}1-\frac{\frac{\sin\left(\frac{\phi}{2}\right)}{\left(\frac{\phi}{2}\right)\tan\alpha\cos\beta'}}{\frac{1}{\sin\alpha}}=1-\frac{\cos\alpha\sin\left(\frac{\phi}{2}\right)}{\left(\frac{\phi}{2}\right)\cos\beta'}\\ \overset{Th.(II)}{=}1-\frac{\frac{\sin\left(\frac{\phi}{2}\right)}{\left(\frac{\phi}{2}\right)\tan\alpha}}{\frac{1}{\tan\alpha}}=1-\frac{\sin\left(\frac{\phi}{2}\right)}{\frac{\phi}{2}}\end{cases}\\ \overset{Th.(III)}{=}1-\frac{A_{spill-(\phi\geq 180^\circ)}}{A_{max-spill}}=1-\frac{RH\sin\left(\frac{\phi}{2}\right)}{\frac{3}{2}RH}=1-\frac{2}{3}\sin\left(\frac{\phi}{2}\right)\end{cases} \tag{5.25}$$

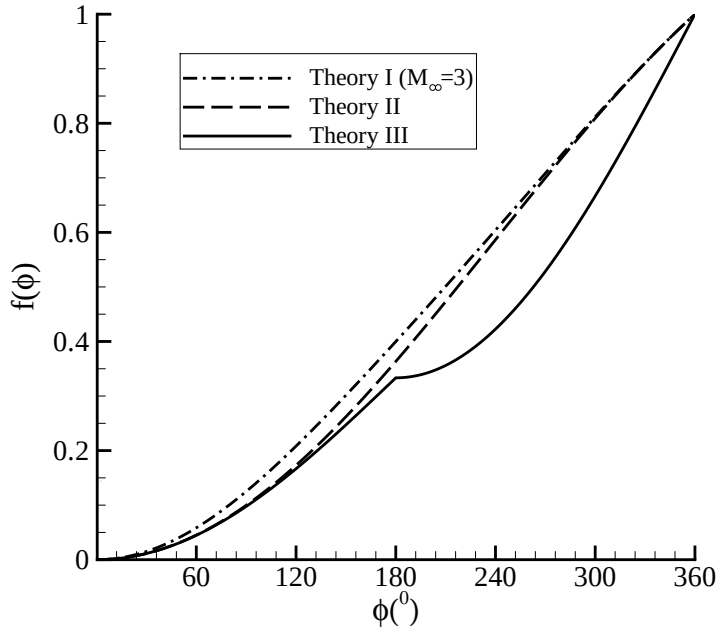

Figure 5–10: Variation of $f(\phi)$ vs. ϕ.

Figure 5–10 shows $f(\phi)$ values calculated using all 3 theories when ϕ is increasing from 0° to 360°. It is clear that as explained above (Section 5.4), the geometrical analysis used to find spillage area A_{spill} in Theory I and Theory II results in gradually increasing of $f(\phi)$ by increasing capture angle ϕ. However, as expected using Theory III defined based on the numerical achievements results in a sharp corner on $f(\phi)-\phi$ diagram at $\phi = 180°$.

Knowing the modified area ratio at any ϕ, the startability analysis for the cases with $0 < \phi < 360°$ starts by choosing a pair (M_2, θ_a). Then, the ratio A_e/A_s, which is obtained for any specific design and $\phi \simeq 0$, is modified to $A_e/\widetilde{A_s}$ using Eqs. (5.17), (5.24) and (5.25). Having M_2 and the modified internal contraction area ratio $A_e/\widetilde{A_s}$,

one obtains the corresponding new free-stream Mach number $\widetilde{M_\infty}$ and shock angle $\widetilde{\theta}$/aerodynamic shock angle $\widetilde{\theta_a}$ (among all available data at M_2 and different θ_a for thin Busemann intakes) as well as the new Busemann contour and the Mach number $\widetilde{M_s}$ at the cross-section $\widetilde{A_s}$ with $u_s \simeq 0$. As the final step, it is analyzed whether or not $\widetilde{M_s}$ and $A_e/\widetilde{A_s}$ satisfy the Kantrowitz criterion. It is very important to note that the above algorithm allows for seamless transition from the case of $\phi \simeq 0$ to $\phi = 360^\circ$ in terms of $\widetilde{M_s}$ and $A_e/\widetilde{A_s}$ (the respective proper values of both quantities are recovered in both limiting cases).

Similar to the case $\phi = 0^\circ$, covering all the parametric space (M_2, θ_a), one can determine the Kantrowitz (self-starting) limit for the Busemann intake with the given capture angle ϕ on the $(M_\infty, A_e/A_i)$ diagram. Such self-starting lines for Busemann intakes with weak and strong conical shock designs are shown for selected capture angles in Figs. 5–11 and 5–12. It is clear that decreasing the capture angle and thereby increasing overboard spillage improves starting characteristics of Busemann intakes. Furthermore, it is to be noted that the influence of capture angle is nonlinear. The gain in startability when decreasing capture angle from 360° (no spillage) to 180° (the "half-Busemann"case) is noticeably higher than that which could be achieved by further decrease of capture angle towards zero.

The application of the three theories presented above results in three sets of self-starting boundaries for any chosen design of Busemann intake. As shown in Figs. 5–11 and 5–12, the results based on the third theory (Theory III) show more improvement in startability via overboard spillage. To make this statement more clear at free-stream Mach number of 3, the variation of area ratio of self-started

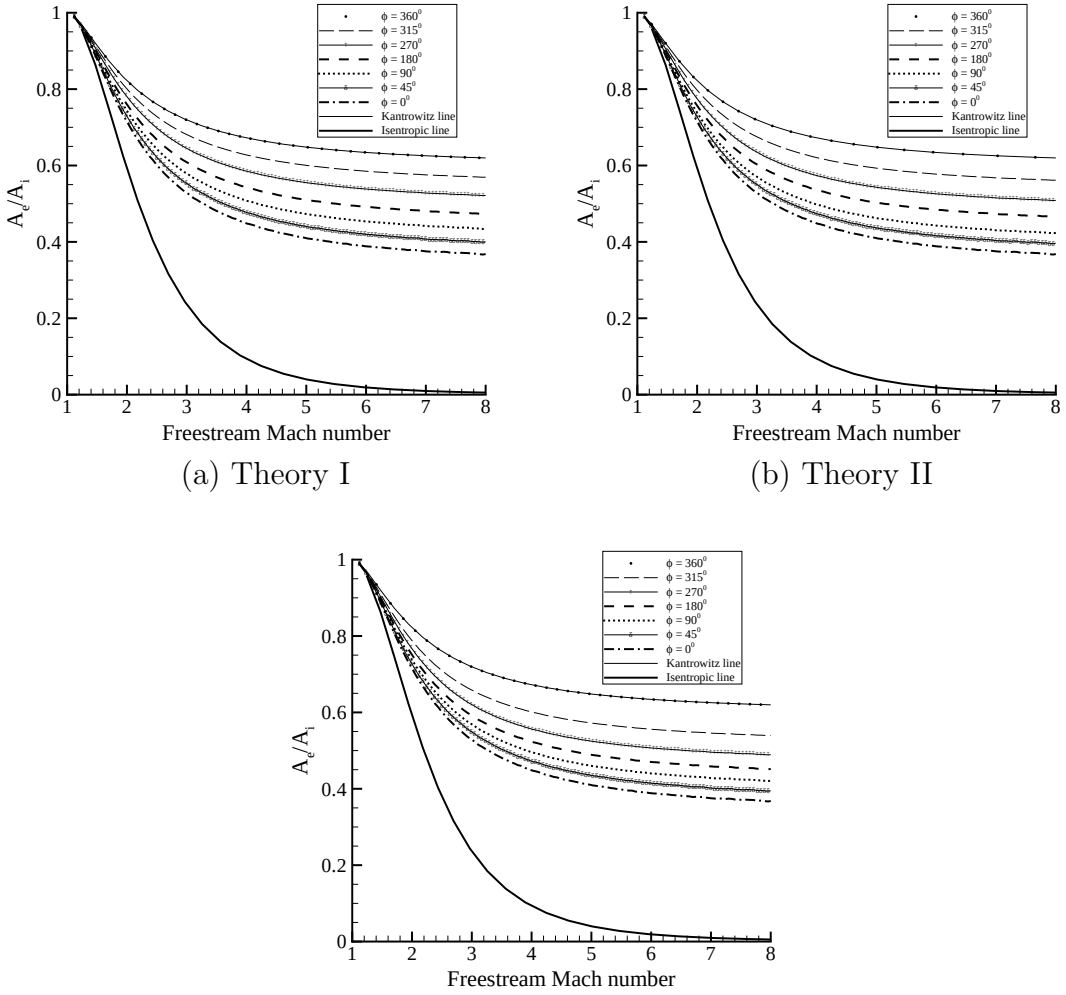

(a) Theory I

(b) Theory II

(c) Theory III

Figure 5–11: Self-starting limits of Busemann intakes with weak conical shock and different capture angles.

intakes with weak and strong conical shocks over the capture angle is plotted, Fig. 5–13, which confirm the above explanation. The self-starting Kantrowitz limits from the other two theories are close to each other. These theoretical predictions will be validated by 3D numerical starting experiments in Chapter 6.

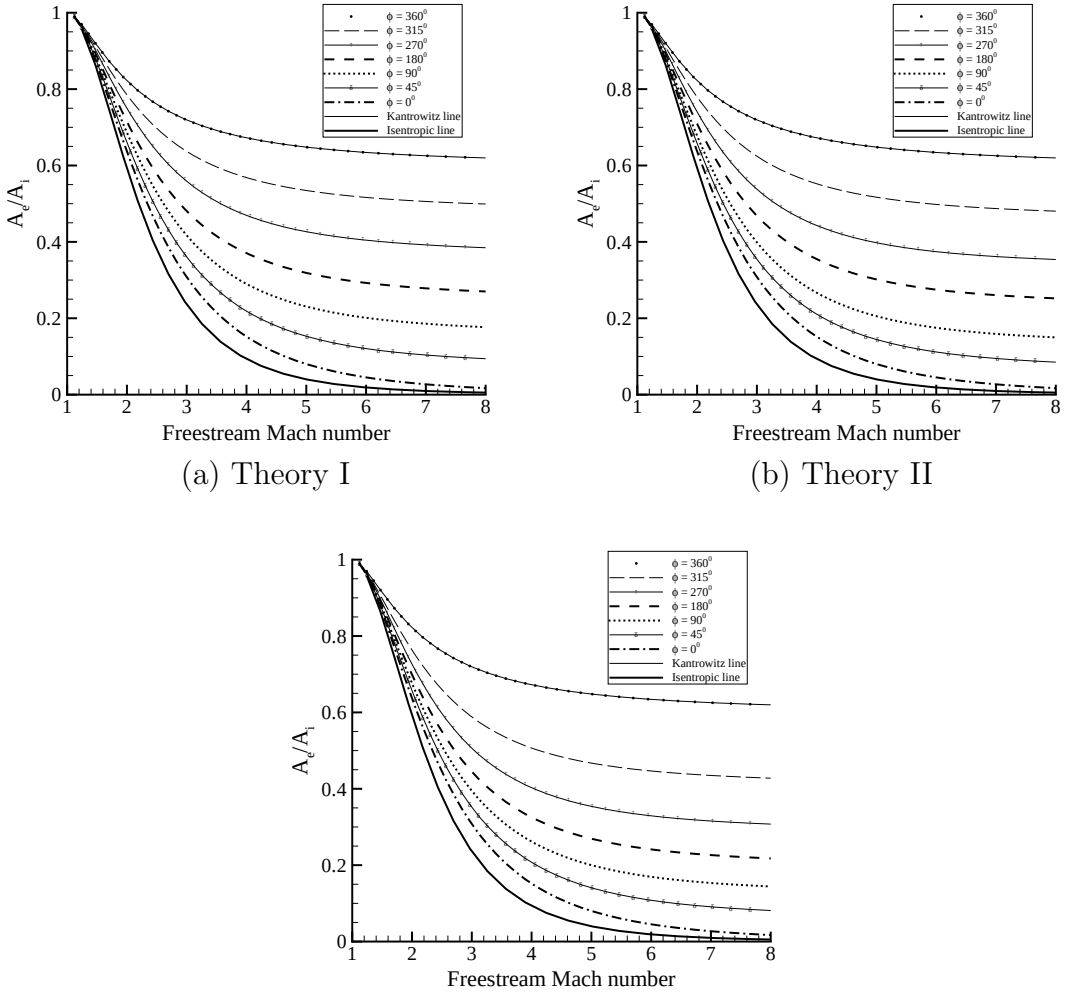

(a) Theory I

(b) Theory II

(c) Theory III

Figure 5–12: Self-starting limits of Busemann intakes with strong conical shock and different capture angles.

5.6 Normal-cut-design Busemann intakes

As mentioned before, the Busemann intakes can be also designed by issuing a line normal to the Busemann contour from the focal point and discarding the part of the contour downstream from the line. It means that the Busemann contour is

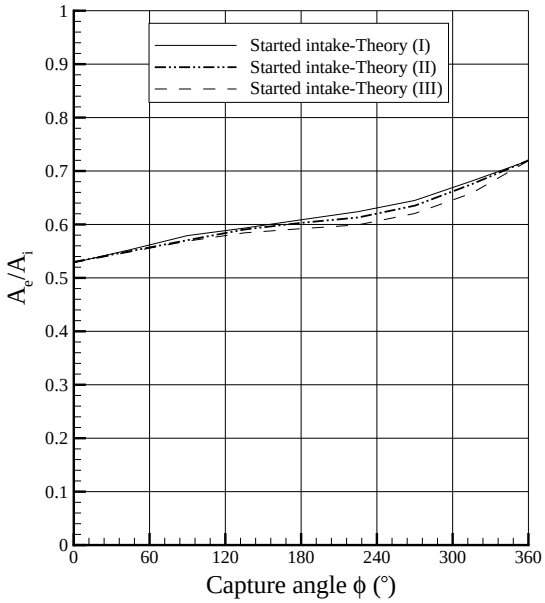

(a) Busemann intake with weak conical shock

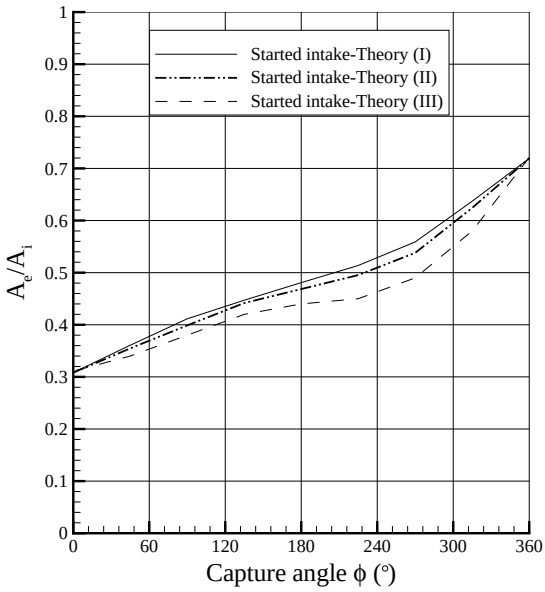

(b) Busemann intake with strong conical shock

Figure 5–13: Self-starting limits of Busemann intakes at free-stream Mach number of 3.

ended at the point with zero curvature, which results in an increase of the exit area as compared to the strong and weak shock designs (see Fig. 5–8) and better startability.

The starting analysis of thin Busemann intakes with normal-cut-designs based on weak or strong conical shocks (Figs. 5–9c and 5–9d) is carried out as explained in Section 5.5 to find the self-starting boundaries of these types of intakes. As shown in Fig. 5–7, the spontaneous starting limits for thin Busemann intakes with normal-cut designs are significantly lower than for other designs and very close to the isentropic line.

The exit area (and area ratio) change between the intake with weak conical shock (Fig. 5–8a) and its normal cut counterpart (Fig. 5–8c) is much greater than the one between the two designs involving strong shock (Figs. 5–8b and 5–8d). Therefore, as may be seen in Fig. 5–7, the improvement in startability via normal cut is much more significant for weak-shock-based intakes. However, the resulting self-starting lines for both normal cut designs are very close.

However, the normal cut design intakes will always produce a non-uniform exit flow pattern. It is an open question whether or not an appropriate pressure boundary condition at the exit would allow to actually have a strong conical shock in the flow for this design or the shock will always be a weak one. In any case, by the virtue of this design, the conical shock does not come to the trailing edge of the Busemann contour. Therefore, the expansion fan is generated at the trailing edge, which interacts downstream with the conical shock, with subsequent wave re-reflections from the intake's walls. That constitutes the primary source of flow non-uniformity in this design.

5.7 Started Busemann intake with weak/strong conical shock

As explained in Section 5.5, the Busemann intake can be designed on the basis of either a weak conical shock or a strong conical shock, see Figs. 5–8a and 5–8b. The flow downstream of a weak shock is supersonic while in the case of having a strong shock, the exit flow is subsonic with higher pressure loss. Figure 5–7 shows the Kantrowitz (self-starting) limits for thin Busemann intakes designed with weak and strong conical shocks which terminate at the trailing edge of the Busemann surface (Figs. 5–9a and 5–9b). The weak-shock-based design leads to a noticeable improvement in startability as compared to fully enclosed intakes: for high Mach numbers, contraction ratios of ~ 2.5 can be started spontaneously, in contrast to 1.7 value for fully enclosed intakes. However, the most significant improvement is achieved via the strong-shock-based design: for $M_\infty > 5$, contraction ratios of ~ 10 or higher can be started with the assistance of overboard spillage alone. Furthermore, for strong-shock-based intakes, the self-starting limit is just slightly above the self-starting lines for normal cut design intakes, which posses the best starting characteristics among Busemann intakes. It is to be recalled that the strong shock design principle was proposed and verified for planar intakes as a way to design intakes on the basis of a particular, well-defined flow and at the same time to get the self-starting area ratios which are close to the theoretical minimum for the intake family under consideration. In view of the results shown in Fig. 5–7, it appears that the strong shock design principle remains valid for Busemann intakes as well.

The capture angle effect on startability of these two designs of Busemann intakes is shown in Figs. 5–11 and 5–12. Clearly, the self-starting boundaries for these intakes

with overboard spillage are lower that the Kantrowitz line for a fully enclosed intake, i.e. increasing spillage by decreasing the capture angle improves startability. At the same free-stream Mach number and the same capture angle, the strong-shock design produces Busemann intakes with significantly lower self-starting area ratios (higher self-starting contractions).

It is to be noted that in the strong shock design intakes, the strong shock can be, in principle, maintained by the application of an appropriate back pressure. In that case, the strong shock design would allow to produce a uniform exit flow (although this flow is subsonic and with elevated total pressure losses due to strong shock). This possibility of having uniform exit flow, if desired, distinguishes the strong-shock-based design from the normal cut designs, which always result in non-uniform exit flow. If an appropriate back pressure is not maintained and/or supersonic exit flow is required, the strong-shock-based intake can be operate with a weak conical shock (not terminating at the trailing edge) and a non-uniform exit flow. As was the case for planar intakes, non-uniformity of the flow into the combustor would be a consequence of having better starting characteristics.

5.8 Conclusion

In this chapter, the properties of internal, conical, axisymmetric, Busemann flow are calculated using the Taylor-Maccoll and streamline equations. The Busemann flow is used to design Busemann air intakes for hyper/supersonic air-breathing engines.

A new way to introduce overboard spillage for Busemann intakes, without altering the started flow, is suggested by considering angular sectors or portions of

full Busemann intakes with different capture angles. Furthermore, in addition to the well-known Busemann intakes with a weak conical shock, three new designs of Busemann intakes are put forward: the strong-shock-based design and two so-called "normal cut" designs in which the downstream part of Busemann contour is truncated.

Three different theories based on geometrical considerations are developed to calculate the spillage amount for Busemann intakes with different capture angles. The startability analysis of different designs of Busemann intakes with overboard spillage is done using these theories. All obtained self-starting boundaries for Busemann intakes show significant improvement in startability of the intakes via overboard spillage. Among all considered designs, the normal cut design based on weak conical shock results in the lowest self-starting area ratios. However, the Busemann intakes designed with strong conical shock exhibit starting characteristics which are close to these lowest values. Therefore, the strong design principle appears to be valid in this case as well.

Considering the influence of capture angle alone on startability of Busemann intakes one may conclude that the influence of capture angle ϕ is nonlinear: the self-starting curves for $\phi \leq 180^\circ$ is noticeably closer to the limiting case of $\phi \simeq 0$ with the highest startability rather than to the case of fully enclosed Busemann intake ($\phi = 360^\circ$). It may be added here that practical usefulness of very thin intakes with small capture angles is questionable in spite of their better starting characteristics.

The differences between the theoretical results are due to the fact that the evaluation of overboard spillage effect is based on different purely geometrical considerations. It is to be noted that for Busemann intakes, the quasi-steady starting process assisted by overboard spillage involves a complex, 3D flow. It appears to be impossible to validate the developed analytical treatment of self-starting boundaries without numerical simulation of intake starting, which is undertaken in the next chapter.

CHAPTER 6
Computational Startability Analysis of Busemann Intakes

6.1 Introduction

This chapter of the present study is devoted to the numerical experiments for the determination of the minimum self-starting area ratios of Busemann intakes with provisions for overboard spillage. The numerical simulations are done using 2D and 3D unstructured adaptive Euler finite-volume flow solvers. As mentioned before in Chapter 3, these codes are free from any assumptions regarding flow symmetry and characteristics. Therefore, reproduction of the steady axisymmetrical Busemann flow in the started mode serves as additional verification of the codes. Methodology of numerically finding the minimum self-starting area ratios at a given free-stream Mach number, discussed in Chapter 3, is applied to Busemann intakes of various designs with different capture angles at free-stream Mach numbers 3.0 and 4.0.

6.2 General 3D model and special cases

6.2.1 3D Busemann intake simulations

The Busemann contour for the intake to be tested is found by integrating the Taylor-Maccoll and streamline equations as described in Section 5.3. The contour is then imported into AutoCAD 2011 software (later on, AutoCAD design suite 2013 is used) to create the 3D geometry of the computational domain, e.g., see Fig. 3–2. It includes the Busemann surface, two flat plates with the leading edges forming the

Mach angle with the free-stream direction and the external surfaces of the domain. The angle between the flat plates corresponds to the chosen value of capture angle.

The mesh is then generated using the existing open source software (OpenCASCADE and Netgen libraries [144,145]) and then, the intake starting experiment is carried out with Candifix code using the boundary conditions and methodology discussed in Chapter 3.

As explained in Chapter 3, many 3D numerical starting experiments are required to determine just one minimum self-starting area ratio for a given intake geometry, which is defined by the intake's design type and its capture angle, and free-stream Mach number. Each of those experiments consists of a few stages, e.g., the computation of steady-state flowfield with the closed exit at first and then, the computation till another steady-state (started or unstarted) is reached after the exit is open, etc. Each 3D simulation is time-consuming. In view of all that the present study is limited to numerical starting experiments for two intake designs: the weak-shock-based design and the strong-shock-based design (Figs. 5–8a and 5–8b). For each design two free-stream numbers ($M_\infty = 3.0$ and $M_\infty = 4.0$) and 9 capture angles are considered. Numerical starting trials for 3D normal-cut design intakes delegated to future studies.

6.2.2 Busemann intakes with capture angles of 0° and 360°

Unstarted flows for Busemann intakes with overboard spillage are 3D flows; therefore, in 3D simulations, an external flow region must be added as shown in Fig. 3–2 to accommodate the bow shock and the spilling flow. However, two limiting

cases of Busemann intakes, with $\phi = 0°$ and $\phi = 360°$, represent an exception as explained below.

The limiting case with capture angle of 360° (fully enclosed intake) is fully axisymmetric and can be studied with a 2D code, e.g. Masterix [140]. The cases with low values of capture angle ϕ pose considerable challenge because the intake becomes very narrow and it is not a simple task to generate good quality 3D mesh inside the intake and in the surrounding region. This reason leads us to analyze this case with a 2D code as well. Indeed, in the limit $\phi \to 0$, the three-dimensional Euler equations turn into the axisymmetrical Euler equations. Then, one may set-up axisymmetrical simulations in the computational domain containing only the intake's interior as shown in Fig. 6–1 without any external surrounding domain. The Mach line would then serve as the inflow boundary upstream of which the free-stream values are specified. It is obvious that in a started case, Busemann flow would be reproduced exactly, see Fig. 6–1a. However, in an unstarted case, a bow shock appears (Fig. 6–1b) with some spillage taking place through the inflow boundary. Such axisymmetrical simulation may not predict the amount of spillage correctly (that is only possible with full 3D simulation), i.e., the predicted location of the bow shock, in general, would not agree well with the corresponding 3D simulation. However, since the minimum self-starting area ratio corresponds to the amount of overboard spillage exactly equal to zero, the inability of the axisymmetric model to accurately reproduce unstarted flow with non-zero spillage is irrelevant, and it is expected that the starting boundary itself would be accurately predicted.

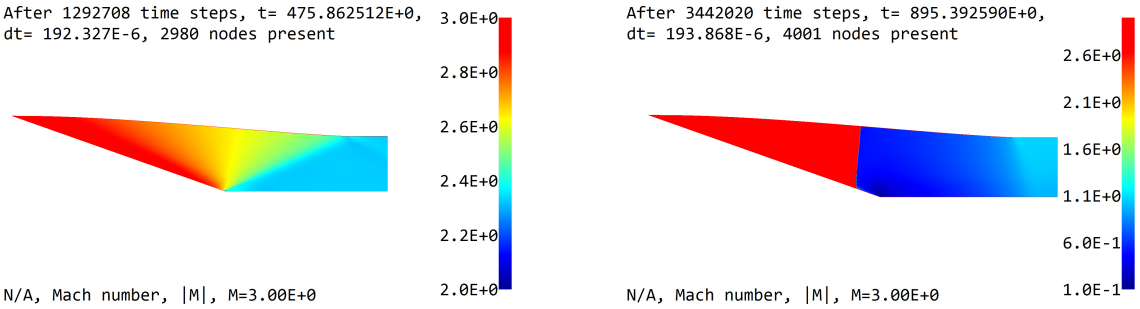

(a) Started flow at area ratio of 0.531 (b) Unstarted flow at area ratio of 0.528

Figure 6–1: Startability analysis of a thin Busemann intake (capture angle $\phi \to 0$) at free-stream Mach number of 3. The bottom line corresponds to the axis of symmetry. The flow is from left to right.

The validity of this method for $\phi \to 0$ is confirmed by applying it to the analysis of startability of two-shock ramp intakes at free-stream Mach numbers of 3, 3.5 and 4. These intakes are planar and, therefore, it is possible to use both approaches: (a) the traditional one in which the computational domain includes both the intake's interior and a surrounding region (Fig. 6–2a), when this approach used to obtain the results presented in Chapter 4, (b) the newly proposed method in which the computational domain contains only the intake's interior with the inflow boundary being at the line connecting the leading edge of the ramp with the cowl lip (Fig. 6–2b). Numerical results demonstrate that both approaches give the same outcome of starting experiments (the same self-starting boundary as in Chapter 4), and, therefore, the new method can be used with confidence.

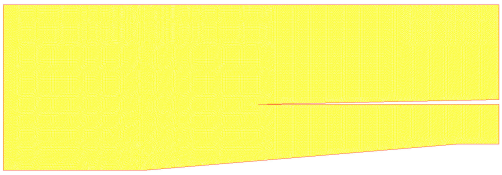

(a) The domain including both the intake's interior and surrounding region.

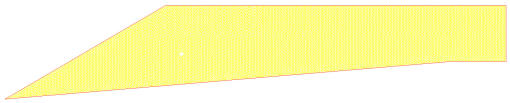

(b) The domain including only the intake's interior.

Figure 6–2: Computational domains for two-shock ramp intake analysis.

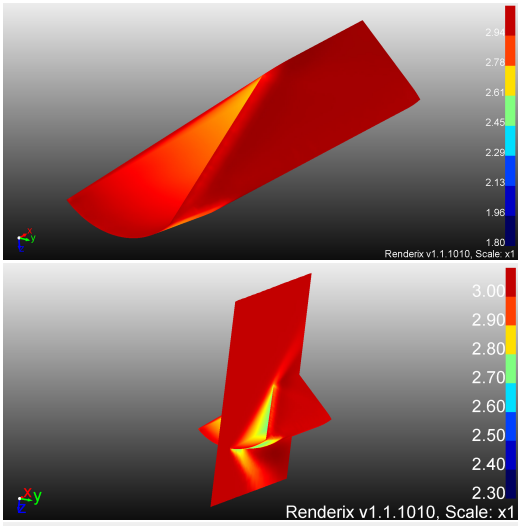

(a) Started flow at $\frac{A_e}{A_i} = 0.58$

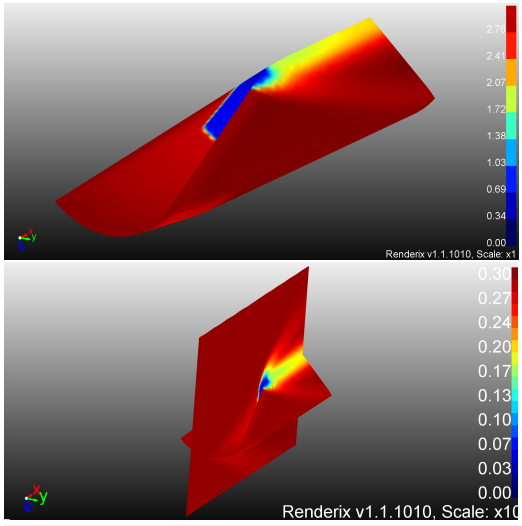

(b) Unstarted flow at $\frac{A_e}{A_i} = 0.56$

Figure 6–3: Numerical flowfields in Busemann intakes with weak shock design and capture angle $\phi = 90°$ at free-stream Mach number of 3. Mach number distributions are shown.

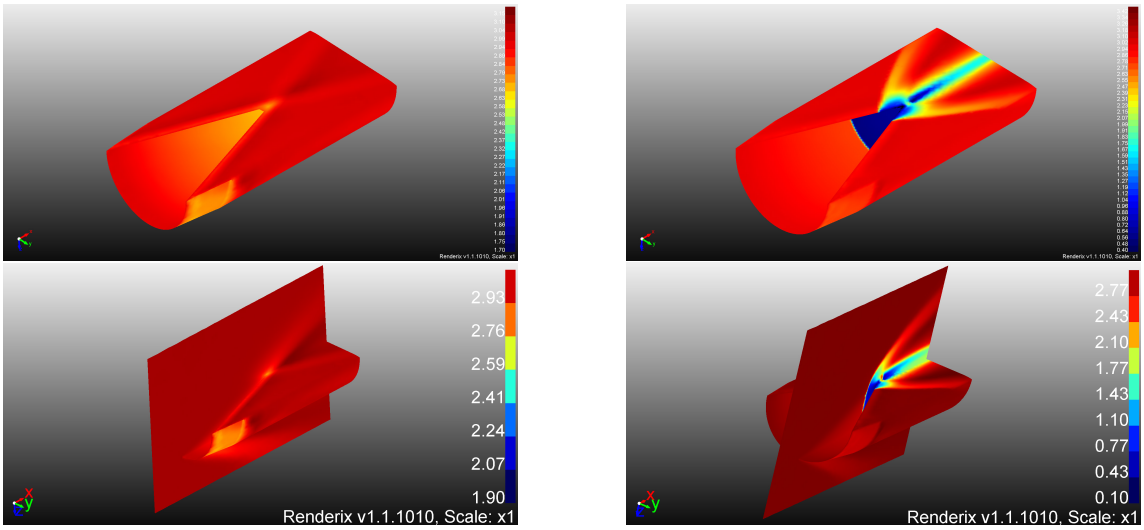

(a) Started flow at $\frac{A_e}{A_i} = 0.60$ (b) Unstarted flow at $\frac{A_e}{A_i} = 0.59$

Figure 6–4: Numerical flowfields in Busemann intakes with weak shock design and capture angle $\phi = 180°$ at free-stream Mach number of 3. Mach number distributions are shown.

6.3 Results

6.3.1 Busemann flowfields

Figures from 6–3 to 6–8 show the started and unstarted flowfields for Busemann intakes with weak and strong shock designs and capture angles of 90°, 180° and 270° at free-stream Mach number of 3.0.

Each figure includes the started flow at the lowest area ratio for which numerical experiments for the given geometry and Mach number resulted in started outcome and the unstarted flow at the highest area ratio for which unstarted outcome was registered. For example, in Fig. 6–3, for the weak-shock design and $\phi = 90°$, the started flow is at the area ratio $A_e/A_i = 0.58$ and the unstarted flow is at the area ratio $A_e/A_i = 0.56$, so that the numerical self-starting boundary may be assumed to

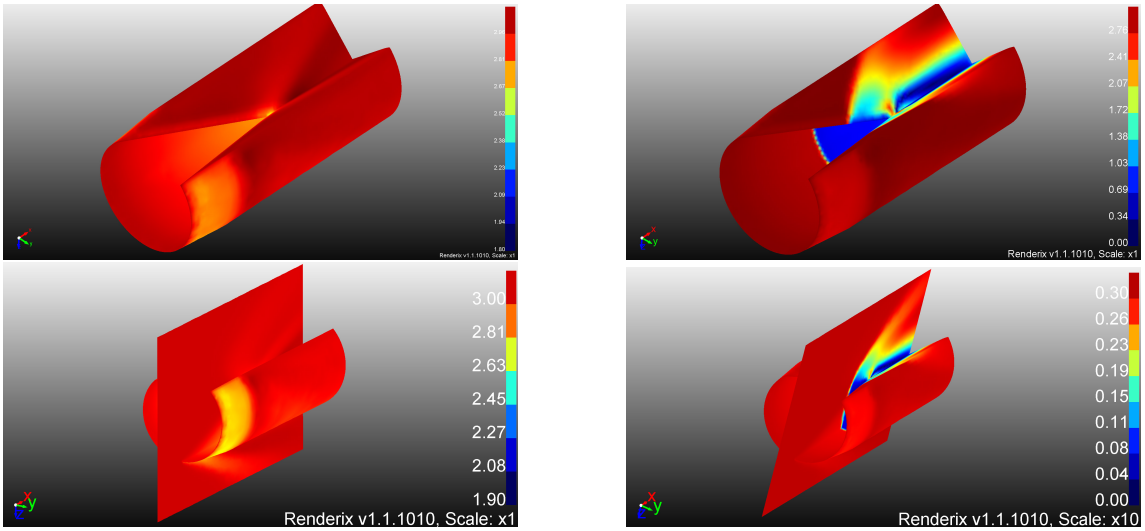

(a) Started flow at $\frac{A_e}{A_i} = 0.62$ (b) Unstarted flow at $\frac{A_e}{A_i} = 0.61$

Figure 6–5: Numerical flowfields in Busemann intakes with weak shock design and capture angle $\phi = 270°$ at free-stream Mach number of 3. Mach number distributions are shown.

be at $A_e/A_i = 0.57$. For each area ratio, the set of images contain 3D view of the intake's surfaces (top image) and the same view with the symmetry plane (middle or bottom image). In some cases (e.g. Fig. 6–3) the view in the symmetry plane is added as a separate image at the bottom.

The flowfield views for started cases show that all the contours converge towards the Busemann flow focal point (which coincides with the tip of the V-shaped opening), thus qualitatively indicating that the flow is conical and the Busemann flow is reproduced in the simulations. In the unstarted cases, the bow shock stand-off distance is, at first glance, rather large (see, e.g., Fig. 6–3b, bottom image), given

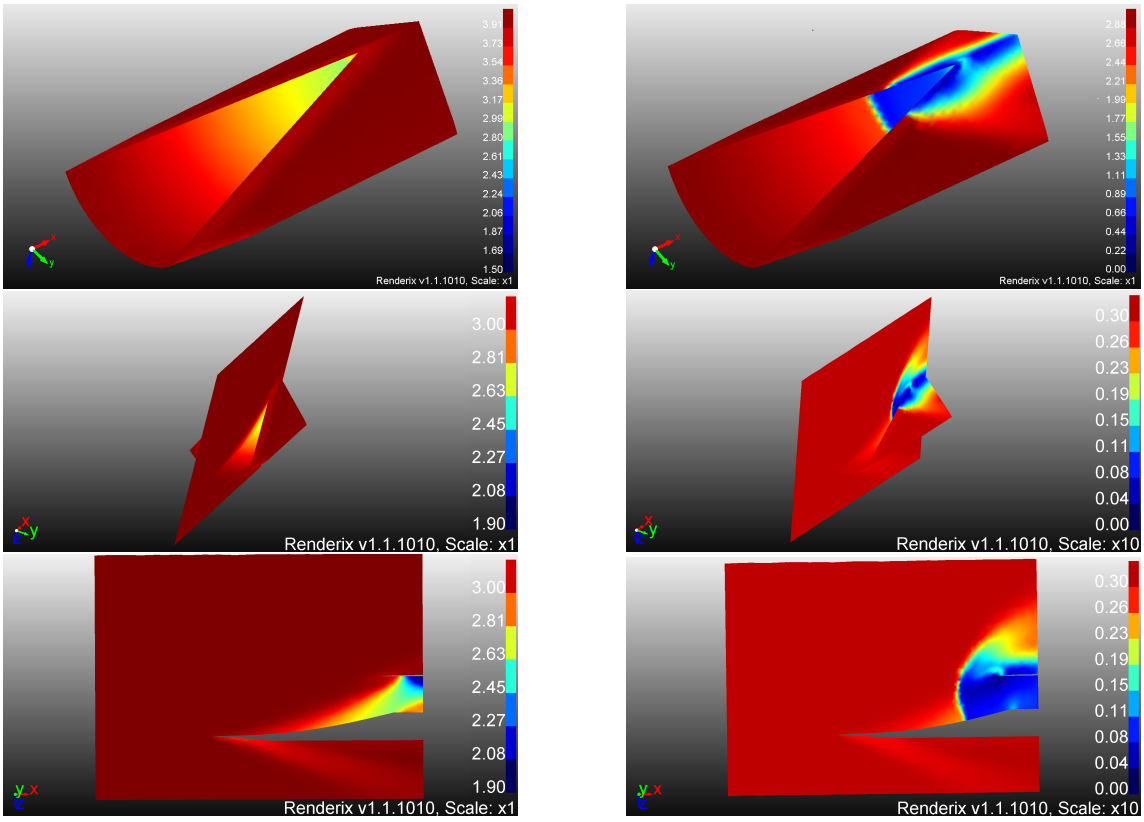

(a) Started flow at $\frac{A_e}{A_i} = 0.38$ (b) Unstarted flow at $\frac{A_e}{A_i} = 0.36$

Figure 6–6: Numerical flowfields in Busemann intakes with strong shock design and capture angle $\phi = 90°$ at free-stream Mach number of 3. Mach number distributions are shown.

that the area ratio is very close to the self-starting limit. However, one should consider that the V-opening is of triangular geometry and narrow so that the stand-off distance should be sufficient to provide the required spillage area.

In the present simulations, for weak shock design intakes in the started case, the Busemann flow is well reproduced (e.g. Fig. 6–3a), i.e. the weak conical shock terminates at the trailing edge of the Busemann contour and the exit flow is uniform. In the started mode for strong shock design intakes, the shock is of weak family and

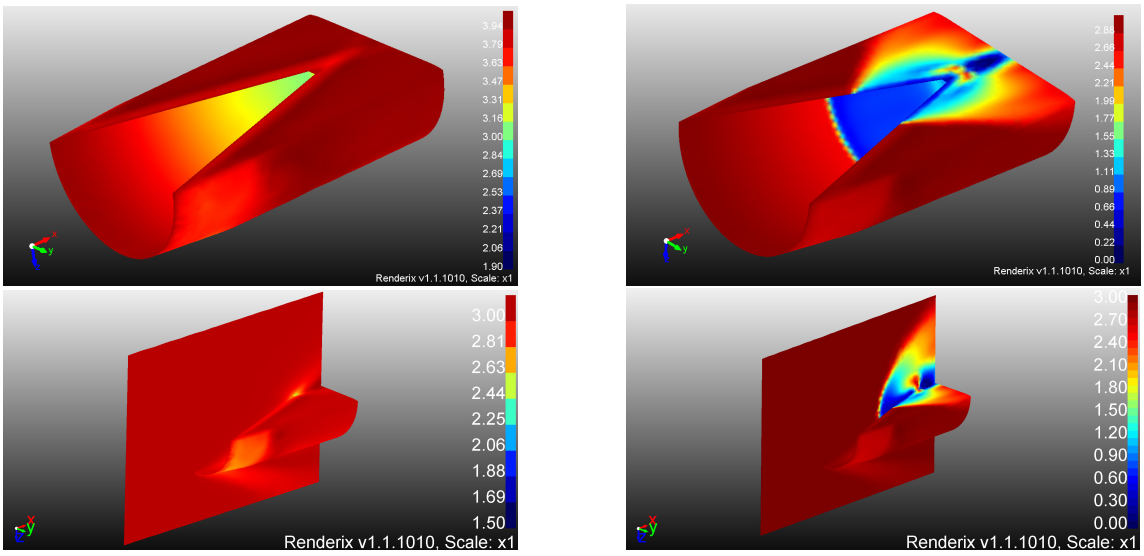

(a) Started flow at $\frac{A_e}{A_i} = 0.44$ (b) Unstarted flow at $\frac{A_e}{A_i} = 0.42$

Figure 6–7: Numerical flowfields in Busemann intakes with strong shock design and capture angle $\phi = 180°$ at free-stream Mach number of 3. Mach number distributions are shown.

does not come to the trailing edge, thus, producing a non-uniform supersonic exit flow (Fig. 6–6a). This is because no special boundary conditions were applied at the exit to induce the strong shock solution and in such a case, a weak shock is generated in the course of flow starting.

To provide quantitative comparison of numerical and analytical solutions for Busemann flow, the variation of flow Mach number, pressure and density on Busemann surface are shown in Figs. 6–9, 6–10 and 6–11 for started flows in "half-Busemann" ($\phi = 180°$) intakes with weak and strong shock designs at $M_\infty = 3$. Analytical results (Section 5.3) are shown as a solid line while numerical data are displayed with symbols. It is to be especially emphasized that the numerical values do *not* represent the data in particular cross-section by a plane containing the axis

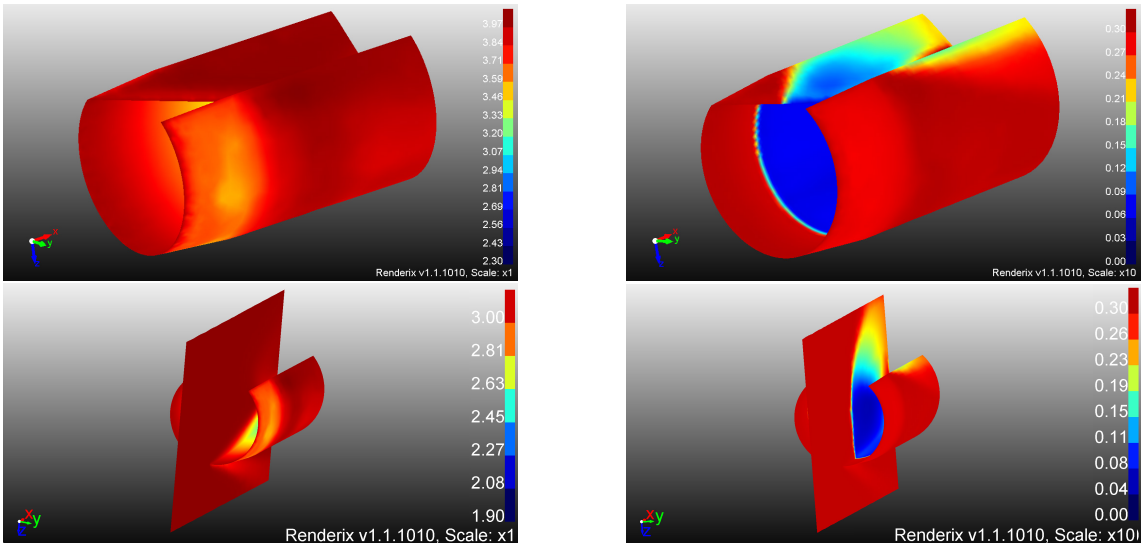

(a) Started flow at $\frac{A_e}{A_i} = 0.49$ (b) Unstarted flow at $\frac{A_e}{A_i} = 0.47$

Figure 6–8: Numerical flowfields of Busemann intakes with strong shock design and capture angle $\phi = 270°$ at free-stream Mach number of 3. Mach number distributions are shown.

of symmetry. *All* points belonging to the Busemann surface are plotted in Figs. 6–9, 6–10 and 6–11. Ideally, the numerical points should lie on a single line. Thus, the scatter of the numerical data allows to judge how well the axisymmetrical nature of Busemann flow is reproduced in numerical simulations.

The following conclusions can be drawn from Figs. 6–9, 6–10 and 6–11. Overall, there is a very good agreement between the analytical and numerical data taking into account that it is 3D modeling with relatively coarse meshes (e.g. as compared to the ones which can be used in 2D simulations of the same flows). This gives additional confidence in the flow solver used in the presents sturdy.

The largest discrepancy for flow Mach number is $\sim 1.8\%$ for the case shown in Fig. 6–9a. The angular scatter of numerical values is below 1% (again, the worst case

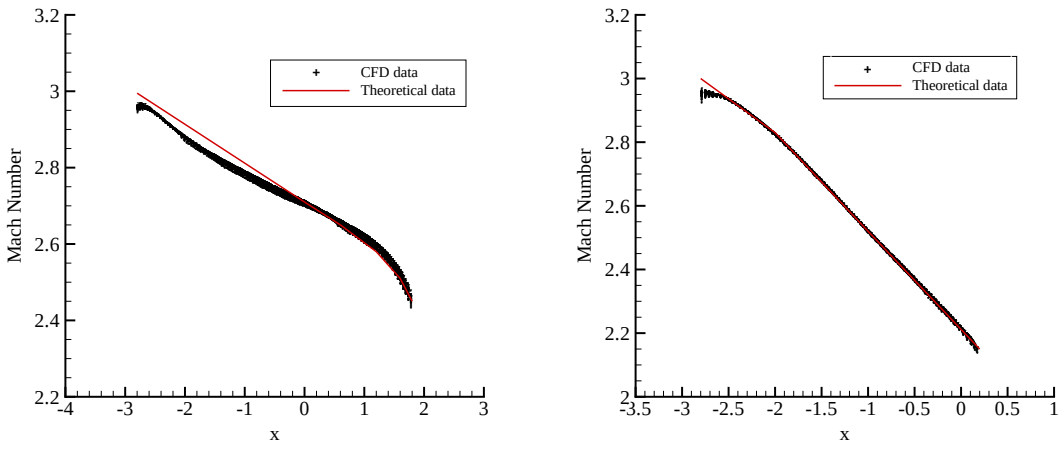

(a) Intake designed with weak shock (started flow at $\frac{A_e}{A_i} = 0.60$)

(b) Intake designed with strong shock (started flow at $\frac{A_e}{A_i} = 0.44$)

Figure 6–9: Mach number variation along the wall of the started half-Busemann ($\phi = 180°$) intake at free-stream Mach number of 3.0.

is the one shown in Fig. 6–9a). The main difference between the analytical distribution and the numerical values is near and downstream from the intake's leading edge. In the analytical solution, at the leading edge, the wall angle and flow deflection are zero. Finite size of grid cells in numerical simulation results in a small wall angle near the leading edge, which induces a weak but finite compression fan/shock wave, thus reducing flow Mach number and increasing pressure downstream of it. The influence of this wave decreases downstream and the numerical solution eventually returns to the analytical curve. Furthermore, the grid control volumes for nodes belonging to the intake's leading edge include both the intake's interior region and some part of the external domain. The solution averaging inside such control volumes results is

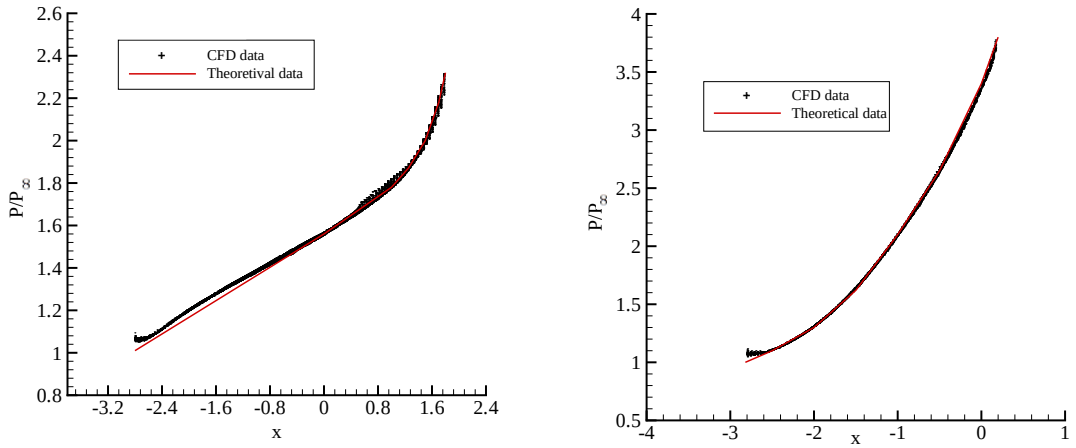

(a) Intake designed with weak shock (started flow at $\frac{A_e}{A_i} = 0.60$)

(b) Intake designed with strong shock (started flow at $\frac{A_e}{A_i} = 0.44$)

Figure 6–10: Pressure variation along the wall of the started half-Busemann ($\phi = 180°$) intake at free-stream Mach number of 3.0.

another reason for the deviation from the analytical solution. Grid refinement studies shown in Fig. 6–12 for the $M_\infty = 3$, $\phi = 45°$, weak shock design case, clearly demonstrate that the effect of the above mentioned control volumes decreases with grid refinement. It is to be noted that in this grid refinement study, the nodes are added only in the vicinity of high solution gradients while the grid in the smooth parts of the flow and the background grid is not refined. That is why some deviation of the numerical results from the exact solution is still seen in Fig. 6–12d. To eliminate it, uniform grid refinement is to be performed, which is computationally very costly. It is to be also noted that, as explained in Section 3.3, the change of grid refinement levels from 0 (background grid) to 3 do not have any effect on the self-starting area ratio (the outcomes of numerical experiments remain the same).

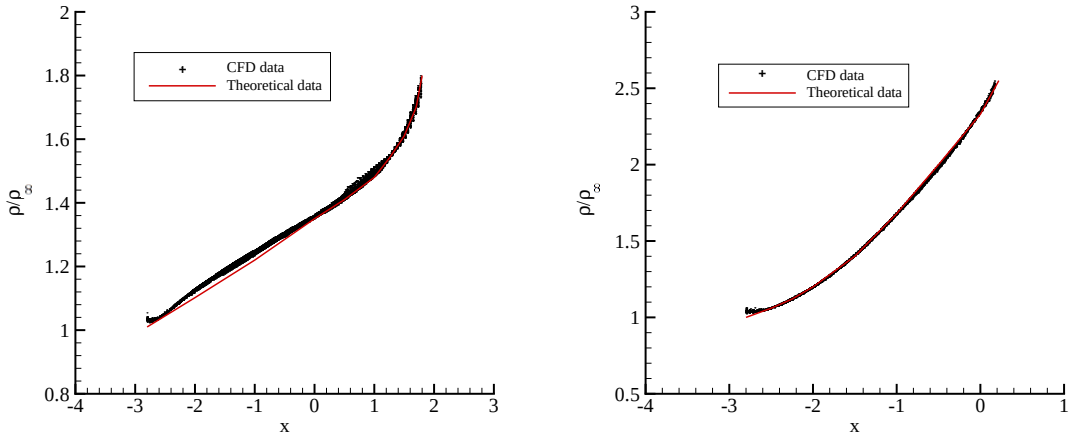

(a) Intake designed with weak shock (started flow at $\frac{A_e}{A_i} = 0.60$)

(b) Intake designed with strong shock (started flow at $\frac{A_e}{A_i} = 0.44$)

Figure 6–11: Density variation along the wall of the started half-Busemann ($\phi = 180°$) intake at free-stream Mach number of 3.0.

It may be conjectured that there may be some influence if one would try to narrow down the differences between the started and unstarted area ratios, i.e., for example, to determine the self-starting area ratio with an accuracy better than 0.56-0.58 for the case shown in Fig. 6–3.

6.3.2 Results of starting experiments

2D simulation results

The numerical computation for started fully enclosed Busemann intakes ($\phi = 360°$) results in minimum area ratios of 0.721 and 0.675 for started intakes at free-stream Mach numbers of 3 and 4, respectively. At $M_\infty = 3$, the numerical area ratio of unstarted fully enclosed Busemann intakes is 0.705 while at $M_\infty = 4$, it is $(A_e/A_i)_{unstarted} = 0.665$. Thus, the numerical self-starting area ratios of these intakes

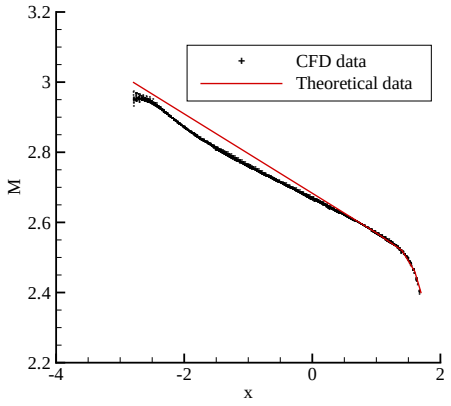

(a) No grid refinement level

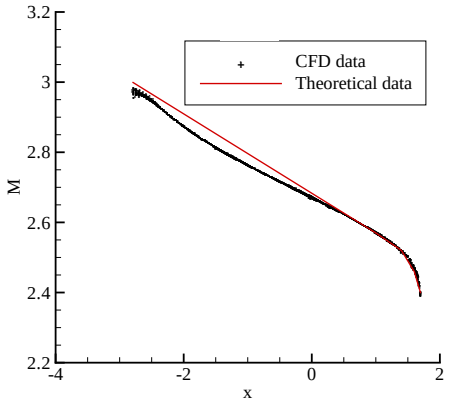

(b) Grid refinement level of 1

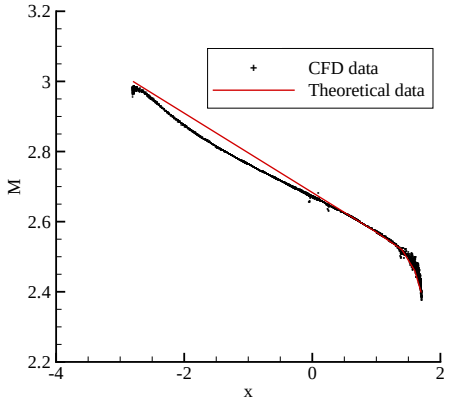

(c) Grid refinement level of 2

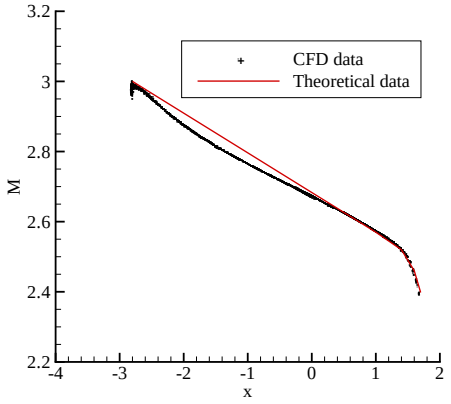

(d) Grid refinement level of 3

Figure 6–12: Mach number variation along the wall of the started Busemann intake designed with weak shock using numerical simulations with different grid refinement levels ($\phi = 45°$ and $M_\infty = 3$).

to compare with the theoretical ones are 0.713 and 0.670 at $M_\infty = 3$ and $M_\infty = 4$, respectively. The results are in excellent agreement with the theoretical values of 0.71922 and 0.67234. The minimum self-starting area ratios of thin Busemann intakes ($\phi \longrightarrow 0°$) designed with weak conical shock which terminates at the trailing edge of

the Busemann surface contour are found to be 0.529 ($M_\infty = 3$) and 0.442 ($M_\infty = 4$). These results are also in good agreement with the theoretical values of 0.52845 ($M_\infty = 3$) and 0.44840 ($M_\infty = 4$) for the self-starting boundaries. Similar level of agreement is found between the theoretical and numerical minimum self-starting area ratios of thin Busemann intakes designed with strong conical shock which terminates at the trailing edge of the Busemann contour. In this case, the numerical simulations result in the minimum self-starting area ratios of 0.300 ($M_\infty = 3$) and 0.146 ($M_\infty = 4$) while the theoretical results are 0.30818 ($M_\infty = 3$) and 0.15211 ($M_\infty = 4$). Slight difference between the theoretical and numerical results may be explained in the same way as it was done in Chapter 4 for ramp intakes. The Kantrowitz theory is based on the assumption of quasi-one-dimensional, quasi-steady isentropic flow downstream from the normal shock while in numerical simulations these conditions are met only with a certain accuracy.

The theoretical results (Chapter 5) indicate that thin ($\phi = 0°$) Busemann intakes with normal cut designs have the lowest minimum self-starting area ratios. As mentioned in Section 6.2.1, the present study does not include 3D numerical starting trials for intakes with normal cut designs. However, less time-consuming 2D simulations for such intakes are carried out.

The startability limits of the normal-cut-design thin Busemann intakes based on Busemann flow with weak and strong conical shocks are very close to each other (Fig. 5–7). So that it would be very difficult to resolve this small difference even in 2D numerical simulations. Therefore, the normal cut design based on weak shock is

chosen for modeling. At free-stream Mach numbers of 3 and 4, the minimum self-starting area ratios of the normal-cut-design thin Busemann intakes based on weak shock are found numerically to be 0.250 and 0.113. The theoretical minimum self-starting area ratios of normal-cut-design thin Busemann intakes with weak conical shock are 0.24843 and 0.10416 at $M_\infty = 3$ and $M_\infty = 4$ and in the case of having normal-cut-design thin Busemann intakes with strong conical shock, these values are $\left(\frac{A_e}{A_i}\right)_{started-(M_\infty=3)} = 0.25554$ and $\left(\frac{A_e}{A_i}\right)_{started-(M_\infty=4)} = 0.10985$. The values are in good agreement with the above mentioned numerical values.

3D simulation results for various capture angles

As mentioned in the previous chapters, the numerical flow solver used in this study does not have the provisions for variable geometry. Therefore, at each design point, an independent starting trial must be conducted. For a given free-stream Mach number M_∞ and a capture angle ϕ, numerical experiments are conducted for intakes with various area ratios with the goal to narrow down the gap between the minimum area ratio resulting in started flow and the maximum area ratio resulting in unstarted flow, as shown in Fig. 6–13.

Symbols in Fig. 6–13 represent the outcomes of starting processes for half-Busemann ($\phi = 180°$) intakes at $M_\infty = 3$ with various area ratios. Since the Kantrowitz limit is not known a prior and the suggested theories, as shown below, do not always provide with a good initial guess, many simulations may be required to get a single point on the starting boundary (see Fig. 6–13).

The numerical results for the minimum self-starting area ratios of the Busemann intakes designed with weak/strong conical shock, which terminates at the trailing

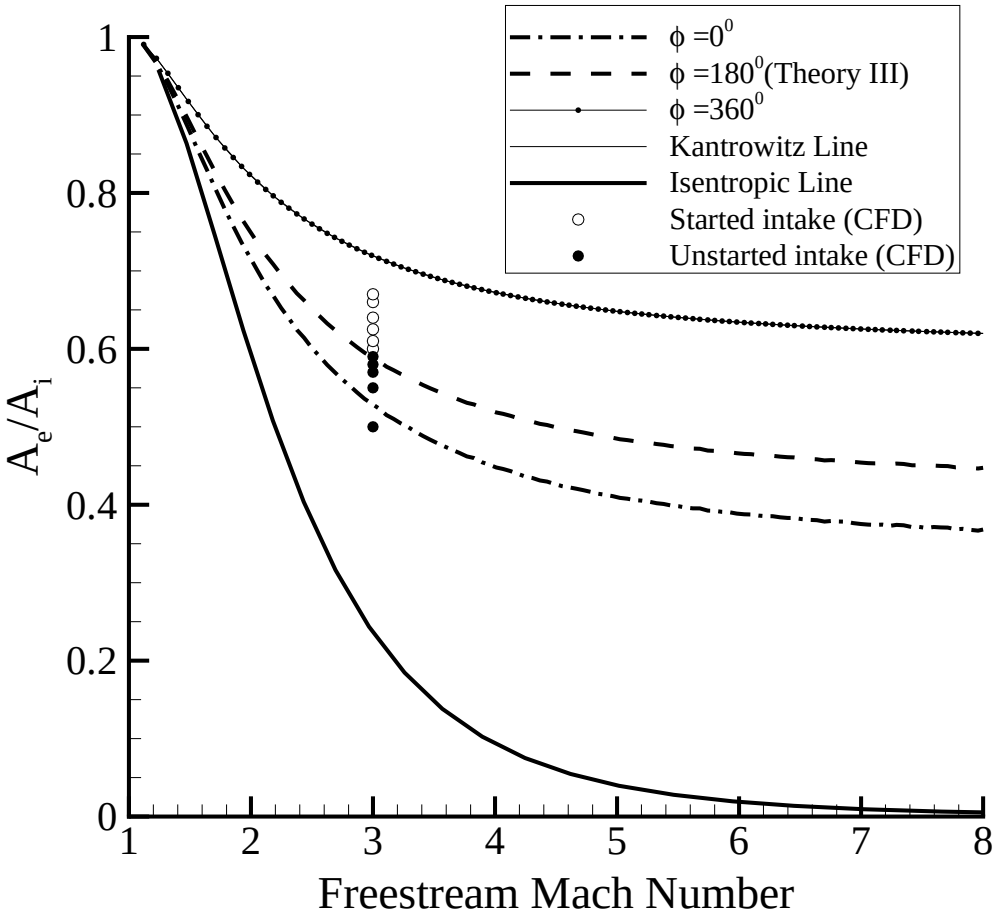

Figure 6–13: Results of numerical experiments for on-design half-Busemann ($\phi = 180°$) intake at $M_\infty = 3$.

edge of the Busemann surface contour, and capture angles of 45°, 90°, 135°, 180°, 225°, 270° and 315° at the design Mach numbers of 3 and 4 are shown in Figs. 6–14, 6–15, 6–16, and 6–17 and Tables 6–1 and 6–2. The results of 2D simulations for $\phi = 0°$ and $\phi = 360°$ are included as well. The theoretical results for all three suggested theories are shown in these figures and tables, too.

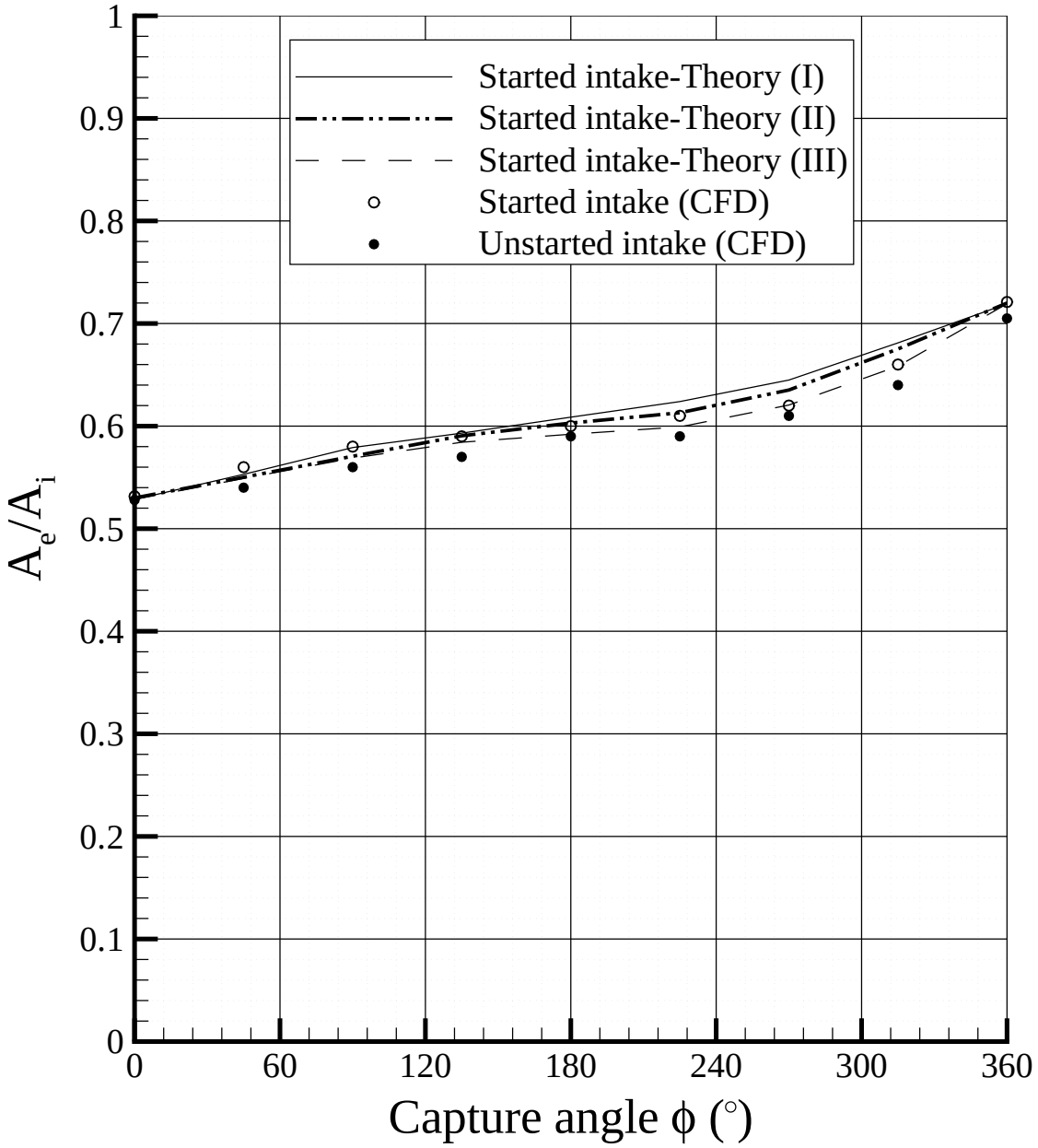

Figure 6–14: Theoretical and numerical self-starting area ratios A_e/A_i vs. capture angle ϕ for Busemann intakes designed with weak conical shock for $M_\infty = 3$.

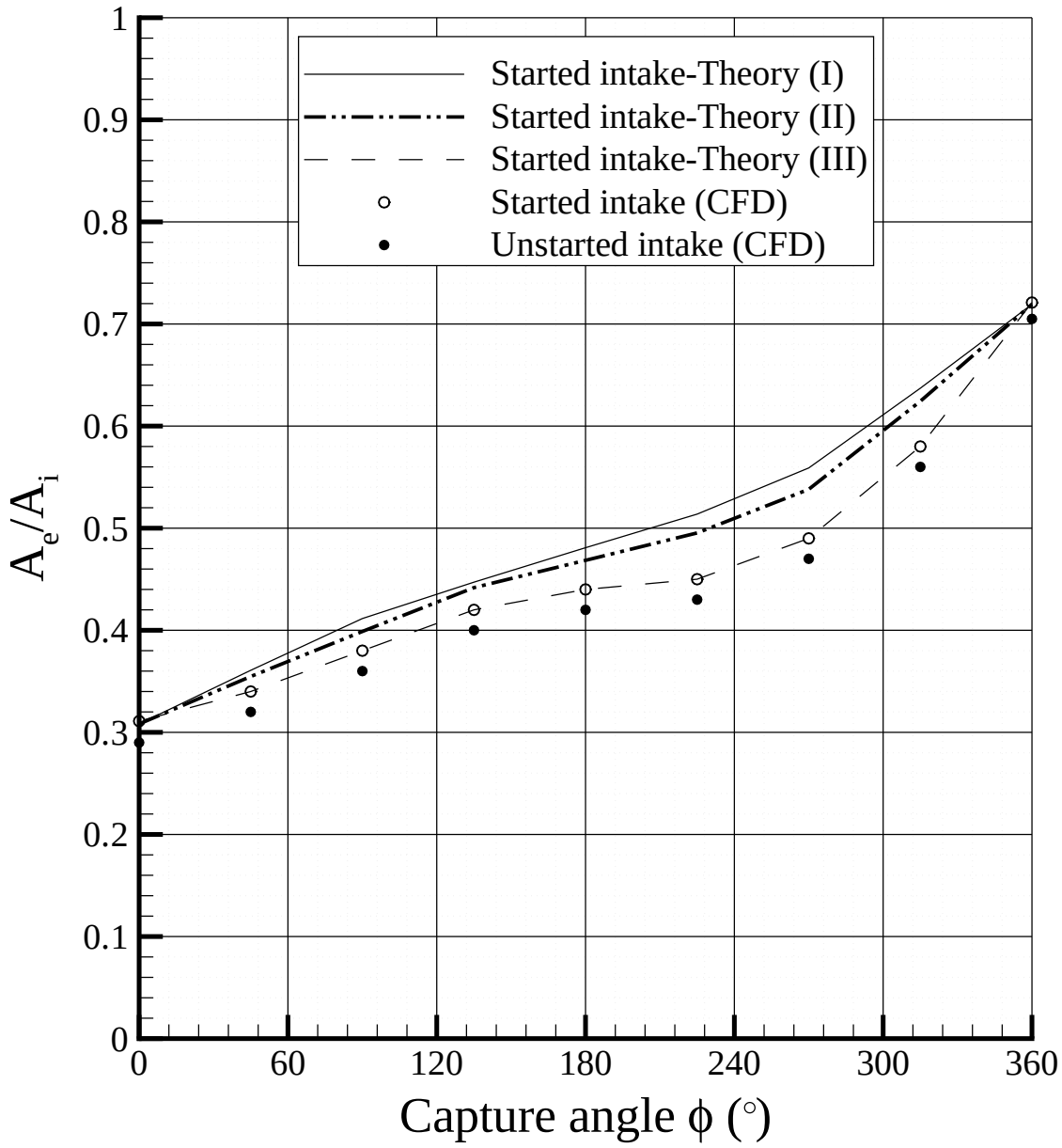

Figure 6–15: Theoretical and numerical self-starting area ratios A_e/A_i vs. capture angle ϕ for Busemann intakes designed with strong conical shock for $M_\infty = 3$.

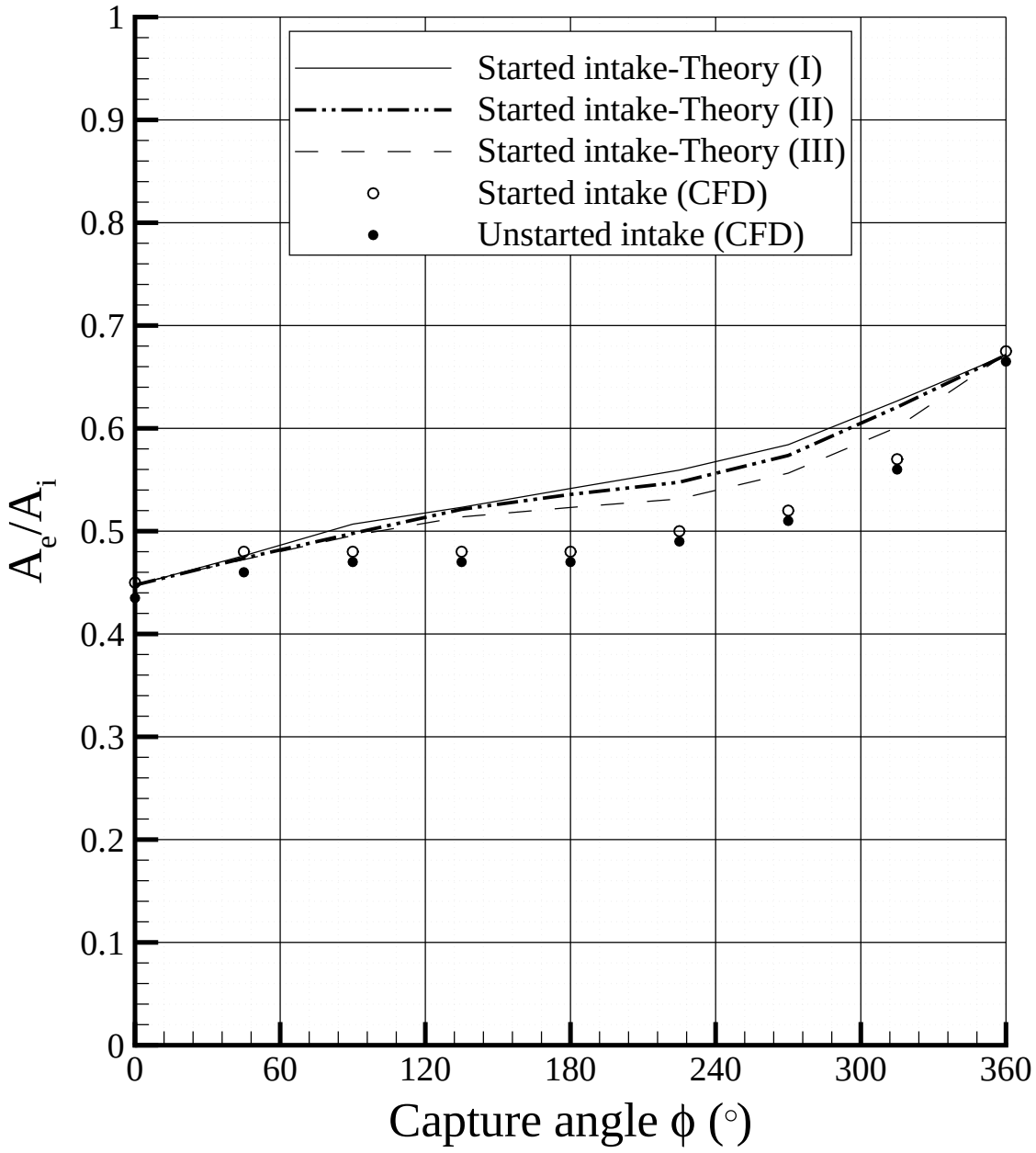

Figure 6–16: Theoretical and numerical self-starting area ratios A_e/A_i vs. capture angle ϕ for Busemann intakes designed with weak conical shock for $M_\infty = 4$.

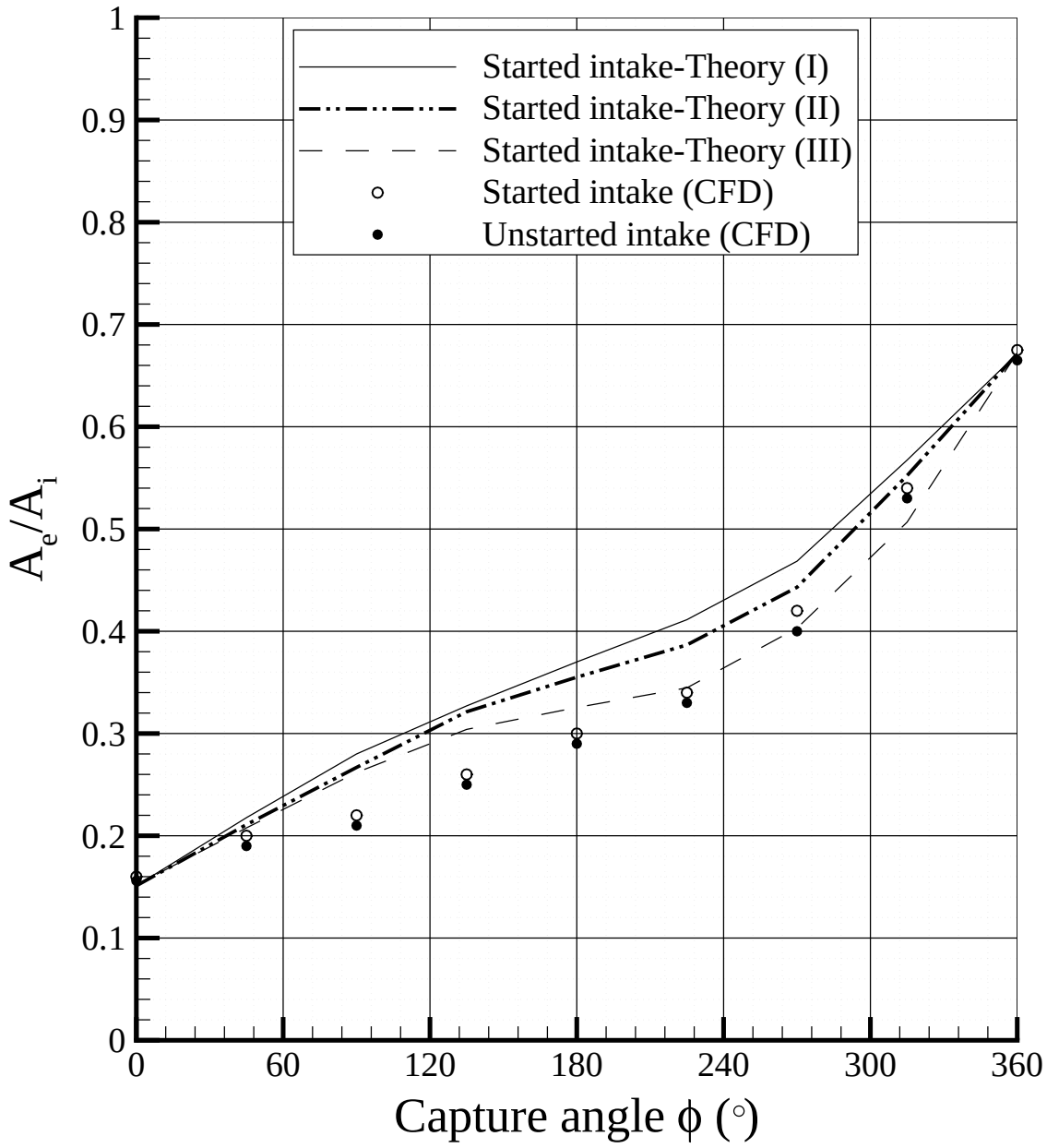

Figure 6–17: Theoretical and numerical self-starting area ratios A_e/A_i vs. capture angle ϕ for Busemann intakes designed with strong conical shock for $M_\infty = 4$.

Table 6–1: Capture angle effect on startability of Busemann intakes designed with weak conical shock.

M_∞	ϕ°	$\frac{A_e}{A_i}_{Started-Theory}$			$\frac{A_e}{A_i}_{Started}$	$\frac{A_e}{A_i}_{Unstarted}$
		Theory(I)	Theory(II)	Theory(III)	CFD	CFD
3	360	0.71922	0.71922	0.71922	0.721	0.705
	315	0.68114	0.67520	0.65842	0.660	0.640
	270	0.64489	0.63515	0.62051	0.620	0.610
	225	0.62393	0.61301	0.59918	0.610	0.590
	180	0.60871	0.60298	0.59206	0.600	0.590
	135	0.59310	0.59056	0.58424	0.590	0.570
	90	0.57912	0.57062	0.56882	0.580	0.560
	45	0.55298	0.55016	0.54896	0.560	0.540
	0	0.52845	0.52845	0.52845	0.531	0.528
4	360	0.67234	0.67234	0.67234	0.675	0.665
	315	0.62659	0.62062	0.60105	0.570	0.560
	270	0.58411	0.57361	0.55641	0.520	0.510
	225	0.55939	0.54759	0.53134	0.500	0.490
	180	0.54152	0.53570	0.52306	0.480	0.470
	135	0.52323	0.52126	0.51386	0.480	0.470
	90	0.50680	0.49782	0.49569	0.480	0.470
	45	0.47611	0.47373	0.47233	0.470	0.460
	0	0.44840	0.44840	0.44840	0.450	0.435

It is to be noted that in Figs. 6–14 - 6–17, only the starting outcomes for the lowest started area ratio and the highest unstarted area ratio are presented. Many more experiments were conducted for each given M_∞ and ϕ (similar to what is shown in Fig. 6–13), however for clarity, these results are not included in Figs. 6–14 - 6–17.

The following observations and conclusions can be made on the bases of these results,

Table 6–2: Capture angle effect on startability of Busemann intakes designed with strong conical shock.

M_∞	ϕ°	$\frac{A_e}{A_i}_{Started-Theory}$			$\frac{A_e}{A_i}_{Started}$	$\frac{A_e}{A_i}_{Unstarted}$
		Theory(I)	Theory(II)	Theory(III)	CFD	CFD
3	360	0.71922	0.71922	0.71922	0.721	0.705
	315	0.63714	0.62434	0.58837	0.580	0.560
	270	0.55901	0.53804	0.50636	0.490	0.470
	225	0.51375	0.49534	0.46028	0.450	0.430
	180	0.48085	0.46852	0.44510	0.440	0.420
	135	0.44714	0.44176	0.42828	0.420	0.400
	90	0.41153	0.39882	0.39496	0.380	0.360
	45	0.36082	0.35470	0.35212	0.340	0.320
	0	0.30818	0.30818	0.30818	0.311	0.290
4	360	0.67234	0.67234	0.67234	0.675	0.665
	315	0.56742	0.55224	0.50670	0.540	0.530
	270	0.46851	0.443	0.40301	0.420	0.400
	225	0.41133	0.3866	0.34464	0.340	0.330
	180	0.37008	0.3551	0.32543	0.300	0.290
	135	0.327	0.32127	0.30401	0.260	0.250
	90	0.28102	0.26685	0.26188	0.220	0.210
	45	0.21772	0.2109	0.20769	0.200	0.180
	0	0.15211	0.15211	0.15211	0.156	0.135

1) The numerical results show that the minimum self-starting area ratio decreases with the decrease of capture angle (and, hence, increase of spillage) monotonically. However, the rate of change of the area ratio varies with capture angle. It is clear that in a range of capture angles centered at $\phi = 180^\circ$, the minimum self-starting area ratio is much less sensitive to the variations of capture angle and stays nearly constant. To the contrary, the area ratio changes most quickly as capture

angle approaches its limiting values of 0° and 360°. This finding may be of practical importance for choosing an appropriate capture angle from the point of view of startability and integration of the intake into airframe.

2) As was observed before, it is clear from Figs. 6–14 - 6–17 that the gain in startability (decrease in the area ratio) is more significant when capture angle decreases from 360° (fully enclosed intake) to 180° (half-Busemann intake) as compared to the gain which could be achieved by further decrease of capture angle towards zero.

3) All three theories qualitatively agree with the numerical results. They predict the decrease in area ratio with decreasing capture angle as well as the above-mentioned low sensitivity of area ratio to capture angle variation in the range of $\phi = 180° \pm 60°$.

4) As far as quantitative agreement is concerned, Theory III gives the best agreement with numerical data. At $M_\infty = 3$, the results of Theory III and numerical trials coincide both for weak and strong shock designs, while for $M_\infty = 4$, the maximum difference is of the order of 10%. It may be concluded that the influence of Mach number is not well predicted by the theories. It is not very surprising because the overboard spillage is modeled in all theories from purely geometrical considerations.

5) The predictions of Theory I and II are close to each other and markedly apart from the values provided by Theory III. Theory II, in which only spillage in upward (vertical) direction is taken into account, gives results closer to the numerical experimental data than Theory I.

6.4 Conclusion

In this chapter, the minimum self-starting area ratios for Busemann intakes with overboard spillage are obtained via numerical starting experiments. Weak and strong designs with various capture angles are considered.

Generally, the outcomes of the numerical experiments on self-starting of Busemann intakes with overboard spillage confirm the theoretical predictions from Chapter 5. It is clearly demonstrated that the startability of Busemann intakes is improved by overboard spillage. It is shown that decreasing the capture angle of Busemann intakes decreases the self-starting limiting area ratio. Two-dimensional analysis confirms the theoretical results related to the minimum self-starting area ratio values for the normal cut design thin Busemann intakes. Also, it is confirmed that compared with the Busemann intakes designed with weak conical shock, the Busemann intakes designed with strong conical shock have a lower Kantrowitz limit.

One of the theories (Theory III) predicting the magnitude of overboard spillage and its influence on intake starting demonstrates particularly good agreement with the data from numerical experiments in spite of its simplicity.

Mach 3 and 4 are chosen for this study since a wind tunnel which produces these Mach numbers may be available for future experimental studies.

CHAPTER 7
Conclusions

Detailed conclusions are presented at the end of each of the previous chapters. This chapter focuses on the significant aspects of this thesis. A detailed theoretical study on starting of Prandtl-Meyer intakes with the assistance of overboard spillage is done. The application of overboard spillage to starting of Busemann intakes is investigated. New designs of Busemann intakes are introduced and their startabilities via overboard spillage are studied. All suggested theories are verified by simulations using newly developed methodologies. Finally, appropriate further developments are suggested.

7.1 Summary

The air intake as a crucial component of supersonic air-breathing engines, scramjets, should decelerate and compress airflow with the least possible loss of total pressure to supply it to the engine combustor. The development of more efficient engines implies improving the startability of their intakes, as unstarted intakes capture less mass flow at subsonic speed and have lower efficiency and higher aerodynamic and thermal loads. Over decades, different techniques for intake starting were developed. Mostly, their performances are limited to specific flow speeds and/or they result in having heavy engines due to the extra mechanisms used to change the intake area ratio. The overboard spillage technique is the one which does not need additional mechanisms in the starting process of an intake and its usage is not limited to any

specific range of flow Mach numbers. In recent study, the overboard spillage technique's application to the one of the simplest types of planar intakes, two-shock ramp intake, was considered in detail with the goal to find ways to maximize the overboard spillage effect. In this thesis, to extend the application of overboard spillage to starting of more practical intakes, the self-starting boundaries for Prandtl-Meyer and Busemann intake families via overboard spillage are determined. The details about these intakes, different techniques used to start intakes and the Kantrowitz theory used to determine the self-starting limit of an intake are explained in Chapter 1. Previous studies on all these subjects are also reviewed.

In Chapter 2, the theoretical startability analysis of Prandtl-Meyer intake family via overboard spillage is done based on the application of the classical quasi-steady Kantrowitz theory to the internal compression section of the on-design intakes. It is concluded that using overboard spillage lowers the self-starting Kantrowitz boundaries for Prandtl-Meyer intakes. The startability of different specific designs of Prandtl-Meyer intakes (weak and strong shock designs and normal-line design) are also studied. The minimum self-starting on-design intakes' area ratio boundary is found to be very close to the one for the strong-reflected shock design, or "strong shock" design with the strong shock terminating at the ramp trailing edge.

The theoretical analysis is continued in Chapter 5 for Busemann intakes. The Busemann flow characteristics (i.e., a conically symmetric flow that compresses and contracts isentropically, with only a small final portion of compression resulting from the downstream conical shock) are specified to let us produce the Busemann intake shape for any chosen aerodynamic shock angle and the flow speed upstream of the

conical shock by integrating the Taylor-Maccoll equations and the streamline equation. The overboard spillage is achieved by cutting out an angular section of the full Busemann intake. Then, the cutting planes are covered by two flat plates allowing for overboard spillage and maintaining the Busemann flow in the started mode by the V-cut shape. Different cutting angles result in intakes with different capture angles which have different spillage amounts and, subsequently, different startabilities. Obviously, the flow spillage is increased by decreasing the intake's capture angle. As explained in Chapter 5, in this study, the flow spillage is calculated by finding the spillage area using three different theories based on purely geometrical considerations. Then, by applying the Kantrowitz theory to the internal compression section of the on-design Busemann intakes, at any free-stream flow speed, the intake highest contraction ratio which satisfies the Kantrowitz condition is determined for Busemann intake designs with terminal weak or strong conical shock and also for the normal-cut-design thin Busemann intake. The thin normal-cut-design Busemann intakes with weak conical shock have the maximum contraction limit for self-starting while the exit flowfield is non-uniform. For any chosen design, varying the flow spillage amount by adjusting the capture angle of the intake influences the startability of the intake. Therefore, by defining a function in terms of capture angle, the inlet area of the intake's internal compression section is modified based on the intake's spillage area for different capture angles. Then, the Kantrowitz limits for Busemann intakes with weak shock and strong shock designs with different capture angles are found. It is shown that smaller capture angle results in better startability.

Busemann intakes with terminal strong conical shock have low minimum self-starting area ratios while it can produce uniform exit flow when the strong shock is maintained by the application of an appropriate back pressure (although this flow is subsonic and with elevated total pressure losses due to strong shock). However, if an appropriate back pressure is not maintained and/or supersonic exit flow is required, the strong-shock-based intake can be operate with a weak conical shock and a non-uniform exit flow.

In order to validate the theoretical results, numerical investigation is undertaken. As explained in Chapter 3, at first, the methodology of numerical experiments to find the self-starting area ratios of intakes at a given free-stream Mach number is considered. In particular, the methodology to satisfy quasi-steady flow assumption of the Kantrowitz theory in a computationally efficiency is suggested. Masterix (2D) and Candifix (3D) codes are used to confirm the intake's self-starting boundaries. As the Masterix and Candifix codes do not have the capability to modify the geometry in a computational run in order to reach the on-design started intake, the modified intake's geometry needs to be produced several times and the computational run needs to be repeated. In 2D analysis, accelerating the flow with $1{,}000g$ acceleration satisfies the quasi-steady flow characteristics while in 3D analysis to reduce the computational time to about (1/10) of the original one (when flow acceleration of $1{,}000g$ is used), the initial condition of the sudden insertion of intake into $M_\infty < M_{design}$ is used. In this process after having an unstarted steady-state condition at $M_\infty < M_{design}$, the flow is accelerated to $M_\infty = M_{design}$ with $1{,}000g$ acceleration. The three levels of refinement result in accuracy of 0.1% in terms of area ratio in using 2D numerical code

although no refinement is needed to get the result with 1% accuracy from 3D numerical analysis using Candifix code. These accuracies represent the difference between the numerical results for the lowest area ratio of the started intake and the highest area ratio of the unstarted intake at each considered case in 2D and 3D numerical analysis, respectively. In 2D analysis, the background mesh includes around ~ 5000 to ~ 10000 nodes while in 3D analysis, after mesh generation, the computational domain approximately includes 0.5M tetrahedral cells, around $100{,}000$ grid nodes.

The numerical findings in Chapters 4 and 6 confirm the theoretical predictions of self-starting boundaries and demonstrate that overboard spillage significantly improves the starting characteristics. There is an excellent agreement between the numerical and theoretical results related to the self-starting boundaries of Prandtl-Meyer intakes. For Busemann intake, this agreement is less accurate due to the fact that the theories are based on geometrical considerations only and no effects of gas-dynamic spillage parameters are considered. It is shown that Busemann intakes with smaller capture angles result in lower self-starting limits. Also, it is confirmed that among all possible on-design Prandtl-Meyer intakes, the strong-shock design leads to markedly better starting characteristics. Also, compared with the Busemann intakes designed with weak conical shock, the Busemann intakes designed with strong conical shock have a lower Kantrowitz limit.

7.2 Original contribution

The following list summarizes the original contributions of this thesis:

1) Startability study for the Prandtl-Meyer intake family. The determination of the Kantrowitz (self-starting) surface for the entire family and Kantrowitz lines for particular designs.

2) The methodology of numerical intake starting experiments allowing to satisfy the main assumptions of the Kantrowitz theory in numerical starting trials.

3) New way to incorporate overboard spillage into Busemann intakes designs.

4) New Busemann intake designs are suggested: strong-shock-based designs and normal-cut designs based on Busemann flows with weak and strong shocks.

5) The first analytical treatment allowing to predict the starting characteristics (minimum self-starting area ratios) for 3D intakes with overboard spillage.

6) Demonstration of the applicability of the strong shock design principle to Prandtl-Meyer and Busemann intakes.

7) Numerical starting experiments for Prandtl-Meyer and Busemann intakes and their results.

8) Original way to simulate starting of thin Busemann intakes with overboard spillage.

7.3 Problem Statement-Need for Further Analysis

Following studies are suggested as future work:

1) Numerically analyzing the startability of normal-cut designs of Busemann intakes with different capture angles;

2) Doing the experimental study based on the suggested theories in the DRDC supersonic wind tunnel, which appears to be suitable for these experiments as the Mach number can be varied from 0.2 to 4 [147, 153];

3) Revealing the influence of viscous effects (e.g. boundary layers on inlet walls, shock/shock and shock/boundary layer interactions) on the intake starting characteristics via overboard spillage;

4) Investigating the different flow attack angles effects on starting intakes via overboard spillage.

APPENDIX A
Runge-Kutta Method

The Taylor-Maccoll and streamline equations (see Chapter 5) are solved using the following Runge-Kutta method:

$$u_{n+1} = u_n + \frac{1}{6}(k_{u1} + 2k_{u2} + 2k_{u3} + k_{u4})\Delta\theta. \tag{A.1}$$

$$v_{n+1} = v_n + \frac{1}{6}(k_{v1} + 2k_{v2} + 2k_{v3} + k_{v4})\Delta\theta. \tag{A.2}$$

$$r_{n+1} = r_n + \frac{1}{6}(k_{r1} + 2k_{r2} + 2k_{r3} + k_{r4})\Delta\theta. \tag{A.3}$$

where

$$\begin{aligned} k_{u1} &= f(u_n, v_n, \theta_n). \\ k_{v1} &= g(u_n, v_n, \theta_n). \\ k_{r1} &= h(u_n, v_n, \theta_n). \end{aligned} \tag{A.4}$$

$$\begin{aligned} k_{u2} &= f(u_n + \tfrac{1}{2}k_{u1}\Delta\theta, v_n + \tfrac{1}{2}k_{v1}\Delta\theta, \theta_n + \tfrac{1}{2}\Delta\theta) \\ k_{v2} &= g(u_n + \tfrac{1}{2}k_{u1}\Delta\theta, v_n + \tfrac{1}{2}k_{v1}\Delta\theta, \theta_n + \tfrac{1}{2}\Delta\theta) \\ k_{r2} &= h(u_n + \tfrac{1}{2}k_{u1}\Delta\theta, v_n + \tfrac{1}{2}k_{v1}\Delta\theta, \theta_n + \tfrac{1}{2}\Delta\theta) \end{aligned} \tag{A.5}$$

$$
\begin{aligned}
k_{u3} &= f(u_n + \tfrac{1}{2}k_{u2}\Delta\theta, v_n + \tfrac{1}{2}k_{v2}\Delta\theta, \theta_n + \tfrac{1}{2}\Delta\theta) \\
k_{v3} &= g(u_n + \tfrac{1}{2}k_{u2}\Delta\theta, v_n + \tfrac{1}{2}k_{v2}\Delta\theta, \theta_n + \tfrac{1}{2}\Delta\theta) \\
k_{r3} &= h(u_n + \tfrac{1}{2}k_{u2}\Delta\theta, v_n + \tfrac{1}{2}k_{v2}\Delta\theta, \theta_n + \tfrac{1}{2}\Delta\theta)
\end{aligned} \tag{A.6}
$$

$$
\begin{aligned}
k_{u4} &= f(u_n + k_{u3}\Delta\theta, v_n + k_{v3}\Delta\theta, \theta_n + \Delta\theta) \\
k_{v4} &= g(u_n + k_{u3}\Delta\theta, v_n + k_{v3}\Delta\theta, \theta_n + \Delta\theta) \\
k_{r4} &= h(u_n + k_{u3}\Delta\theta, v_n + k_{v3}\Delta\theta, \theta_n + \Delta\theta)
\end{aligned} \tag{A.7}
$$

In order to start solving the above equations, the initial values should be assumed, as explained in Chapter 5 (u_2, v_2, θ_2 and r_2).

REFERENCES

[1] Edwin H., *Constructing a turbocharger turbojet engine.*, Turbojet Technologies, 2001.

[2] NASA. (2014). Turbojet engine. Available: $http://www.grc.nasa.gov/WWW/K-12/airplane/aturbj.html$

[3] Aviadvigatel. (2014). Turbofan engine family for regional jet. Available: $http://www.avid.ru/eng/advanced-developments/Regional_Jet/$

[4] Encyclopedia of science. (2014). Turbojet and turbofan engines. Available: $http://www.daviddarling.info/encyclopedia/alphindext.html$

[5] Billig F.S., "Supersonic combustion ramjet missile," *Journal of Propulsion and Power*, Vol. 11, No. 6, 1995, pp. 1139-1146.

[6] Tahir R.B., *Starting and unstarting of hypersonic air intakes*, M.A.Sc. Thesis, Ryerson University, 2003.

[7] Van Wie D.M., D'Alessio S.M., and White M.E. "Hypersonic air-breathing propulsion," *Johns Hopkins APL Technical Digest*, Vol. 26, No. 4, 2005, pp. 430-437.

[8] Waltrup P.J., White M.E., Zarlingo F., and Gravlin E.S., "History of ramjet and scramjet propulsion development for U.S. navy missiles," *Johns Hopkins Apl. Technical Digest*, Vol. 18, No. 2, 1997, pp. 234-243.

[9] Wikipedia. (2014). Ramjet. Available: $http://en.wikipedia.org/wiki/Ramjet$

[10] Brighthub. (2014). U.S. hypersonic aircraft. Available: $http://www.brighthub.com/science/aviation/articles/65787.aspx$

[11] Billig F.S., "Propulsion systems from takeoff to high-speed flight. In: High speed flight propulsion systems," Ed. By S.N.B. Murthy and E.T. Curran, *Progress in Astronautics and Aeronautics*, Vol. 137, 1991, pp. 21-100.

[12] VanWie D.M., *Scramjet intakes*, In scramjet propulsion. Progress in astronautics and aeronautics (Eds E.T.Curran and S. N. B. Murthy), (AIAA, Reston, VA), Vol. 189, Ch. 7, 2000, pp. 447-511.

[13] ALVRJ. (2014). LTV ALVRJ. Available: $http://www.designation-systems.net/dusrm/app4/alvrj.html$

[14] Kazmar R.R., "Airbreathing hypersonic propulsionat Pratt & Whitney OverviewPratt," *AIAA, Pratt & Whitney*, AIAA 2005-3256, AIAA, 2005.

[15] NASA. (2014). NASA dryden past projects. Available: $http://www.nasa.gov/centers/dryden/history/pastprojects/HyperX/$

[16] NASA. (2014). X-43A scramjet. Available: $http://www.nasa.gov/missions/research/x43A_captive-carry.html$

[17] McClinton C.R., "X-43Scramjet power breaks the hypersonic barrier. Dryden lectureship in research for 2006," AIAA 2006-0001, AIAA, Jan. 2006.

[18] Boeing. (2014). X-51A waverider. Available: $http://www.boeing.com/boeing/Features/2014/05/bds_aiaa_x51_05_02_14.page$

[19] Heiser W.H., and Pratt D.T., *Hypersonic airbreathing propulsion*, 1st ed. Washington, D.C.:AIAA Education Series, 1994.

[20] Boyce R.R., Gerard S., and Paull A., "The HyShot scramjet flight experiment - flight data and CFD calculations compared," AIAA 2003-7029, AIAA, 2003.

[21] Paull A., Alesi H., and Anderson S., "The HyShot flight program and how it was developed," AIAA/AAAF 11th International Space Planes and Hypersonic Systems and Technologies Conference, Sep 2002, AIAA 2002-4939.

[22] Smart M.K., Hass N.E., and Paull A., "Flight data analysis of the HyShot 2 scramjet flight experiment," *AIAA Journal*, Vol. 44, No. 10, 2006, pp. 2366-2375

[23] Boyce R.R., Tirtey S.C., Brown M., Creagh M., and Ogawa H., "Scramspace: Scramjet-based access-to-space systems," AIAA 2011-2297, AIAA, 11 April 2011.

[24] Tirtey S.C., Boyce R.R., Brown L.M., and Creagh M.A., "The SCRAMSPACE I hypersonic flight experiment feasibility study," AIAA Paper 2011-2277, AIAA, 11 April 2011.

[25] Dolvin D., "Hypersonic knternational flight research and experimentation (HIFiRE)-fundamental science and technology development strategy," AIAA Paper 2008-2581, AIAA, April 2008.

[26] Kimmel R. L., Adamczak D., Dolvin D., Borg M., and Stanfield S., "Aerothermodynamic insight from the HIFiRE program," *Proceedings of the 7th European Symposium on Aerothermodynamics for space vehicle*, Brugge, Belgium, May 2011, ESA SP-692.

[27] Steelant J., "LAPCAT: High-speed propulsion technology," *Advances on Propulsion Technology for High-Speed Aircraft*, NATO Research and Technology Organisation, Neuilly-sur-Seine, France, 2008, RTO-EN-AVT-150, Paper 12, pp. 12.1 - 12.38.

[28] Steelant J., "Sustained hypersonic flight in Europe: First technology achievements within LAPCAT II," AIAA Paper 2009-7240, AIAA, Nov. 2009.

[29] Falempin F., and Serre L., "LEA flight test program - A first step towards an operational application of high-speed air breathing propulsion," AIAA-2002-5249, AIAA, 2002.

[30] Falempin F., and Serre L., "LEA flight test program - A first step to an operational application of high-speed air breathing propulsion," AIAA-2003-7031, AIAA, 15-19 December 2003.

[31] Gaisbauer U., Weigand B., and Reinartz B., "Research training group GRK 1095/1: Aerothermodynamic design of a scramjet propulsion system," *18th International Symposium on Airbreathing Engines (ISABE)*, Beijing, China, Paper 2007-1131, 2-7 Sept. 2007

[32] Weigand B., and Gaisbauer U., "An overview on the structure and work of the DFG research training group GRK 1095: Aero-thermodynamic design of a scramjet propulsion system," AIAA Paper 2009-7276, AIAA, Nov. 2009.

[33] McClinton C.R., Rausch V.L., Shaw R.J., Metha U., and Naftel C., "Hyper-X: Foundation for future hypersonic launch vehicles," *Acta Astronautica*, Vol. 57, July 2005, pp. 614-622.

[34] McClinton C.R., Rausch V.L., Nguyen L.T., and Sitz J.R., "Preliminary X-43 flight test results," *Acta Astronautica*, Vol. 57, July 2005, pp. 266-276.

[35] Boeing "X-51A waveRider breaks record in 1st flight," News Realeases/Statements [online database], http://boeing.mediaroom.com [retrieved 26 May 2010].

[36] Hank J.M., Jammes S.M., and Mutzman R.C., "The X-51A scramjet engine flight demonstration program," AIAA 2008-2540, AIAA, 28 April - 1 May 2008.

[37] Manned mission to mars. (2014). Earth based facilities. Available: *http* : *//www.androidpubs.com/Chap*04.*htm*

[38] Connors J.F., and Woollett R.R., "Performance characteristics of several types of axially symmetric nose inlets at Mach number 3.85," *National Advisory Committee for Aeronautics*, NACA research memorandum, 1952.

[39] Gruhn P., "Inviscid design of the inlet for the LAPCAT Mach 8 configuration," DLR-Interner Bericht, DLR-IB 32418-2006, 2006.

[40] Haberle J., and Gulhan A., "Investigation of two-dimensional scramjet inlet flowfield at Mach 7", *Journal of Propulsion and Power*, Vol. 24, No. 3, 2008, pp. 446-459.

[41] Sorensen N.E., and Smeltzer D.B., "Study of two axisymmetric inlets designed for Mach 3.5," *Journal of Aircraft*, Vol. 13, No. 11, 1976, pp. 845-849.

[42] Van Wie D.M., and Ault D.A., "Internal flowfield characteristics of a scramjet inlet at Mach 10," *Journal of Propulsion and Power*, Vol. 12, No. 1, 1996, pp. 158-164.

[43] Goonko Y.P., Latypov A.F., Mazhul I.I., Kharitonov A.M., Yaroslavtsev M.I., and Rostand P., "Structure of flow over a hypersonic inlet with side compression wedges," *AIAA Journal*, Vol. 41, No. 3, 2003, pp. 436-447.

[44] Holland S.D., "Reynolds number and cowl position effects for a generic sidewall compression scramjet inlet at Mach 10: A computation and experimental investigation," AIAA 1992-4026, AIAA, 1992.

[45] Holland S.D., and Murphy K.J., "An experimental parametric study of geometric, Reynolds number, and ratio of specific heats effects in three-dimensional sidewall compression scramjet inlets at Mach 6," AIAA 1993-740, AIAA, Jan. 11-14, 1993.

[46] Holland S.D., "Mach 10 experimental database of a three-dimensional scramjet inlet flow field," *NASA Technical Memorandum*, NASA TM-4648, 1995.

[47] Trexler C.A., "Performance of an inlet for an integrated scramjet concept," *Journal of Aircraft*, Vol. 11, No. 9, 1974, pp. 589-591.

[48] Nguyen T., Behr M., Reinartz B., Hohn O., and Gulhan A., "Numerical investigations of the effects of sidewall compression and relaminarization in 3D scramjet inlet," AIAA Paper 2011-2256, AIAA, 11-14 April 2011.

[49] Hohn O., and Gulhan A., "Experimental investigation on the influence of sidewall compression on the flowfield of a scramjet inlet at Mach 7," AIAA 2011-2350, AIAA, April 2011.

[50] Huang G., Zhou M., Chen J., and You Y., "A new combined design of inlet and forebody for high-speed vehicle," AIAA 2011-5828, AIAA, 31 July - 03 August 2011.

[51] You Y., "An overview of the advantages and concerns of hypersonic inward turning inlets," AIAA Paper 2011-2269, AIAA, 11 - 14 April 2011.

[52] Goldman A.L., and Willis B.P., "Test results of a fixed geometry RBCC inlet," AIAA Paper 1999-2589, AIAA, 20-24 June, 1999.

[53] Smart M.K., Trexler C.A., and Goldman A.L., "A combined experimental/computational investigation of a rocket based combined cycle inlet," AIAA Paper 2001-671, AIAA, Jan 2001.

[54] Liang J-H, Fan X-Q, Wang Y., and Liu W-D, "Performance enhancement of three-dimensional hypersonic inlet with sidewall compression," *Proceedings of The Institution of Mechanical Engineers Part G-Journal of Aerospace Engineering - PROC INST MECH ENG G-J A E 01/2008*, Vol. 222, No. 8, 2008, pp. 1211-1219.

[55] Molder S., and Szpiro E.J., "Busemann inlet for hypersonic speeds," *AIAA Journal of Spacecraft and Rockets*, Vol. 3, No. 8, pp. 1303-1304, August 1966.

[56] Smart M.K., "Design of three-dimensional hypersonic inlets with rectangular-to-elliptical shape transition," *Journal of Propulsion and Power*, Vol. 15, No. 3, pp. 408-416, May 1999.

[57] Hong W., and Kim C., "Numerical study on supersonic inlet buzz under various throttling conditions and fluid-structure interaction," AIAA 2011-3967, AIAA, 2011.

[58] Trexler C.A., "Intake starting predictions for sidewall-compression scramjet intakes," AIAA Paper 1988-3257, AIAA, July 1988.

[59] Holland S.D., "Mach 10 computational study of a three-dimensional scramjet inlet flow field," *NASA Technical Memorandum*, Vol TMON 4602, March 1995.

[60] Yuan Z.K., Dong X.X., and Hui X., "The parametric analysis and experimental investigation of sidewall compression intake at Mach 5.3 in non-uniform incoming flow condition," AIAA Paper 95-2889, AIAA, 1995.

[61] Goonko Y.P., Kharitonov A.M., Mazhul I.O., Zvegintsev V.I., Nalivaichenko D.G., and Chirkadhenko V.F., "Investigation of a scramjet model at hypersonic velocities and high Reynolds numbers," AIAA 2002-5273, AIAA, 2002.

[62] Smart M.K., "Experimental testing of a hypersonic intake with rectangular-to-elliptic shape transition," *AIAA Journal of Propulsion and Power*, Vol. 17, pp.276-283, 2001.

[63] Smart M.K., and Trexler C.A., "Mach 4 performance of a fixed-geometry hypersonic inlet with rectangular-to-elliptical shape transition," *Journal of Propulsion and Power*, Vol. 20, No. 2, 2004, pp. 288293.

[64] Billig F.S., and Kothari A.P., "Streamline tracing: Technique for designing hypersonic vehicles," *Journal of Propulsion and Power*, Vol. 16, No. 3, 2000, pp. 465-471.

[65] Tam C-J, Baurle R.A., and Streby G.D., "Numerical analysis of steamline-traced hypersonic intakes," AIAA Paper 2003-13, AIAA, 2003.

[66] Haddad A., and Moss J.B., "Aerodynamic design for supersonic nozzles of arbitrary cross section," *Journal of Propulsion and Power*, Vol. 6, No. 6, 2000, pp. 740-746.

[67] Lu X., Yue L., Xiao Y., Chen L., and Chang X., "Design of scramjet nozzle employing streamline tracing technique," AIAA 2009-7248, AIAA, 2009.

[68] Bussey G.H., and Lewis M.J., "Application of compound compressible flow to hypersonic three-dimensional inlets," AIAA-2009-7403, AIAA, 2009.

[69] Gollan R.J., and Ferlemann P.G., "Investigation of REST-class hypersonic inlet designs," AIAA Paper 2011-2254, AIAA, April 11-14, 2011.

[70] Hermann R., *Supersonic intake diffusers and introduction to internal aerodynamics*, Minneapolis-Honeywell Regulator Company, 1st ed. 1956.

[71] Clark J., "An experimental investigation of a supersonic two-dimensional perforated inlet at a nominal free-stream Mach number of 2.50," *Univ. of Toronto Inst. for Aerospace Studies*, TN 24, Toronto, Ontario, Canada, 1958.

[72] Seddon J., and Goldsmith E.L., *Intake aerodynamics*, AIAA Education Series, New York, 2nd Edition, 402 pages, 1999.

[73] Ives D. C., "Supercritical inlet design" AIAA Applied Aerodynamics Conference, Pratt and Whitney Group, AIAA-83-1866, AIAA, 1983.

[74] Hawken D.F., and Gottlieb J.J., *Prediction of two-dimensional time-dependent gasdynamic flow for hypersonic studies*, Viatec Resource Systems Inc, Toronto, Ontario, March 1990, UTIAS Report No. 335.

[75] Molder S., McGregor R.J., and Paisley T.W., *A Comparison of three hypersonic air inlets*. Ryerson Poly technical Institute, Toronto, 1991.

[76] Curran E.T., and Murthy S.N.B., "Scramjet propulsion," *Progress in Astronautics and Aeronautics*, Vol. 189, 2000.

[77] Parent B., and Sislian J.P., "Hypersonic mixing enhancement by compression at a high convective Mach number," *AIAA Journal*, Vol. 42, No. 4, 2004, pp. 787-795.

[78] Zhang L., Zhang K., Wang L., and Liu Y., "Numerical investigation of hypersonic curved shock two-dimensional inlet designed on the wall constant Mach number gradient," AIAA Paper 2012-4065, AIAA, 2012.

[79] Busemann A., "Drucke auf kegelformige spitzen bei bewegung mit uberschallgeschwindigkeit," *Ztscr.f. angew. Math. und Mech.*, Vol. 9, No. 6, Dec. 1929, pp. 496-498.

[80] Taylor I., and Maccoll J.W., "The air pressure on a cone moving at high speeds," *Proceedings of the Royal Society of London*, Vol. 139, 1933, pp. 278-311.

[81] Molder S., and Romeskie J.M., "Modular hypersonic intakes with conical flow," *AGARD Conference Proceedings*, No. 30, 1968.

[82] Busemann A., "Die achsensymmetrische kegelige uberschallstromung," *Luftfahrtforschung*, Vol. 19, No. 4, 1944, pp. 137-144.

[83] Van Wie D.M., and Molder S., "Application of Busemann intake designs for flight at hypersonic speeds," AIAA Paper 92-1210, AIAA, 1992.

[84] Billig F.S., Baurle R.A., Tam C-J, and Wornom S.F., "Design and analysis of streamline traced hypersonic inlets," AIAA Paper 99-4974, AIAA, Nov. 1999.

[85] Ramasubramanian V., Sarkey R., and Lewis M., "An euler numerical study of Busemann and quasi-Busemann hypersonic inlets," AIAA-2008-66, AIAA, Jan 2008.

[86] Molder S., "A benchmark for internal flow CFD codes," *Computational fluid dynamics Journal*, Vol. 12, No. 2, p. 47, 2003.

[87] Ogawa H., and Boyce R.R., "Physical insight into scramjet inlet behavior via multi-objective design optimisation," *AIAA Journal*, Vol. 50, No. 8, August 2012.

[88] Molder S., *Curved aerodynamic shock waves*, PhD thesis, Jan. 2012.

[89] Ramasubramanian V., Lewis M., and Starkey R., "Performance of various truncation strategies employed on hypersonic Busemann inlets," AIAA 2009-7249, AIAA, 2009.

[90] Van Wie D.M., Kwok F.T., and Walsh R.F., "Starting characteristics of supersonic inlets," AIAA Paper 96-2914, AIAA, 1996.

[91] Rodriguez C.G., "CFD analysis of the CIAM/NASA scramjet," AIAA 2002-4128, AIAA, 2002.

[92] Yue L., Chen L., Xiao Y., Gong P., and Chang X., "Research on threedimensional scramjet inlet," AIAA Paper 2006-9141, AIAA, 2006.

[93] Wang Y., Liang J., Fan X., Liu W., and Wang Z. "Investigation on the unstarted flowfield of a threedimensional sidewall compression hypersonic inlet," AIAA Paper 2009-7404, AIAA, 2009.

[94] Hutchins K.E., Akella M.R., Clemens N.T., and Donbar J.M., "Detection and transient dynamics modeling of experimental hypersonic inlet unstart," AIAA 2012-2808, AIAA, 25-28 June 2012.

[95] Saunders J.D., Slater J.W., Dippold V., Lee J., Sanders B.W., and Weir L.J., "Intake mode transition screening test for a turbine-based combined-cycle propulsion system," As part of the NASA fundamental aeronautics program / hypersonics project, James L. Pittman, Principle Investigator, Supported through Contract no. NAS3-03110 and NNC08CA60C, 2008.

[96] Barber T.J., Hiett D., and Fastenberg S., "CFD modeling of the hypersonic intake starting problem," AIAA Paper 2006-123, AIAA, 2006.

[97] Bolender M.A., Wilkin H., Jacobsen L., Drayna T., and Dwenger A., "Flight dynamics of a hypersonic vehicle during inlet unstart," AIAA-2009-7292, AIAA, 2009.

[98] Molder S., Timofeev E.V., Tahir R., and Najafiyazdi A., "Analytical and numerical study of flow starting in supersonic inlets by mass spillage," AIAA Paper 2007-5072, AIAA, 2007.

[99] Kantrowitz A., and Donaldson C., "Preliminary investigation of supersonic diffusers," Advance Confidential Report L5D20, *NACA*, 1945.

[100] Kantrowitz A., "The formation and stability of normal shock waves in channel flows," Technical Note 1225, *NACA*, 1947.

[101] Evvard J.C., and Blakey J.W., "The use of perforated intakes for efficient supersonic diffusion," *NACA*, RM E7C26, 1947.

[102] Saad M.A., *Compressible fluid flow*, 2nd Edition, Prentice Hall, 1985.

[103] Park S.O., Chung Y.M., and Sung H.J., "A numerical study of unsteady supersonic compression ramp flows," *AIAA Journal*, Vol. 32, No. 1, 1994, pp.216-218.

[104] Tahir R., Molder S., and Timofeev E., "Unsteady starting of high Mach number air intakes – A CFD Study," AIAA Paper 2003-5191, AIAA, 2003.

[105] Li Z., Huang B., and Yang J., "A novel test of starting characteristics of hypersonic inlets in shock tunnel," AIAA Paper 2011-2308, AIAA, 2011.

[106] Grainger A.L., Boyce R.R., Tirtey S.C., and Ogawa H., "The unsteady flow physics of hypersonic inlet starting processes," AIAA 2012-5937, AIAA, 24-28 Sep 2012.

[107] Wikipedia. (2014). Lockheed SR-71 Blackbird. Available: $http://en.wikipedia.org/wiki/Lockheed_SR-71_Blackbird$

[108] Higgins A., *Compressible fluid notes*. Department of Mechanical Engineering, McGill University, 2005.

[109] Oates G.C., *The aerodynamics of gas turbine and rocket propulsion*, AIAA Education Series, 3rd edition, 468 pages, 1997.

[110] Prakash D.P., *Hypersonic intake studies*, Master of Technology Dissertation, Department of Aerospace Engineering Indian Institute of Technology, Bombay, 2006.

[111] Diggins J.L., and Lange A.H., *A systematic study of a variable area diffuser for supersonic wind tunnels*, NAVORD Rep. 2421, U.S. Naval Ord. Lab. (White Oak, Md.), Dec. 1952.

[112] Goldberg T.J., and Hefner J.N., "Starting phenomena for hypersonic inlets with thick turbulent boundary layer at Mach 6," Lungley Reseurch Center Humpton, Va. 23365, National Aeronautics and Space Administration Washington D.C., 1971.

[113] Ferri A., and Nucci L.M., "Theoretical and experimental analysis o low-drag supersonic intakes having a circular cross section and a central body at Mach numbers of 3.30, 2.75, and 2.45," *National Advisory Committee for Aeronautics*, Report 1189, 1948, pp. 737-773.

[114] Mossman E.A., and Pfyl F.A., "An experimental investigation at Mach numbers from 2.1 to 3.0 of circular-internal-contraction intakes with translating center bodies," *NACA RM A56G06*, 1956.

[115] Scherrer R., and Gowen F.E., "Preliminary experimental investigation of a variable-area, variable-internal-contraction air intake at Mach numbers between 1.42 and 2.44," *NACA RM A55F23*, 1955.

[116] Scherrer R., and Anderson W.E., "Investigation of the performance and internal flow of a variable-area, variable-internal-contraction air intake at Mach numbers of 2, 2.5, and 2.92," *NACA RM A58O24*, 1958.

[117] Dalle D., Torrez S., and Driscoll J., "Performance analysis of variable-geometry sramjet inlets using a low-order model," AIAA-2011-5756, AIAA, 31 July - 03 August 2011.

[118] Imfeld, W.F., "Development program for the F-15 inlet," *AIAA Journal of Aircraft*, Vol. 13, No. 4, 1976, pp. 286-291.

[119] Rettie I.H., and Lewis W.G.E., "The design and development of an air intake for a supersonic transport aircraft," AIAA-1967-0752, AIAA, October 1967.

[120] Candel S., "Concorde and the future of supersonic transport," *AIAA Journal of Propulsion and Power*, Vol. 20, No. 1, 2004, pp. 59-68.

[121] Porcher C.E. and Thebiay F.J., "Development of the variable geometry inlet for the B-58 airplane," SAE 595N, October 1962.

[122] Johnson, C.L., "Some development aspects of the YF-12A interceptor aircraft," *AIAA Journal of Aircraft*, Vol.7, No.4, 1970, pp.355-359.

[123] Law P., *SR-71 propulsion system P&W J-58 engine (JT11D-20)*, Cal-TECH course Ae107 on SR-71 development, 1991.

[124] Wasserbauer J.F., Meleason E.T., and Burstadt P.L., "Experimental investigation of the performance of a Mach 2.7 two-dimensional bifurcated inlet with 30 percent internal contraction," NASA TM-106728, May 1996.

[125] Moses P.L., "X-43C plans and status," AIAA Paper 2003-7084, AIAA, 2003.

[126] Morgenstern J.M., Norstrud N., Stelmack M., and Jha P.D., "Advanced concept studies for supersonic commercial transports entering service in 2030-2035 (N+3)," AIAA Paper 2010-5114, AIAA, June 2010.

[127] Hirt S.M., Chima R.V., Vyas M.A., Conners T.R., Wayman T.R., and Reger R.W., "Experimental investigation of a large-scale low-boom inlet concept," AIAA-2011-3796, AIAA, June 2011.

[128] Wu J., "An experimental study of perforated intake diffusers at a free-stream Mach number of 2.5," *Univ. of Toronto Inst. for Aerospace Studies*, 1960.

[129] Liou M-F, and Benson T.J., "Optimization of bleed for supersonic inlet," AIAA 2010-9172, AIAA, 2010.

[130] Molder S., Timofeev E.V., and Tahir R.B. "Flow starting in high compression hypersonic air intakes by mass spillage," AIAA Paper 2004-4130, AIAA, 2004.

[131] Najafiyazdi A., Tahir R., and Timofeev E.V., "Analytical and numerical study of flow starting in. supersonic inlets by mass spillage," AIAA Paper 2007-5072, AIAA, July 2007.

[132] Veillard X., Tahir R., Timofeev E., and Molder S. "Limiting contractions for starting simple ramp-type scramjet intakes with overboard spillage," *AIAA Journal of Propulsion and Power*, Vol. 24, No. 5, 2008, pp. 1042-1049.

[133] Sun B., and Zhang K., "Empirical equation for selfstarting limit of supersonic inlets," *Journal of Propulsion and Power Technical Notes*, Vol.26, No. 4, Mar. 2010, pp. 874 -875.

[134] Hohn O.M., and Gulhan A., "Analysis of a three-dimensional, high pressure ratio scramjet inlet with variable internal contraction," AIAA 2012-5975, AIAA, 24-28 Sep. 2012.

[135] Rosli M.R., Takahashi M., Sato T., Kojima T., Taguchi H., and Maru Y., "Streamline tracing technique based design of elliptical-to-rectangular transitioning hypersonic inlet," AIAA-2013-2665, AIAA, 2013.

[136] Degani D., and Steger J.L., "Comparison between Navier-Stokes and thin-layer computations for separated supersonic flow," *AIAA Journal*, Vol. 21, No. 11, 1983, pp. 1604-1606.

[137] Coon M.D., and Chapman G.T., "Experimental study of flow separation on an oscillating flap at Mach 2.4," *AIAA Journal*, Vol. 33, No. 2, 1995, pp. 282-288.

[138] Molder S., Sullivan P.A., Sislian J.P., Gottlieb J.J., McGregor R.J., Paisly T.W., Weston S.C., Rogers R.J., Hawboldt R.J., Deschambault R.L., Groth C.P.T., Hawken D.W., He Z D., Chen L.W., and Gordon K.A. "Investigations in the fluid dynamics of scramjet intakes," Final Contract report USAF, Contract No: F33615-87-C-2748: JHU, Contract No: APL 602235-0, *Ryerson Polytechnic Institute and University of Toronto Institute for AerospaceStudies*, 1992.

[139] Tahir R.B., *Analysis of shock dynamics in supersonic intakes*, Ph.D. Thesis, McGill University, 2008.

[140] Masterix, Two-dimensional, multi-block, multi-gas, adaptive, unstructured mesh, unsteady and steady-state, CFD software. Software Package, Ver. 3.40.0.3018, RBT Consultants, Toronto, ON, 2010-2013.

[141] Candifix, Three-dimensional, multi-gas, adaptive, unstructured mesh, time-accurate unsteady, CFD software. Software Package, Ver. 1.10.0065, RBT Consultants, Toronto, ON, 2010-2013.

[142] Toro E.F., *Riemann solvers and numerical methods for fluid dynamics A practical intoduction*, Springer, 2nd edition, 1999.

[143] Saito T., Voinovich P., Timofeev E., and Takayama K., *Development and application of high-resolution adaptive numerical techniques in shock wave research center in: Godunov methods: Theory and applications*, Edited Review, E.F. Toro (Ed.), Kluwer Academic/Plenum Publishers, New York, USA, 2001, pp. 763-784.

[144] OpenCASCADE, Getting started, http://www.opencascade.org/org/gettingstarted/.

[145] Netgen, Installation and requisite libraries, http://sourceforge.net/apps/ mediawiki/netgenmesher/index.php?title=Installwindows.

[146] Renderix, One-, two-, and three-dimensional, structured and unstructured data visualization software for Windows R. Software Package, Ver. 1.1.723, RBT Consultants, Toronto, ON, 2010-2013.

[147] DRDC, Trisonic Wind Tunnel, Defense RD Canada-Valcartier.

[148] Hynes T. P., and Greitzer E. M., "A method for assessing effects of circumferential flow distortion on compressor stability." *Journal of turbomachinery* Vol. 109, No. 3, 1987, pp. 371-379.

[149] O'Brien T. F., and Colville J. R., "Analytical computation of leading-edge truncation effects on invicid Busemann-inlet performance," *Journal of Propulsion and Power*, Vol. 24, No. 4, 2008, pp. 655-661.

[150] Anderson J.D., *Modern compressible flow with historical perspective*, McGraw-Hill, 1982.

[151] Emanuel G., *Analytical fluid dynamics, CRC Press*, 1994.

[152] Kreyszig E., *Differential geometry*, Dover Publications, 1991.

[153] Moerel J.-L., Veraar R.G., Halswijk W.H.C., Pimentel R., Corriveau D., Hamel N., Lesage F., and Vos J.B., "Internal flow characteristics of a rectangular ramjet air intake," AIAA 2009-5076, AIAA, 2-5 August 2009.